Geometric Design Methods for Conducting Solids Cooled by Conjugate Heat Transfer Including Surface Radiation

by

Chadwick D. Sevart
Department of Mechanical Engineering
University of Kansas

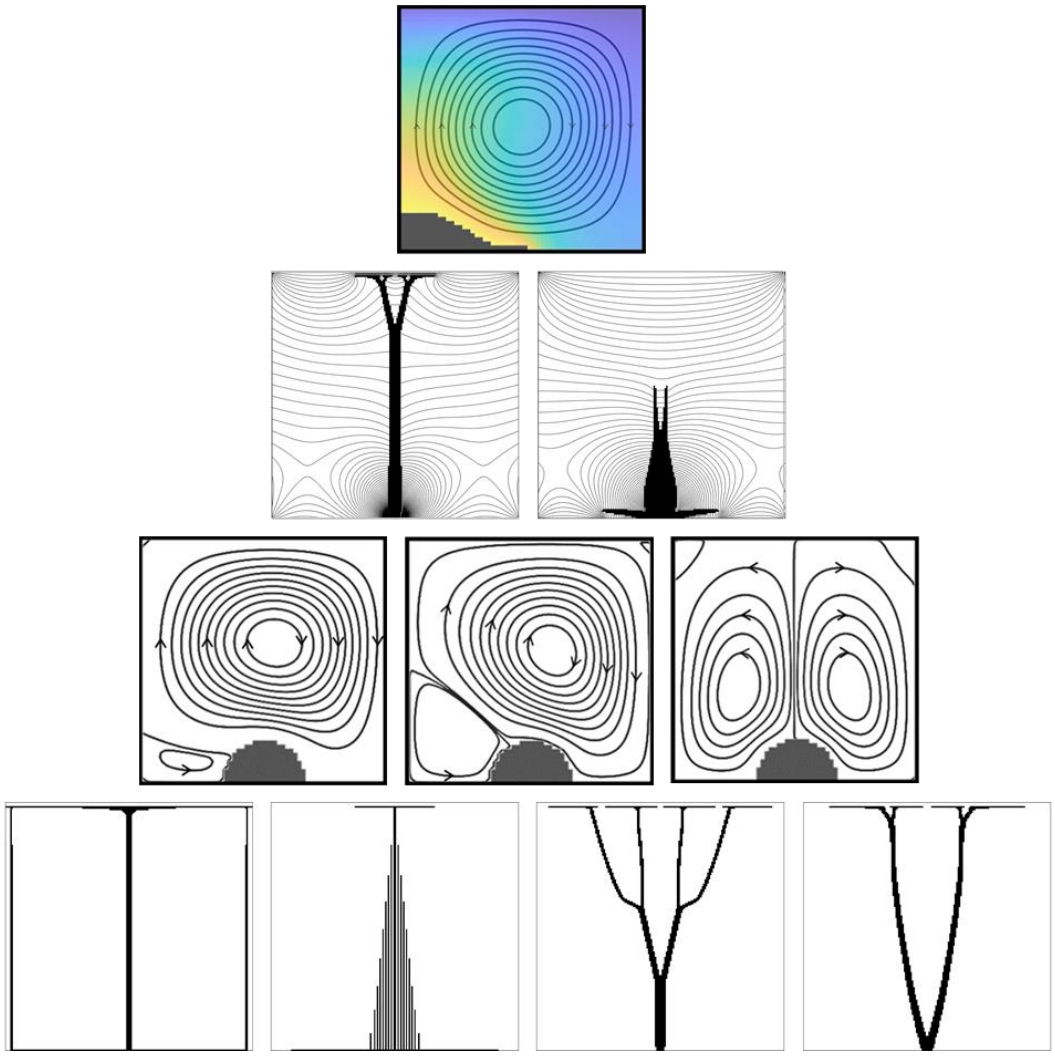

Geometric Design Methods for Conducting Solids Cooled by Conjugate Heat Transfer Including Surface Radiation

by

Chadwick D. Sevart

Submitted to the graduate degree program in Mechanical Engineering and the Graduate Faculty of the University of Kansas in partial fulfillment of the requirements for the degree of Doctor of Philosophy.

_____
Chairperson Professor **Theodore L. Bergman**
Dept. of Mechanical Engineering, University of Kansas

_____
Professor **Christopher Depcik**
Dept. of Mechanical Engineering, University of Kansas

_____
Associate Professor **Huazhen Fang**
Dept. of Mechanical Engineering, University of Kansas

_____
Associate Professor **Xianglin Li**
Dept. of Mechanical Engineering, University of Kansas

_____
Professor **Z.J. Wang**
Dept. of Aerospace Engineering, University of Kansas

Date Defended: May 20th, 2022

University of Kansas
Department of Mechanical Engineering
Learned Hall 3165a, 1530 W. 15th Street
Lawrence, Kansas 66046

The Dissertation Committee for Chadwick Sevart

certifies that this is the approved version of the following dissertation:

Geometric Design Methods for Conducting Solids Cooled by Conjugate Heat Transfer Including Surface Radiation

_____

Chairperson Professor **Theodore L. Bergman**
Dept. of Mechanical Engineering, University of Kansas

Date approved: May 20th, 2022

Preface

This dissertation is submitted to the graduate degree program in Mechanical Engineering and the Graduate Faculty of the University of Kansas in partial fulfillment of the requirements for the degree of Doctor of Philosophy. The work was performed at the Department of Mechanical Engineering, at the University of Kansas from September 2018 to April 2022 under the supervision of main supervisor Professor Theodore L. Bergman. Co-supervisors for this work are Professors Christopher Depcik, Huazhen Fang, and Xianglin Li of the Department of Mechanical Engineering and Professor Z.J. Wang of the Department of Aerospace Engineering.

I've been extremely fortunate over the course of this dissertation work and have many people for which I would like to express my gratitude. First and foremost, I would like to thank my adviser, Dr. Bergman, who has been a tremendous mentor to me ever since I started working with him as an undergraduate research assistant. Your extensive heat transfer knowledge and ability to teach complex concepts has given me a deeper understanding of the field. The experience I've gained from our many technical discussions is immeasurable and I know I am a better researcher for it. More importantly, your enthusiasm for our research was always encouraging. The work detailed in this dissertation was not always easy, but it was always enjoyable, thanks to Dr. Bergman.

To all of the professors in the ME department at KU who I have had the joy of interacting with, thank you for providing such a great research environment and always being welcoming to technical discussions. To Dr. Li, thank you for providing me with your CFD source code and for meeting with me at length to explain the concepts and implementation. The tools you gave me made all of this work possible. Thank you to the other committee members, as well, including Dr. Peter Tenpas. The insight you provided greatly improved my research. Also, thank you to the faculty who work in the ME office, whose bright personalities always made my day.

I would like to thank my amazing family for their support and encouragement over the past four years. To my dad, who is responsible for my initial interest in engineering, thank you for being such a great role model and for always expressing your pride in me. Thank you to my siblings, Hillary, Blake, Max, and Syed, for always being there for me. It's always nice to hear from you when I'm missing home, and the times that we spend together are some of my favorite moments. To my in-laws, thank you for always treating me as your own and for providing much needed advice.

Finally, and most importantly, I would like to thank my wonderful wife for her love and encouragement through the years. I truly could not have accomplished this without your support. Thank

you for your immense patience and understanding. I am so excited to continue growing this life we've made. This is just one of the many dreams we will accomplish together.

Abstract

The objective of this dissertation is to develop and investigate design methods for conducting solids cooled by multimode heat transfer, including surface radiation. The goal is to determine solid shapes with reduced or minimal overall thermal resistances. The influence of radiation on the predicted optimal shapes and thermal performance is investigated.

First, a heuristic, evolutionary design method (EDM) is developed that iteratively adjusts a discrete solid shape based on local surface heat fluxes and temperatures. The EDM is initially applied to a conjugate conduction-free convection problem and compared to a solid replicated from a benchmark topology optimization (TO) study. While the EDM does not achieve the thermal performance of the benchmark solid, it does reduce the overall thermal resistance from an initial, arbitrary geometry. The effects of radiation are then incorporated into the physical model and EDM, which is applied to a range of solid emissivities and domain sizes. It is found that radiation has a significant influence on the thermal behavior (fluid flow and temperature distribution) and therefore on the predicted optimal solid shapes. In general, increasing the strength of radiation results in increased symmetry about the vertical centerline for both the thermal behavior and predicted solid geometries.

Next, to isolate the effects of radiation, a coupled conduction-radiation problem is considered, and a heuristic solid growth method (SGM) is introduced that is similar in concept to the EDM. The SGM is distinct in that it incrementally adds solid material to the domain, so the solid mass is not constant throughout the design process. It is demonstrated that the relative strength of radiation has a significant effect on the solid growth and thermal performance. The SGM is also compared to a formal TO method that neglects the effects of radiation in obtaining optimal solid shapes. It is found that when a low amount of solid material or a relatively low solid thermal conductivity is considered, the SGM produces favorable solid configurations with lower overall thermal resistances.

The effects of radiation are then incorporated into a formal TO method, by introducing a dual solid method (DSM) that utilizes both a discrete and continuous description of the solid material distribution. The discrete description is used to model radiation heat transfer, while the continuous solid description is used in conjunction with a TO method to adjust the solid shape. It is once again shown that the effects of radiation have a strong influence on the predicted optimal solid shapes and thermal performances.

Lastly, a comparison of heuristic (SGM) and formal (DSM) design methods is made. When a high thermal conductivity solid is considered, the DSM achieves a lower overall thermal resistance. However, somewhat surprisingly, the SGM produces shapes having better thermal performance when a low solid thermal conductivity is considered.

Publications

The following publications provide the basis for this dissertation. All numerical work detailed within the articles was completed by me under the advisory of Dr. Theodore Bergman.

P1: *C.D. Sevart and T.L. Bergman, An Iterative Design Method to Reduce the Overall Thermal Resistance in a Conjugate Conduction-Free Convection Configuration, Frontiers in Heat and Mass Transfer, 13 (18) (2019) (10 pages)*

The purpose of this paper is to develop a discrete, heuristic evolutionary design method and apply it to a conjugate conduction-free convection problem.

P2: *C.D. Sevart and T.L. Bergman, Evolutionary Design Method for a Conducting Solid Cooled by Combined Free Convection and Radiation, Journal of Heat Transfer, 143 (4) (2021) p. 042103 (9 pages)*

In this work, the effects of radiation are incorporated into the design methods developed in paper **P1** and the influence of radiation on the final solid shape and thermal resistance is determined.

P3: *C.D. Sevart and T.L. Bergman, Growth Based Design of a Conducting Solid Cooled by Conjugate Gas Conduction and Surface Radiation, Proceedings of the ASME IMECE (2022) (In Review)*

A heuristic growth-based design method is developed and applied to a conjugate radiation-conduction problem. The design method is similar to that of papers **P1** and **P2** but distinct in that the solid mass is not constant throughout the design process. The growth-based design method is compared to a topology optimization method which neglects the effects of radiation.

P4: *C.D. Sevart and T.L. Bergman, A Dual Solid Method for Topological Optimization of a Conducting Solid Cooled by Gas Conduction and Surface Radiation, Journal of Heat Transfer, (In Review)*

A formal topology optimization method that incorporates the effects of radiation is developed and applied to a radiation-conduction problem.

Table of Contents

Introduction 1

1.1 Background

The geometric optimization of heat transfer devices is an important consideration for an assortment of thermal management applications. In terms of heat sink design, the goal is often to limit the amount of material or mass while minimizing the overall thermal resistance. Historically, this has been achieved by size and shape optimization (Bar-Cohen 1979, Bar-Cohen *et al*. 2003, Ahmed *et al*. 2018). For example, Bar-Cohen (1979) maximized the heat transfer rate per unit volume of a plate-fin heat sink cooled by natural convection by optimizing the fin spacing and thickness. The obvious drawback to size and shape optimization is that the basic geometric features must be specified *a priori*, while a true optimal structure might be more complex and unexpected.

A design method that allows for more geometric freedom is Constructal Theory (Bejan 1997), which involves the hierarchical optimization and construction of flow pathways. The overall geometry is obtained by assembling multiple smaller sections referred to as constructs. It has been observed that increasing the number of constructs or lowering the number of constraints results in more complex geometries with lower thermal resistances (Almogbel and Bejan 2001, Muzychka 2007). While the overall geometry can evolve into more complex and unanticipated shapes, Constructal Theory still requires that the basic geometric features of the constructs be specified *a priori*.

Topology Optimization (TO), however, is a design method that does not rely on any pre-specified geometric features and thus allows for the most geometric freedom (Bendsoe and Sigmund 2003). The solid shape is defined by a material distribution method that utilizes a discretized domain. The general TO process involves (*i*) specification of an initial material distribution and an objective function to be optimized, then (*ii*) the governing equations that describe the physics of the problem are solved (*e.g.* conservation of thermal energy, Navier-Stokes equations) and the objective function is evaluated, next (*iii*) the material distribution is adjusted according to an optimization algorithm. Steps (*ii*) and (*iii*) are repeated until the solid shape converges to an optimal solution. There are many subsets of TO that are characterized by the material distribution and optimization methods employed (Sigmund and Maute 2013). One such subset that is commonly used is density TO methods, which utilize a spatial distribution of a solid volume fraction, γ. The distribution can be discrete, in which each computational control volume or finite element is either solid or fluid (γ = 1 or 0), or continuous, meaning that some locations contain a mixture of solid and fluid ($0 \leq \gamma \leq 1$). While discrete methods have the advantage of producing

a definite solid-fluid interface, continuous methods often have better accuracy in obtaining optimal structures (Sigmund and Maute 2013).

The earliest examples of TO applied to heat transfer problems considered pure conduction (Li *et al*. 1999, Li *et al*. 2004, Gersborg-Hansen *et al*. 2006, Zhang and Liu 2008, Gao *et al*. 2008, Marck *et al*. 2012). However, for practical applications, it is often necessary to consider multiple modes of heat transfer. For example, many TO studies have considered the optimal design of conducting solids cooled by forced convection (Bruns 2007, Iga *et al*. 2009, Yoon 2010, Marck *et al*. 2013, Yan *et al*. 2019, Zhang *et al*. 2021). Iga *et al*. (2009) incorporated a design-dependent convection coefficient into a continuous density TO method and found that the strength of convection had a significant effect on the optimal solid shape and thermal performance. Another physical situation that has been considered by multiple TO studies is conjugate conduction-free convection heat transfer (Alexandersen *et al*. 2014, Alexandersen *et al*. 2016, Alexandersen *et al*. 2018, Lazarov *et al*. 2018). Similar to the findings of Iga *et al*. (2009), it has been observed that the optimal solid shape and thermal performance are highly dependent on the strength of advection when TO is applied to problems involving free convection (Alexandersen *et al*. 2014).

Studies which consider the effects of radiation heat transfer in TO are much more limited. Castro *et al.* (2015) considered a radiative enclosure and optimized the distribution of reflective material on the interior surfaces using a continuous density TO method. Multiple objective functions and boundary condition cases were considered, and each resulted in a unique optimal solution. In a similar study, Zhao *et al*. (2021) determined the optimal distribution of radiant cooling panels within an office. The objective function considered both energy consumption and occupant thermal comfort. Both Castro *et al*. (2015) and Zhao *et al*. (2021) considered the optimal distribution of material on a surface, however, a more complex problem is the determination of optimal solid shapes that are cooled by radiation heat transfer. Wang *et al*. (2022) considered a thermophotonic problem and optimized the microscale material distribution of a thin film cooled by radiation and convection heat transfer. Radiation was incorporated into the heat diffusion equation as a uniformly distributed source term, which was independent of temperature. While the conduction and radiation processes were only weakly coupled, the radiative properties were dependent on the material distribution. Therefore, the optimal solid shape was influenced by conduction, radiation, and convection.

To the author's knowledge, TO has not been applied to a conducting solid cooled by strongly coupled multimode heat transfer, including the effects of surface-to-surface radiation. The application of TO to such a situation presents multiple difficulties. For example, while continuous density TO methods have higher accuracy than discrete methods, they do not possess a clear solid-fluid interface at which to evaluate radiation heat transfer. Furthermore, formal TO methods often rely on the evaluation of the

sensitivity (partial derivative) of the objective function to the solid shape (γ). The dependence of radiation transfer on view factors, for example, makes evaluating the sensitivities difficult. Regardless of these challenges, radiation heat transfer can often have a strong influence on thermal performance (Audunson and Gebhart 1972, Carpenter *et al*. 1976, Hall *et al*. 1999, Chu *et al*. 2019), therefore it is important to develop thermal design methods which incorporate the effects of radiation.

1.2 Scope of Dissertation

The objectives of the present dissertation are to develop and investigate geometric design methods for conducting solids cooled by multimode heat transfer, including thermal radiation, and to investigate the influence of radiation on the predicted optimal geometries and thermal performance. The overall goal of implementing the design methods is to determine solid configurations that result in reduced or minimal overall thermal resistances. To achieve these objectives, first, a heuristic evolutionary design method (EDM) is introduced which utilizes a discrete description of the solid material distribution and iteratively adjusts the solid shape based on local surface heat fluxes and temperatures. The EDM is first applied to a conjugate conduction-free convection problem and compared to the results of a benchmark TO method (paper **P1**). Then, the effects of radiation are incorporated into the physical model and EDM (paper **P2**). Because the EDM does not require evaluation of the sensitivity information (partial derivatives), incorporating the effects of radiation is straightforward.

Next, to isolate the effects of radiation, a conjugate conduction-radiation problem, in which free convection is assumed to be negligible, is considered, and a heuristic solid growth method (SGM) similar to the EDM is introduced (paper **P3**). The SGM is distinct in that solid material is incrementally added to the domain so that the amount of solid is not constant throughout the design process. The results of the SGM are compared to those of a formal TO method that neglects the effects of radiation in obtaining optimal solid shapes. Lastly, a formal TO method which incorporates the effects of radiation is developed and applied to a conjugate conduction-radiation problem (paper **P4**). A novel dual solid method (DSM) is introduced which utilizes both a continuous and discrete description of the solid distribution. The continuous distribution is used for adjusting the solid shape, while the discrete distribution is used to evaluate radiation heat transfer. Descriptions of the various design methods described in this dissertation are presented in Table 1.

This dissertation is presented in the summary format and consists of the four publications introduced above. An overview of the publications will be organized by the design method implemented: EDM – negligible radiation (Paper **P1)**, EDM – significant radiation (Paper **P2**), SGM (Paper **P3**), and DSM (Paper **P4**). Each overview will summarize the numerical modeling, design method implementation, and

results of the studies. Finally, a brief comparison of the various design methods will be discussed. The publications can be found in their entirety at the end of the dissertation.

Table 1 Descriptions of design methods.

Design Method	Description
Evolutionary Design Method (EDM)	A heuristic, constant mass method in which the solid shape is iteratively adjusted based on local surface heat fluxes and temperatures. This design method is novel and was developed over the course of the dissertation.
Solid Growth Method (SGM)	A heuristic, non-constant mass method in which solid material is iteratively added to the domain based on local surface heat fluxes. This design method is novel and was developed over the course of the dissertation.
Topology Optimization (TO)	A formal optimization method in which the solid shape is iteratively adjusted based on sensitivity (partial derivative) information.
Dual Solid Method (DSM)	A formal TO method which utilizes both a continuous and discrete description of the solid material distribution. This design method is novel and was developed over the course of the dissertation.

Evolutionary Design Method – Negligible Radiation (Paper P1) 2

An overview of Paper **P1** is provided here, and the publication can be found in its entirety in Chapter 8.

2.1 Physical and Numerical Modeling

The physical situation considered by paper **P1** is depicted in Fig. 1, in which a two-dimensional, square domain is filled with a specified amount of solid and an incompressible, Boussinesq fluid. The top boundary is isothermal and there is an applied heat rate at the bottom center of the domain. All other boundaries are adiabatic. The initial solid geometry is a semicircle of radius, *R*. The effects of radiation are assumed to be negligible. In all physical problems considered in this dissertation, it is assumed that the conditions are steady-state, the thermophysical properties are constant, and viscous dissipation is negligible. As mentioned previously, the goal of all four studies is to determine solid shapes which result in low overall thermal resistances, which for the given boundary conditions is defined as $R_t' \equiv [T(H/2,0) - T_o]/q'$.

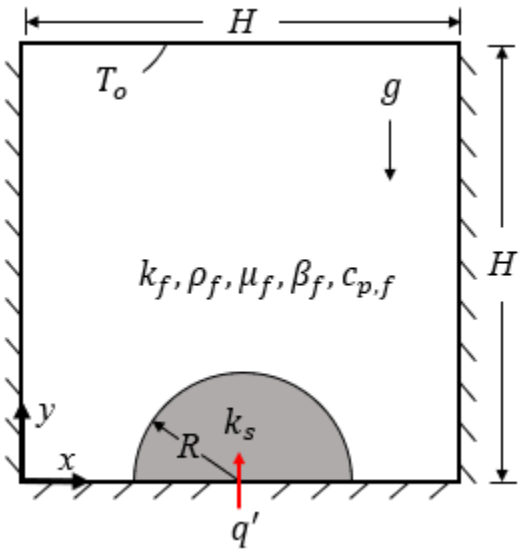

Fig. 1 The computational domain including thermal boundary conditions, thermophysical properties, and the initial solid shape [**P1**].

2.1.1 Governing Equations

The temperature distributions are obtained by solution of (*i*) the conservation of mass, (*ii*) the Navier-Stokes equations, and (*iii*) the conservation of energy. In the fluid, the governing equations are expressed as

$$\frac{\partial(\rho_f u)}{\partial x} + \frac{\partial(\rho_f v)}{\partial y} = 0 \tag{1}$$

$$\frac{\partial(\rho_f uu)}{\partial x} + \frac{\partial(\rho_f uv)}{\partial y} = -\frac{\partial p}{\partial x} + \mu_f \frac{\partial^2 u}{\partial x^2} + \mu_f \frac{\partial^2 u}{\partial y^2} \tag{2}$$

$$\frac{\partial(\rho_f vu)}{\partial x} + \frac{\partial(\rho_f vv)}{\partial y} = -\frac{\partial p}{\partial y} + \mu_f \frac{\partial^2 v}{\partial x^2} + \mu_f \frac{\partial^2 v}{\partial y^2} + \rho_f g \beta_f \Delta T \tag{3}$$

$$\frac{\partial(\rho_f c_{p,f} uT)}{\partial x} + \frac{\partial(\rho_f c_{p,f} vT)}{\partial y} = \frac{\partial}{\partial x}\left(k_f \frac{\partial T}{\partial x}\right) + \frac{\partial}{\partial y}\left(k_f \frac{\partial T}{\partial y}\right) \tag{4}$$

In the solid the conservation of energy is

$$\frac{\partial}{\partial x}\left(k_s \frac{\partial T}{\partial x}\right) + \frac{\partial}{\partial y}\left(k_s \frac{\partial T}{\partial y}\right) = 0 \tag{5}$$

At the interface between solid and fluid, the heat flux from the solid to the interface due to conduction must be equal to the convection heat flux from the interface to the fluid. A no-slip condition is applied at all boundaries of the domain.

2.1.2 Discretization

Throughout this dissertation, the governing equations are solved using the finite volume method with a uniform mesh and harmonic mean thermal conductivities at the control volume interfaces (Patankar 1980). In Paper **P1**, the SIMPLER algorithm is implemented with a staggered grid and a power-law differencing scheme to solve the Navier-Stokes equations. Each control volume is occupied entirely by either solid or fluid.

2.2 Design Method

The EDM is an iterative process in which the solid shape is adjusted by selectively adding and removing solid material. Numerically, this is accomplished by switching one solid control volume to fluid while concurrently switching one fluid control volume to solid, at each iteration. Note that the amount of solid mass is kept constant throughout the design process. The criterion for selecting which control volumes are switched is based on a shape evolution method (SEM). Four SEMs are considered in Paper **P1**, which are detailed in Table 2. For example, when SEM I is implemented, at each design iteration the fluid control volume along the solid-fluid interface that experiences the smallest local surface heat flux from the solid is switched to solid. Concurrently, the solid control volume which experiences the largest local surface heat flux to the fluid is switched to fluid. After the solid shape has been adjusted, Eqs. (1)-(5) are solved again and the process is repeated. The EDM is curtailed once the solid shape is the same as for a previous iteration, or once part of the solid becomes detached from the rest of the solid.

Table 2 Shape Evolution Methods considered in Paper **P1.**

SEM	Add Solid Where	Remove Solid Where
I	Heat Flux is Smallest	Heat Flux is Largest
II	Temperature is Highest	Temperature is Lowest
III	Heat Flux is Largest	Heat Flux is Smallest
IV	Temperature is Lowest	Temperature is Highest

2.3 Results and Discussion

2.3.1 Predicted Solid Shapes and Thermal Performance

The SEMs are exercised with the thermophysical properties and boundary conditions listed in Paper **P1**. The solid shapes at various points throughout the evolution are shown in Fig. 2. Each row of Fig. 2 corresponds to an amount of displaced solid, A_D, and number of design iterations, *iter*. The last solid structure in each column of Fig. 2 is the final solid shape predicted before curtailment of the EDM. As evident, SEM I undergoes the largest transformation, while SEMS II, III, and IV reach curtailment at A_D = 1 mm^2 (*iter* = 4), 7 mm^2 (*iter* = 28), and 8 mm^2 (*iter* = 32) respectively.

The evolution histories of thermal resistance for the four SEMs are shown in Fig. 3. While all four SEMs lead to a reduction in thermal resistance, the largest reduction is associated with SEM I, which has significantly more solid material displaced. The horizontal dashed line of Fig. 3 corresponds to a thermal resistance associated with a replicated benchmark topology optimized solid shape (Coffin and Maute 2016) with the same thermophysical properties and boundary conditions as Paper **P1**. The solid shapes, streamline distributions, and temperature distributions associated with the final results of SEM I and the replicated benchmark TO solid, are shown in Fig. 4. The solid shapes are similar in that they both exhibit highly asymmetrical behavior, and the streamlines and temperature distributions have a strong qualitative agreement. However, the benchmark result has a lower thermal resistance (R_t' = 23.888 m·K/W) compared to that of SEM I (R_t' = 26.126 m·K/W). The higher thermal resistance of SEM I is attributed to the buildup of solid material along the side adiabatic boundary which is relatively thermally inactive.

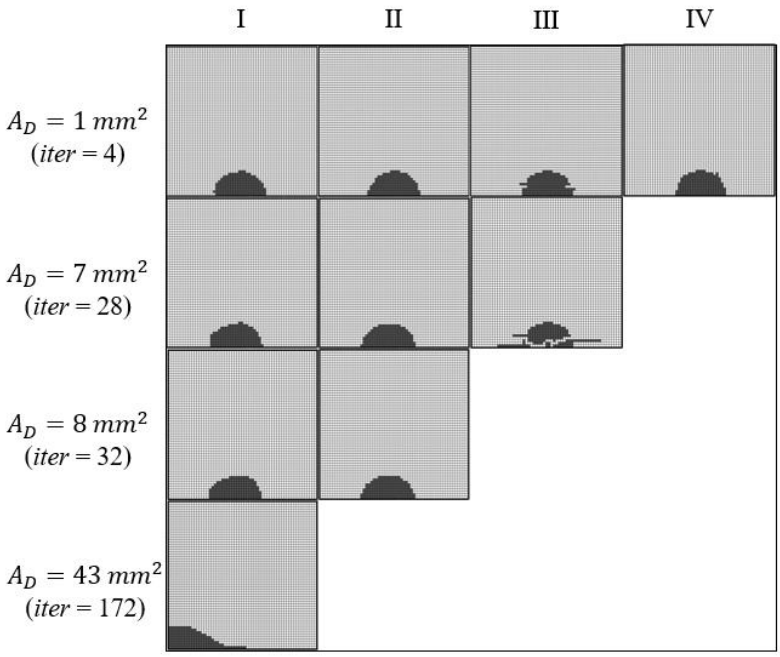

Fig. 2 Solid shapes generated by each of the four SEM sub-models. The final shapes are those at the bottom of each column [**P1**].

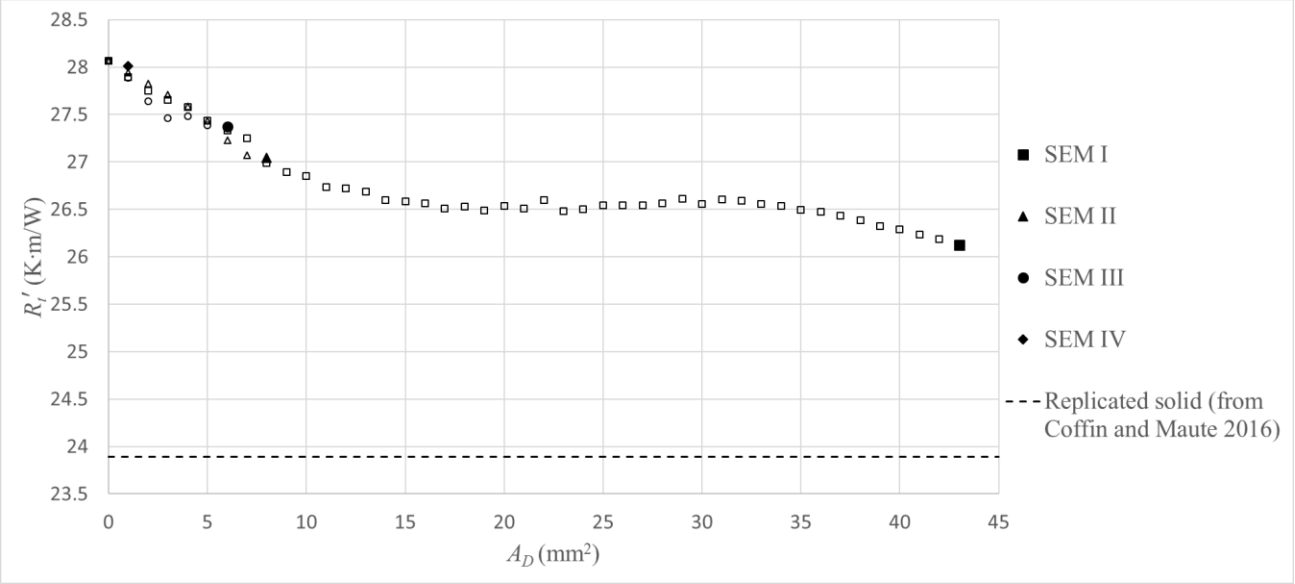

Fig. 3 Evolution of the thermal resistance for each SEM, and that of the benchmark geometry. Filled symbols are associated with the final geometries [**P1**].

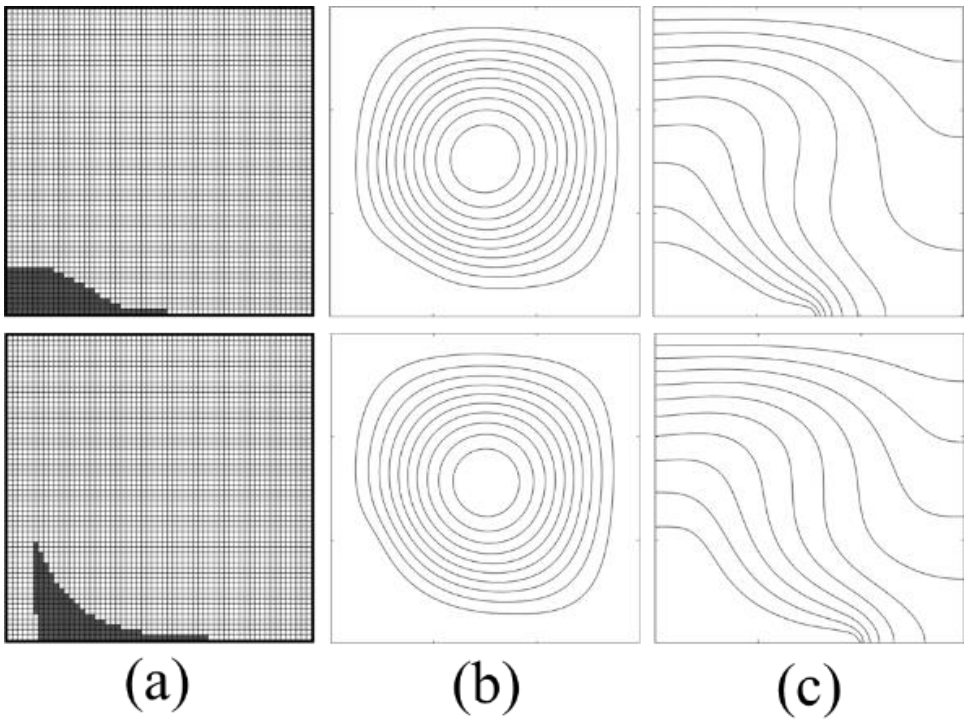

Fig. 4 Predictions of (a) final solid geometry, (b) streamline distribution, (c) temperature distribution associated with (top) SEM I and (bottom) the replicated benchmark topology optimized solid from (Coffin and Maute 2016) [**P1**].

2.3.2 Implementation of a Cutoff Constraint

To prevent the build-up of solid material along the side adiabatic boundary, a cutoff constraint is introduced into SEM I. The constraint prevents solid material from being added to locations where the local surface heat flux is less than 5% of the maximum local surface heat flux in the domain. The resulting solid shape, streamline distribution, and temperature distribution are shown in Fig. 5. While the cutoff constraint effectively prevents the solid from contacting the side adiabatic boundary, the thermal resistance (R_t' = 26.119 m·K/W) is approximately the same as the final solid shape without the cutoff constraint (R_t' = 26.126 m·K/W)

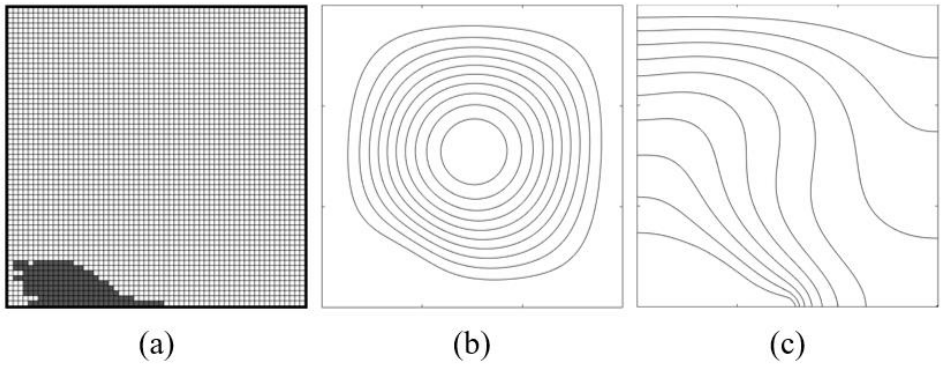

Fig. 5 EDM predictions using SEM I with cutoff constraint: (a) final solid geometry, (b) streamline distribution, (c) temperature distribution [**P1**].

2.3.3 Parametric Simulations

To investigate the effects of conduction and convection on the predicted solid shape and thermal performance, the EDM is exercised with different solid thermal conductivities and domain sizes (Rayleigh number). The predicted solid shapes using SEM I with various solid thermal conductivities are shown in Fig. 6. Surprisingly, the k_s = 23.7 W/m·K case exhibits a lower thermal resistance than that of the k_s = 237 W/m·K case. This is attributed to the modest differences in the solid shape between Figs. 6a and 6b. For the k_s = 2.37 W/m·K case (Fig. 6c), less solid is displaced, therefore the solid material resides lower in the domain and the thermal resistance is higher.

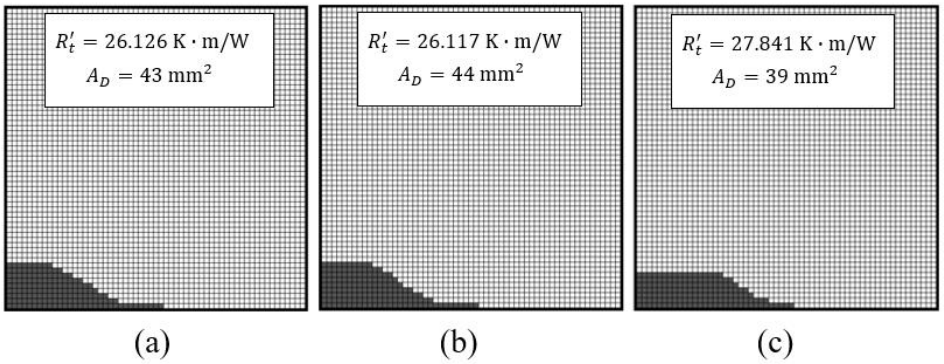

Fig. 6 Predicted solid shape and thermal resistance for SEM I, R_C = 0: (a) k_s = 237 W/m·K, (b) k_s = 23.7 W/m·K, (c) k_s = 2.37 W/m·K [**P1**].

The predicted solid shapes for three different domain sizes, *H*, are reported in Fig. 7. Increasing the size of the domain strengthens convection, as quantified by the Rayleigh number which is defined as $Ra = g\beta_f \Delta T H^3 / \nu_f \alpha_f$. As evident from Fig. 7, this results in a decrease in the overall thermal resistance. The solid shapes also reach slightly higher in the domain and bear a closer resemblance to the benchmark

structure of Fig. 4a. The influence of the cutoff constraint on the parametric simulations is also reported in Paper **P1**. While the added constraint does affect the solid shape, it leads to only a modest reduction in the thermal resistances.

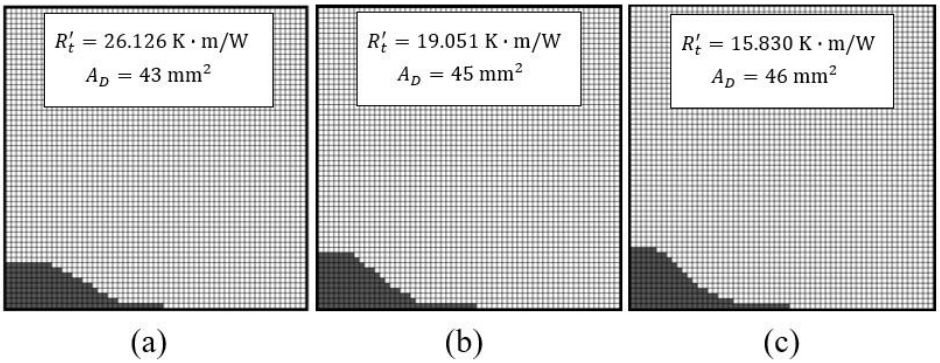

Fig. 7 Predicted solid shape and thermal resistance for SEM I, $R_C = 0$: (a) H = 30 mm (Ra = 4460), (b) H = 45 mm (Ra = 10980), (c) H = 60 mm (Ra = 21620) [**P1**].

Evolutionary Design Method – Significant Radiation (Paper P2) 3

An overview of Paper **P2** is provided here, and the publication can be found in its entirety in Chapter 8.

3.1 Physical and Numerical Modeling

The physical situation considered in Paper **P2** is identical to that of **P1** save that radiation is no longer assumed negligible. Throughout the remainder of this dissertation, the following assumptions apply to the modeling of thermal radiation: (*i*) all exposed surfaces are assumed to be diffuse, opaque, and gray, (*ii*) all surfaces are characterized by the same emissivity, ε, and (*iii*) the fluid is assumed to be radiatively transparent. The initial solid shape is again specified to be a semicircle of radius, *R*.

3.1.1 Governing Equations

The temperature distributions are calculated by solving the same governing equations as Paper **P1** (Eqs. (1) – (5)). However, at the solid-fluid interface, the heat flux from the solid to the interface due to conduction is now equal to the combined convection and radiation heat fluxes leaving the interface, that is

$$-k_s \frac{\partial T}{\partial n} = q''_{conv} + q''_{rad} \tag{6}$$

The condition at the exposed adiabatic boundary is expressed as

$$q''_{conv} + q''_{rad} = 0 \tag{7}$$

or

$$-k_f \frac{\partial T}{\partial n} + q''_{rad} = 0 \tag{8}$$

The remaining boundary conditions are straightforward and are detailed in Section 2.1 of Paper **P2**.

3.1.2 Discretization

The same numerical methods described in Section 2.1.2 are implemented in Paper **P2** for the discretization. However, the boundary condition of Eq. (6) is approximated by incorporating a source term distribution, $S_{rad}(x, y)$, into the energy equation and the adiabatic boundary condition is satisfied by setting the boundary temperature such that it satisfies Eq. (8). Due to the coupled nature of the heat transfer processes, an iterative solution is required as follows: (*i*) first, Eqs. (1)-(5) are solved without the effects of radiation ($S_{rad}(x, y) = 0$), then (*ii*) the radiation heat fluxes are evaluated as will be detailed in Section 3.1.3, next (*iii*) the source terms are adjusted ($S_{rad}(x, y) \neq 0$) and the boundary temperatures are set, then (*iv*) the governing equations are solved again. Steps (*ii*) – (*iv*) are repeated until the maximum relative change in local temperature is less than 10^{-8}.

3.1.3 Radiation Modeling

The source term distribution and boundary temperatures used to incorporate the effects of radiation depend on the local radiation heat fluxes. By assuming the temperature of each control surface is that of the adjacent solid control volume, the net radiative heat flux from a given control surface, i, is calculated as (Bergman and Lavine 2017)

$$q_i'' = \frac{E_{bi} - J_i}{(1-\varepsilon_i)/\varepsilon_i}, \tag{9}$$

where $E_{bi} = \sigma T_i^4$ and

$$\frac{E_{bi} - J_i}{(1-\varepsilon_i)/\varepsilon_i} = \sum_{j=1}^{N} F_{ij}(J_i - J_j) \tag{10}$$

The method used to evaluate the view factors, F_{ij}, is described in detail in Section 2.3 of Paper **P2**. In short, the view factors are first either calculated using Hottel's crossed string method (Hottel 1954) or set to zero based on whether or not a center-to-center ray between the surfaces is obstructed. Then all partially obstructed view factors are adjusted such that the summation and reciprocity requirements are satisfied (Bergman and Lavine 2017).

3.2 Design Method

The EDM detailed in Section 2.2 with SEM I is implemented here. Solid is added to the location of the smallest combined (radiation + convection) local surface heat flux and removed from the location of the largest combined local surface heat flux. The design process ends once the solid begins to oscillate between two shapes from iteration-to-iteration. As will be shown in the following section, the overall thermal resistance does not necessarily decrease at every design iteration. Therefore, the EDM is allowed to proceed until it reaches an oscillation point, and then the solid shapes associated with the lowest overall thermal resistances will be reported as the predicted optimal solid shapes.

3.3 Results and Discussion

3.3.1 Influence of Radiation on Thermal Behavior

To demonstrate the influence that radiation has on the thermal behavior, the heat transfer sub-model is first applied to the initial geometry with a range of emissivities, the results of which are shown in Fig. 8. As evident, increasing the strength of radiation (ε) causes the fluid flow and temperature distributions to be more symmetric about the vertical centerline. This phenomenon is a result of radiation decreasing local temperatures and, therefore, buoyancy forces as described in Section 3.1 of Paper **P2**.

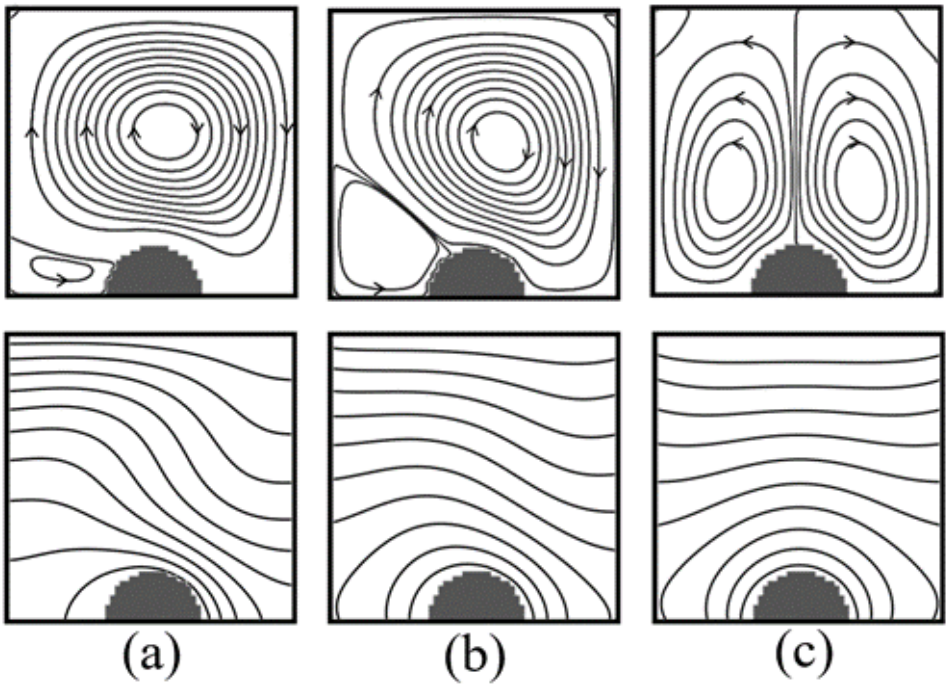

Fig. 8 Streamlines (top) and temperature distributions (bottom) associated with H = 30 mm and the initial semicircular geometry (R/H = 1/6, b/H = 1/30, Ra^* = 199,100). (a) ε = 0, (b) ε = 0.1, (c) ε = 0.2. Temperature distributions are generated by plotting 12 evenly spaced isothermal contours between and including the maximum and minimum temperature [**P2**].

3.3.2 Predicted Solid Shapes and Thermal Performance

The EDM is applied to various domain sizes and emissivities. The evolution histories of thermal resistance for H = 30 mm and a range of emissivities are shown in Fig. 9. The solid shapes and streamlines associated with the minimum thermal resistance are reported in Fig. 10. As mentioned previously, increasing the strength of radiation causes the thermal behavior to be more symmetric. As a result, the predicted optimal geometries of Fig. 10 become more symmetric as ε is increased, and the EDM reaches an oscillation point early into the design process for $\varepsilon \geq 0.15$ (Fig. 9). The evolution histories of thermal resistance for the H = 60 mm cases are shown in Fig. 11, and the corresponding solid shapes and streamlines associated with the minimum thermal resistance are reported in Fig. 12. As the strength of advection is increased, the influence of radiation on fluid flow is weakened and the thermal behavior is less symmetric (Fig. 12). As a result, the solid shapes undergo a greater transformation, and the predicted optimal solid shapes are not achieved as early in the design process (Fig. 11).

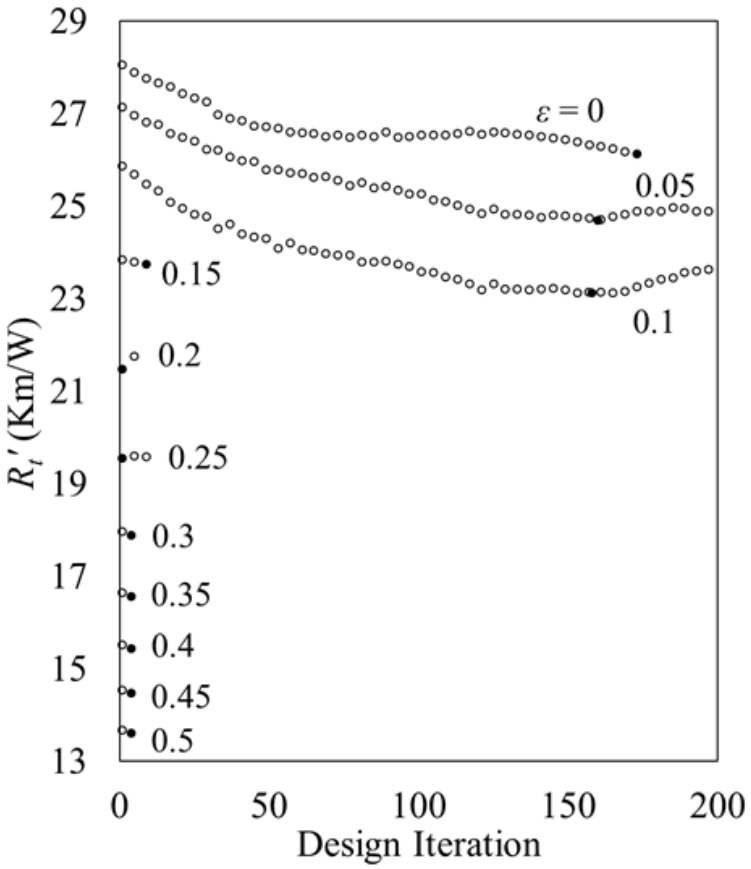

Fig. 9 Evolution history of thermal resistance for H = 30 mm, Ra^* = 199,100. Solid markers designate minimum thermal resistance [**P2**].

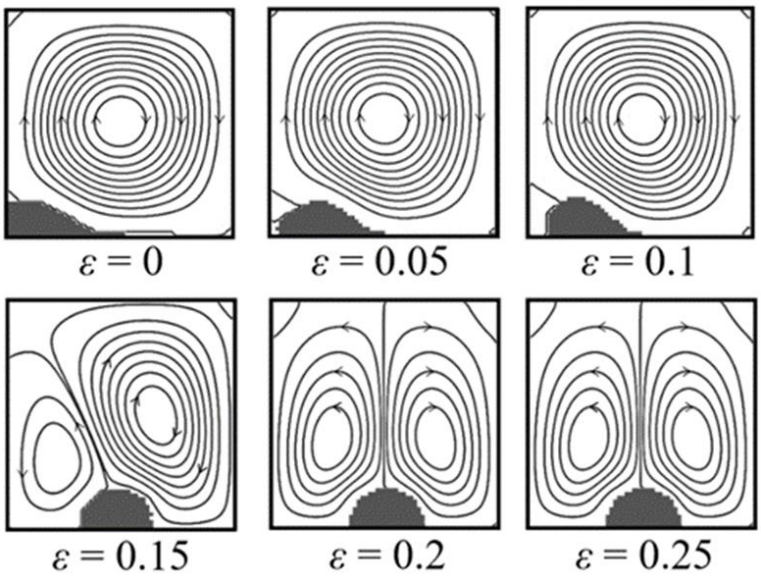

Fig. 10 Solid shape and streamlines associated with the minimum thermal resistances (solid markers in Fig. 5) of the H = 30 mm, Ra^* = 199,100 cases. Qualitatively, the streamlines of the $\varepsilon \geq 0.30$ cases are similar to those of the $\varepsilon = 0.25$ case. Note the sharp transition in the fluid flow and the solid shape at $\varepsilon \approx 0.2$ [**P2**].

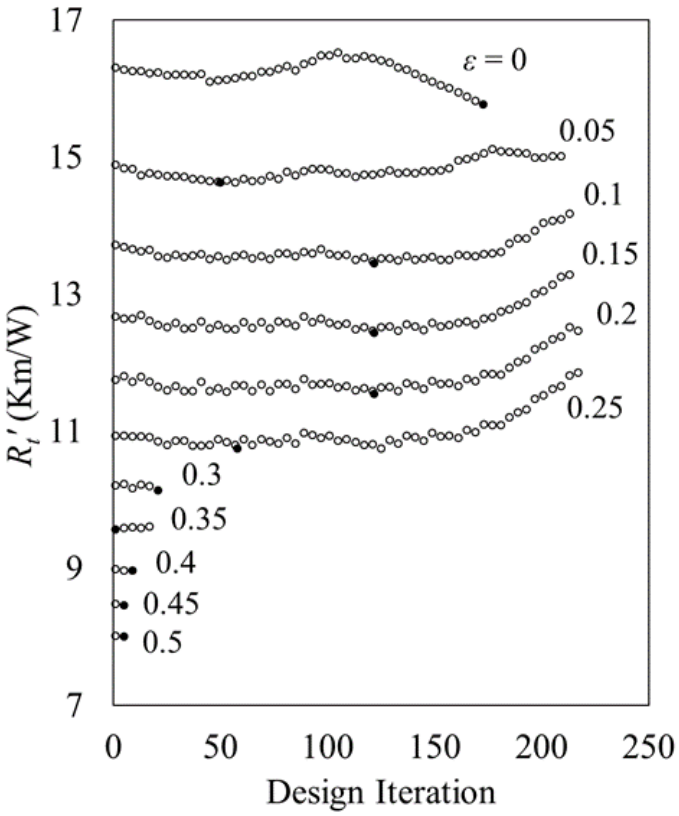

Fig. 11 Evolution history of thermal resistance for H = 60 mm, Ra^* = 1,592,000. Solid markers designate minimum thermal resistance [**P2**].

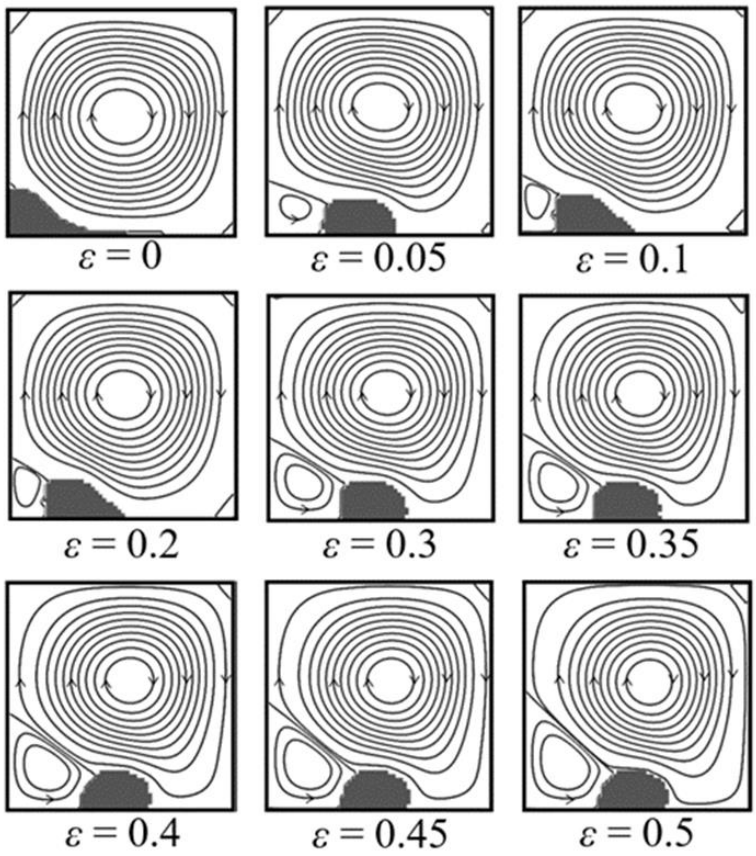

Fig. 12 Solid shape and streamlines associated with the minimum thermal resistances (solid markers in Fig. 7) of the H = 60 mm, Ra^* = 1,592,000 cases [**P2**].

3.3.3 Impact of Radiation and the EDM on Overall Thermal Resistance

To quantify the influence of (*i*) the strength of radiation and (*ii*) the reconfiguration of the solid shape on the overall thermal resistance, two parameters are introduced. For a given H and ε case, the influence of radiation is calculated as the relative difference between the minimum thermal resistance of the $\varepsilon = 0$ case with the same H and the minimum thermal resistance of that particular case:

$$\hat{R}'_{t,1} = \frac{R'_{t,min}(\varepsilon=0) - R'_{t,min}}{R'_{t,min}(\varepsilon=0)} \tag{11}$$

The results of this parameter are shown in Fig. 13. In general, $\hat{R}'_{t,1}$ increases with ε. The decrease in $\hat{R}'_{t,1}$ between $\varepsilon = 0.1$ and 0.15 of the $H = 30$ mm case is due to the severe differences in predicted optimal solid shape (Fig. 10).

The influence of the reconfiguration of solid on the overall thermal resistance is quantified as the relative difference between the initial thermal resistance and the minimum thermal resistance

$$\hat{R}'_{t,2} = \frac{R'_{t,i} - R'_{t,min}}{R'_{t,i}} \tag{12}$$

which is plotted in Fig. 14. The greatest reductions are experienced by the $H = 30$ mm, $\varepsilon \leq 0.1$ cases. Unsurprisingly, the smallest reductions are associated with the higher emissivities, for which the solid shape did not deviate much from its initial semicircular geometry.

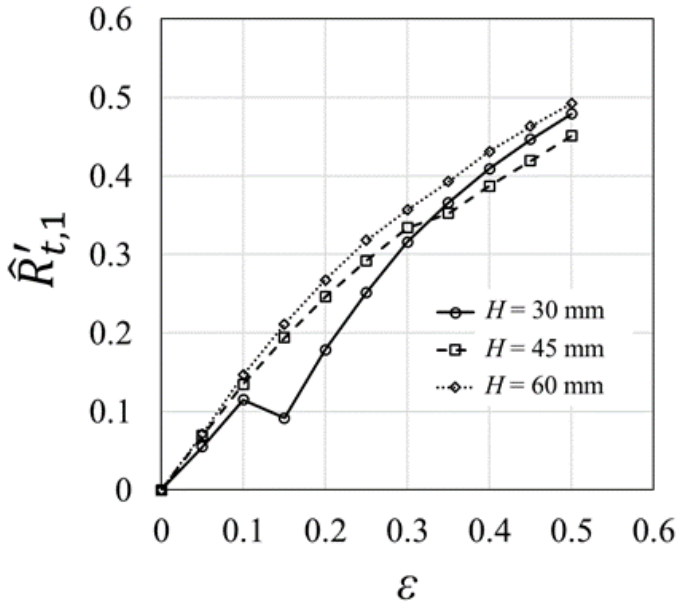

Fig. 13 Relative reduction between $\varepsilon = 0$ minimum thermal resistance and minimum thermal resistance of each emissivity value [**P2**].

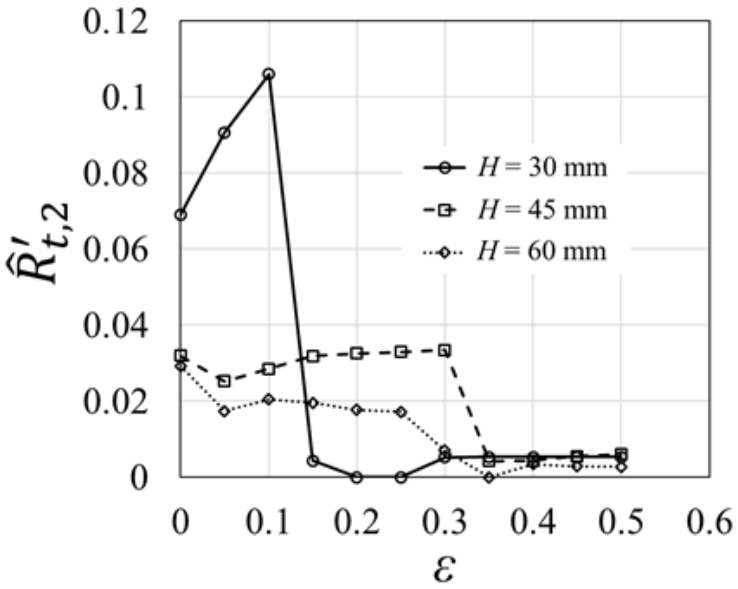

Fig. 14 Relative reduction between initial and minimum thermal resistance [**P2**].

Solid Growth Method (Paper P3) 4

An overview of Paper **P3** is provided here, and the publication can be found in its entirety in Chapter 8.

4.1 Physical and Numerical Modeling

The physical situation considered in both Paper **P3** and **P4** is shown in Fig. 15. The physical problem is identical to that of Paper **P2**, but now it is assumed that buoyancy effects are negligible. Therefore, the conducting solid is cooled by (*i*) surface radiation and (*ii*) conduction in a stagnant fluid. The solid material is restricted to the section of the domain below $y = y_{max}$. The initial solid shape is a small rectangular section of solid placed at the location of the applied heat rate. Throughout the design process, solid material is iteratively added to the domain, thus increasing the solid mass.

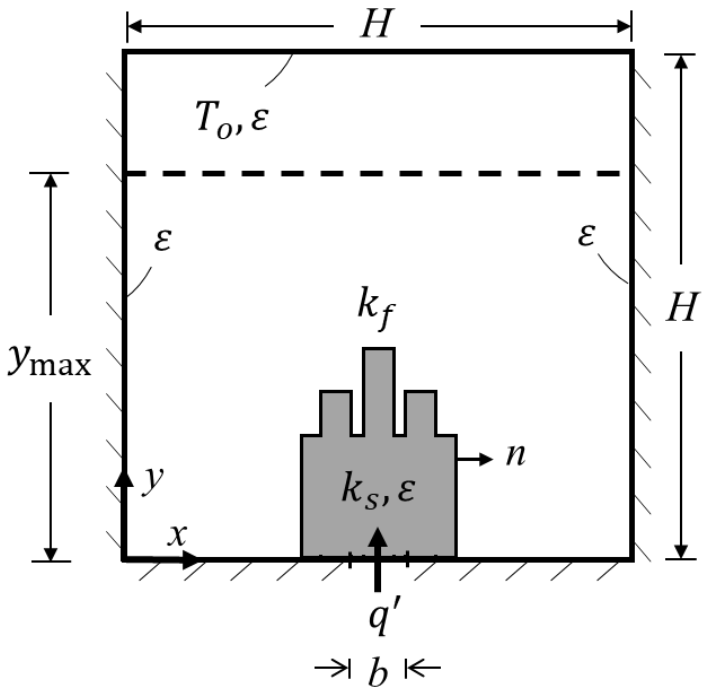

Fig. 15 Physical domain and boundary conditions [**P3**].

4.1.1 Governing Equations

Since there is no fluid motion, the temperature distribution in both the solid and fluid is governed only by the heat diffusion equation, Eq. (5). The boundary conditions are very similar to that of Paper **P2**, however, at the solid-fluid interface, the balance of heat fluxes is now described as

$$-k_s \frac{\partial T}{\partial n} = -k_f \frac{\partial T}{\partial n} + q''_{\text{rad}} \tag{13}$$

The discretization and radiation modeling are the same as detailed in Section 3.1 of this dissertation.

4.2 Design Method

The SGM begins with a small amount of solid material (2 computational control volumes) at the location of the applied heat rate. The governing equation is solved, and the combined (radiation + conduction) local surface heat fluxes are calculated. Solid material is then added to the location with the largest heat flux. Without fluid flow, it is expected that the heat transfer processes be horizontally symmetric, therefore symmetry is enforced on the solid growth. At each design iteration, two control volumes (one on the left-hand side of the domain and one at the corresponding location of the right-hand side) are switched from fluid to solid. Through an investigation not detailed in Paper **P3**, it was determined that the best thermal performance was achieved by adding solid material at the location of the largest heat flux, rather than the smallest. This is in direct contradiction to the results of Paper **P1** and is attributed to the differences in the physical problem being considered.

The results of the SGM are compared to a formal TO method which assumes pure conduction and is described in detail in Paper **P4** and Section 5.2.1 of this dissertation. The method utilizes a continuous material distribution, and local thermal conductivities are defined using the Solid Isotropic Material with Penalization method (Bendsoe and Sigmund 2003). The material distribution is optimized using the Method of Moving Asymptotes (Svanberg 1987). To evaluate radiation heat transfer, the optimized continuous distribution is converted to a discrete distribution as described in Section 3 of **P3** and Section 4 of **P4**. In short, the discrete solid is obtained by specifying the control volumes with the highest solid fraction values to be entirely solid and all remaining control volumes to be entirely fluid. With the discrete solid obtained, the coupled radiation-conduction problem is solved as detailed in Section 3.1 of this dissertation. Note that the TO solid shapes reported in Paper **P3** were obtained by a process that neglects the effects of radiation.

4.3 Results and Discussion

The SGM is applied with ε = 0 and 0.4 for k_s^* = 1 and 0.1, where $k_s^* \equiv k_s/(237\ \text{W/m} \cdot \text{K})$. A figure of merit is introduced which rewards both low overall thermal resistance and low amount of solid and is defined as $F \equiv (R'_{\text{tot}} \cdot k_f \cdot A_s/A_{\text{tot}})^{-1}$, where A_s is the cross-sectional area of the solid and A_{tot} is the area of the entire $H \times H$ computational domain. The evolution history of the overall thermal resistance and figure of merit are reported in Fig. 16. The TO method is applied at four arbitrarily selected A_s values, the

results of which are also shown in Fig. 16 as isolated, filled data points. For the $\varepsilon = 0$ SGM cases, R'_{tot} decreases monotonically as solid material is added to the domain, while F undergoes a more complex evolution. In contrast, the $\varepsilon = 0.4$ SGM cases have regions in which R'_{tot} increases as solid material is added. As will be detailed later, this is a result of solid sections shielding radiation transfer.

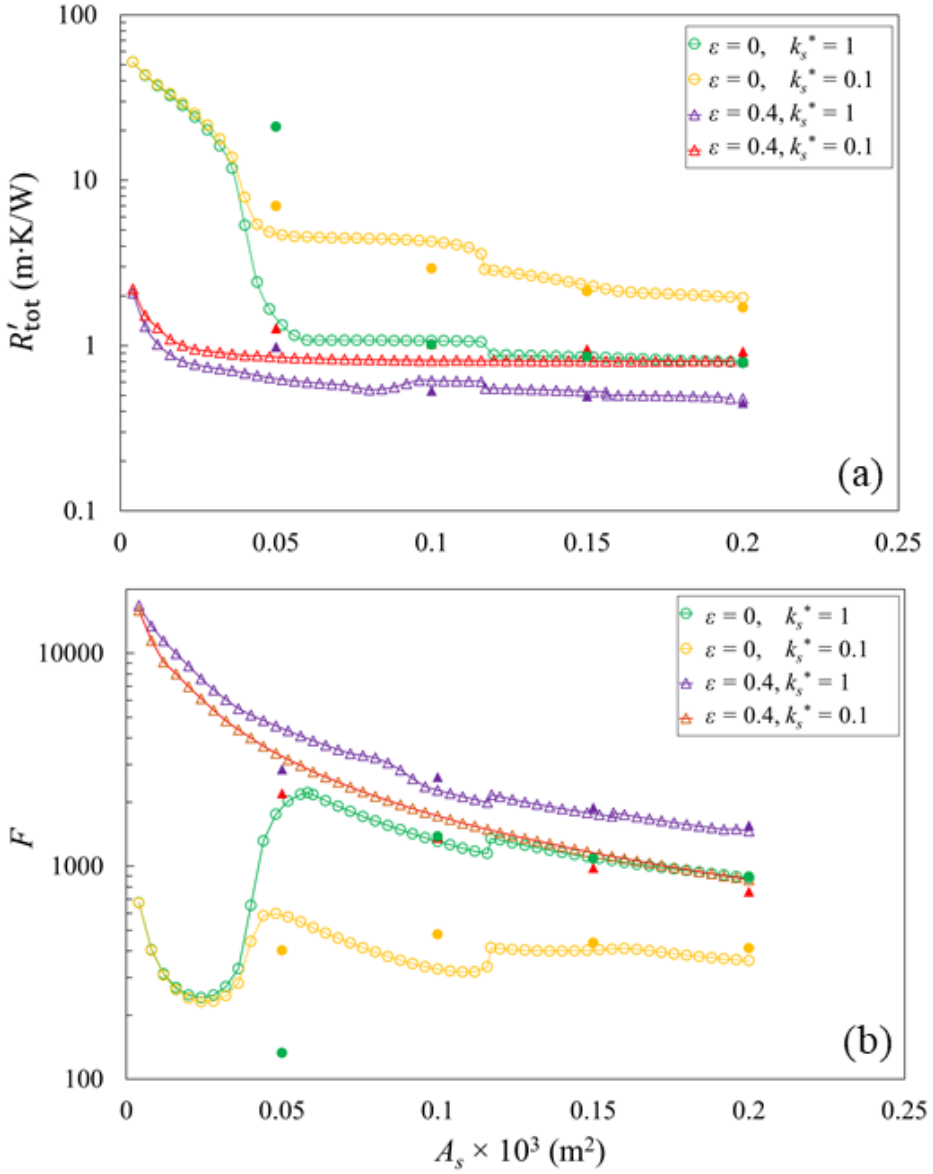

Fig. 16 Evolution history of (a) overall thermal resistance and (b) figure of merit predicted by the SGM. Filled data points correspond to TO predictions [**P3**].

4.3.1 Predicted Solid Shapes and Thermal Performance, $k_s^* = 1$

The corresponding solid configurations and temperature distributions associated with the $k_s^* = 1$ cases are shown in Figs. 17 and 18 respectively. Note that the TO solid shapes are the same for $\varepsilon = 0$ and 0.4, therefore one TO solid is shown for each A_s value. The overall thermal resistance (R'_{tot}), conduction thermal resistance (R'_{cond}), and figure of merit associated with the temperature distributions of Fig. 18, are reported in Table 3. The solid growth processes of the various cases are described in detail in Sections 4.2 and 4.3 of Paper **P3** and are briefly summarized here.

For the $\varepsilon = 0$ case, the solid initially grows upward towards the isothermal top boundary. Once the solid reaches the top of the design domain, it bifurcates outward resulting in the T-shaped structure of Fig. 17a. The horizontal section of solid at the top of the domain continues to expand outward until reaching the side adiabatic boundary, at which point the location of maximum local surface heat flux shifts to the bottom center of the domain. From there, the solid growth results in the additional sections of solid present in the lower half of the domain of Fig. 17b. Once the vertical solid sections along the side adiabatic boundaries come into contact with the top horizontal section of solid, there is a sharp decrease in R'_{tot} (Fig. 16a, $A_s \times 10^3 \approx 0.1165\ \text{m}^2$) which corresponds to a sharp increase in F (Fig. 16b, $A_s \times 10^3 \approx 0.1165\ \text{m}^2$). For the remainder of the growth process, solid is added along the three existing vertical columns, increasing their thickness, as shown in Figs. 17c and 17d.

The inclusion of radiation ($\varepsilon = 0.4$) results in a significantly different growth process, as shown by Figs. 17e - 17h. The solid initially grows outward horizontally, until turning upwards at the side adiabatic boundary. Then the solid growth shifts to the bottom center of the domain resulting in the central vertical section of solid present in Fig. 17e. This central section continues to grow until reaching the top boundary and bifurcating outward (Fig. 17f). As the horizontal section of solid at the top of the domain expands outward, it serves to reduce the conduction thermal resistance but increasingly shields radiation transfer between the high-temperature sections at the bottom of the domain and the colder, top isothermal boundary. As a result, R'_{tot} increases (Fig. 16a, $0.08\ \text{m}^2 \lesssim A_s \times 10^3 \lesssim 0.1\ \text{m}^2$). Later in the design process, the solid growth is characterized by the addition of slender vertical columns near the center of the domain (Figs. 17g and 17h).

The solid configurations resulting from TO (Figs. 17i - 17l) are slightly more complex than the SGM solids. As A_s increases, the TO solid structures are characterized by thicker solid sections with more branching and complexity. For $A_s \times 10^3 = 0.05\ \text{m}^2$ (Fig. 17i), the conversion between continuous and discrete descriptions results in sections of solid which are not fully connected and therefore exhibit an increased conduction thermal resistance (Table 3). For $A_s \times 10^3 > 0.05\ \text{m}^2$, however, the TO solid

structures have conduction resistances of less than or similar value to the SGM cases and the lowest overall thermal resistances. Based on these limited results, it may be concluded that the TO approach produces more desirable structures when a relatively high solid thermal conductivity is considered and sufficient solid is present to minimize numerical effects that artificially increase conduction resistance values.

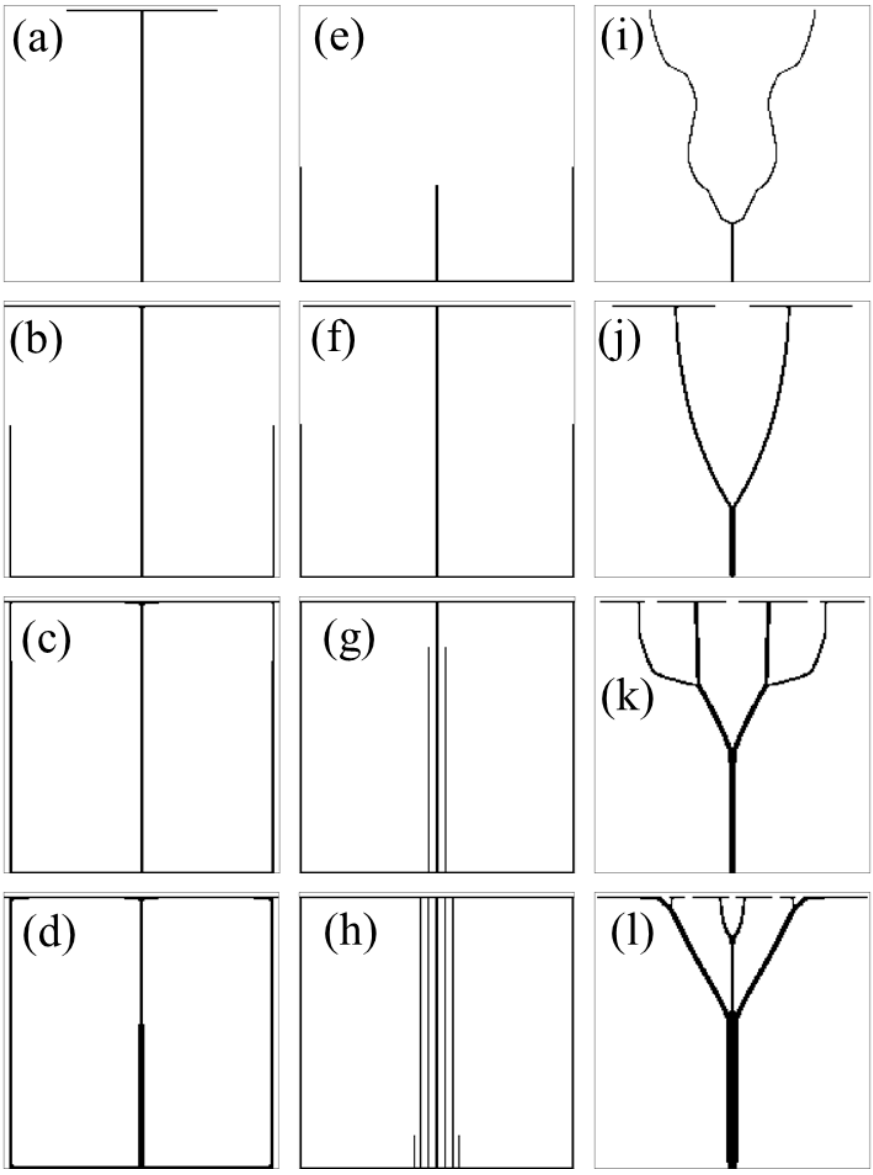

Fig. 17 Solid configurations for $k_s^* = 1$ and the SGM with $\varepsilon = 0$ (left), the SGM with $\varepsilon = 0.4$ (middle), and TO (right) for $A_s \times 10^3 = 0.05$ m^2 (a, e, i), 0.1 m^2 (b, f, j), 0.15 m^2 (c, g, k), and 0.2 m^2 (d, h, l) **[P3]**.

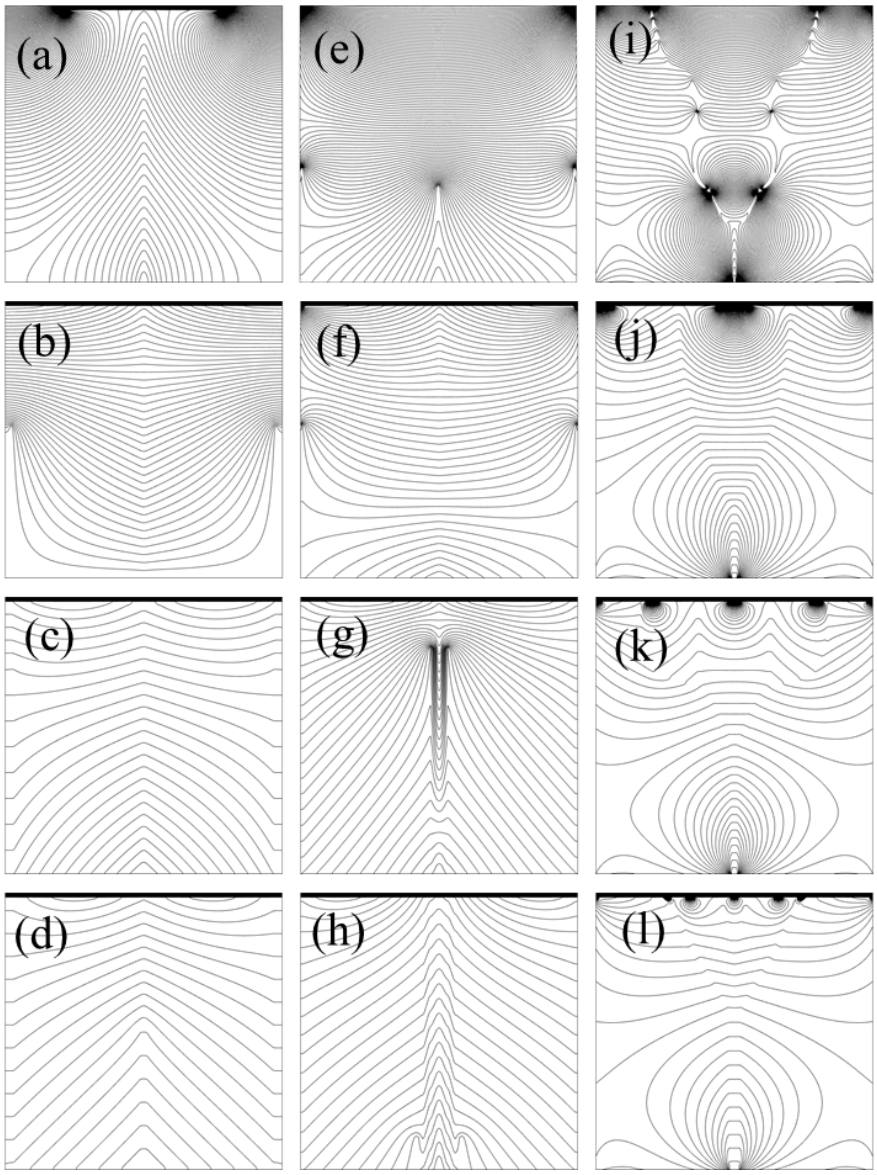

Fig. 18 Temperature distributions for k_s^* = 1 and the SGM with ε = 0 (left), the SGM with ε = 0.4 (middle), and TO (right) for $A_s \times 10^3$ = 0.05 m^2 (a, e, i), 0.1 m^2 (b, f, j), 0.15 m^2 (c, g, k), and 0.2 m^2 (d, h, l) [**P3**].

Table 3 Thermal resistances and figures of merit for $k_s^* = 1$ [**P3**].

$A_s \times 10^3$ (m^2)	Method	$R'_{\mathrm{tot}}(\frac{\mathrm{m \cdot K}}{\mathrm{W}})$	$R'_{\mathrm{cond}}(\frac{\mathrm{m \cdot K}}{\mathrm{W}})$	F
0.05	SGM, $\varepsilon = 0$	1.468	1.468	1909
	SGM, $\varepsilon = 0.4$	0.6307	27.72	4442
	TO, $\varepsilon = 0.4$	0.9816	21.12	2854
0.1	SGM, $\varepsilon = 0$	1.071	1.071	1308
	SGM, $\varepsilon = 0.4$	0.6144	1.080	2280
	TO, $\varepsilon = 0.4$	0.5341	1.015	2623
0.15	SGM, $\varepsilon = 0$	0.8514	0.8514	1097
	SGM, $\varepsilon = 0.4$	0.5286	0.8706	1767
	TO, $\varepsilon = 0.4$	0.4946	0.8591	1888
0.2	SGM, $\varepsilon = 0$	0.7935	0.7935	882.7
	SGM, $\varepsilon = 0.4$	0.4777	0.7783	1466
	TO, $\varepsilon = 0.4$	0.4506	0.7821	1554

4.3.1 Predicted Solid Shapes and Thermal Performance, $k_s^* = 0.1$

Solid configurations and temperature distributions of the $k_s^* = 0.1$ cases are reported in Figs. 19 and 20, respectively, at several A_s values. The thermal resistances and figures of merit associated with the solid configurations of Fig. 19 are reported in Table 4. The solid growth of the $\varepsilon = 0$, $k_s^* = 0.1$ case is nearly identical to the $\varepsilon = 0$, $k_s^* = 1$ case aside from slight differences in the later stages of the growth process, as evident by Figs. 17c, 17d, 19c, and 19d. The solid evolution of the $\varepsilon = 0.4$, $k_s^* = 0.1$ case (Figs. 19e - 19h) is remarkably different than that of the other SGM cases. The solid growth initiates by growing outward horizontally, then a vertical section of solid grows upwards from the bottom center of the domain. The solid evolution is then characterized by the addition and extension of multiple vertical columns near the vertical centerline (Figs. 19e-19f). Eventually, the central column reaches the top of the design domain and bifurcates outward (Fig. 19g). This horizontal section of solid at the top of the domain causes some shielding of radiation heat transfer, as evidenced by the increase in R'_{tot} (0.8063 m·K/W to 0.8101 m·K/W) and decrease in R'_{cond} (4.385 m·K/W to 3.448 m·K/W) between $A_s \times 10^3 = 0.15$ m^2 and 0.2 m^2.

The TO design method again results in branching structures (Figs. 19i - 19l). In comparison to the higher thermal conductivity TO case (Figs. 17i - 17l), the TO solid configurations of the $k_s^* = 0.1$ case

(Figs. 19i - 19l) are of simpler geometry with less branching and a higher concentration of solid near the vertical centerline. For all A_s values other than $A_s \times 10^3 = 0.05\ \mathrm{m}^2$, the TO method achieves the lowest conduction thermal resistance (Table 4). However, the SGM, $\varepsilon = 0.4$ case exhibits a lower overall thermal resistance for all A_s values. This result shows that the SGM achieves a lower thermal resistance due to radiation and therefore results in a preferred solid configuration when the radiation heat transfer is dominant, such as when a low solid thermal conductivity or low amount of solid is considered.

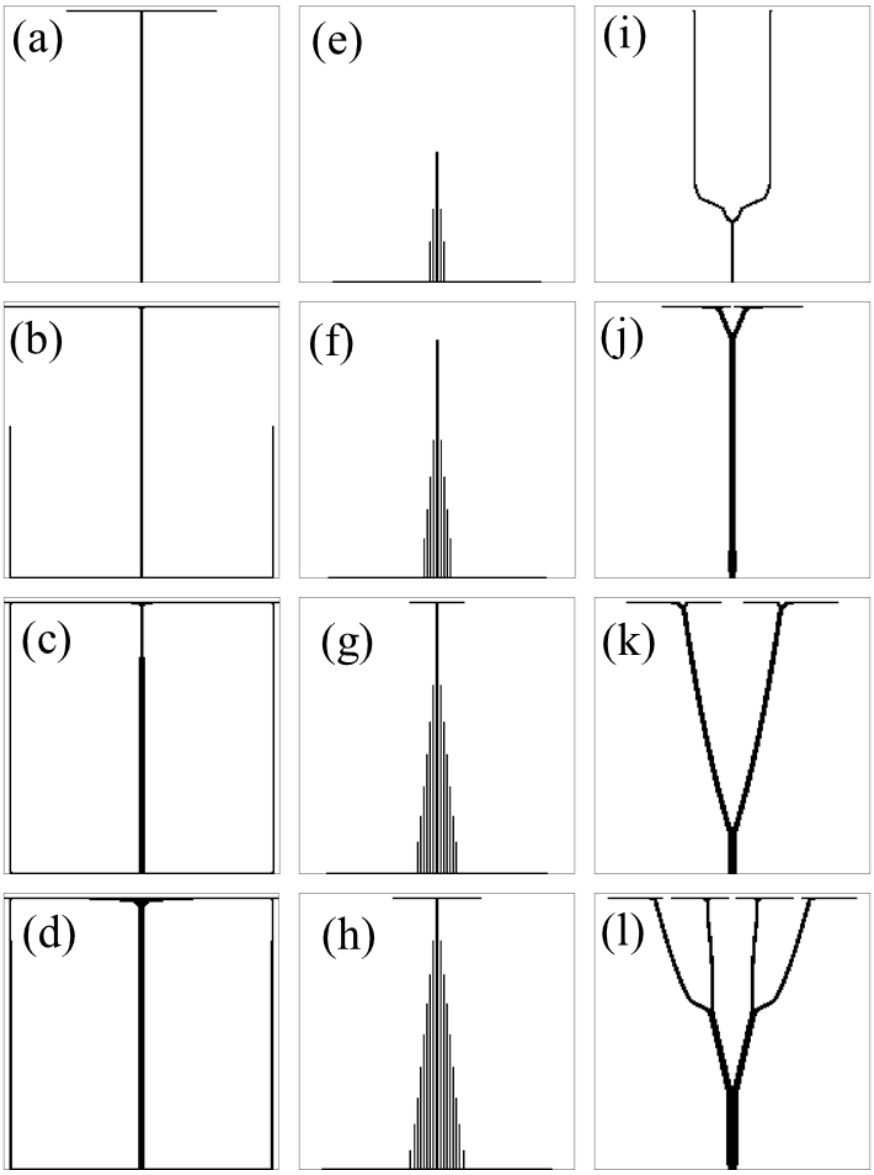

Fig. 19 Solid configurations for k_s^* = 0.1 and the SGM with ε = 0 (left), the SGM with ε = 0.4 (middle), and TO (right) for $A_s \times 10^3$ = 0.05 m^2 (a, e, i), 0.1 m^2 (b, f, j), 0.15 m^2 (c, g, k), and 0.2 m^2 (d, h, l) [**P3**].

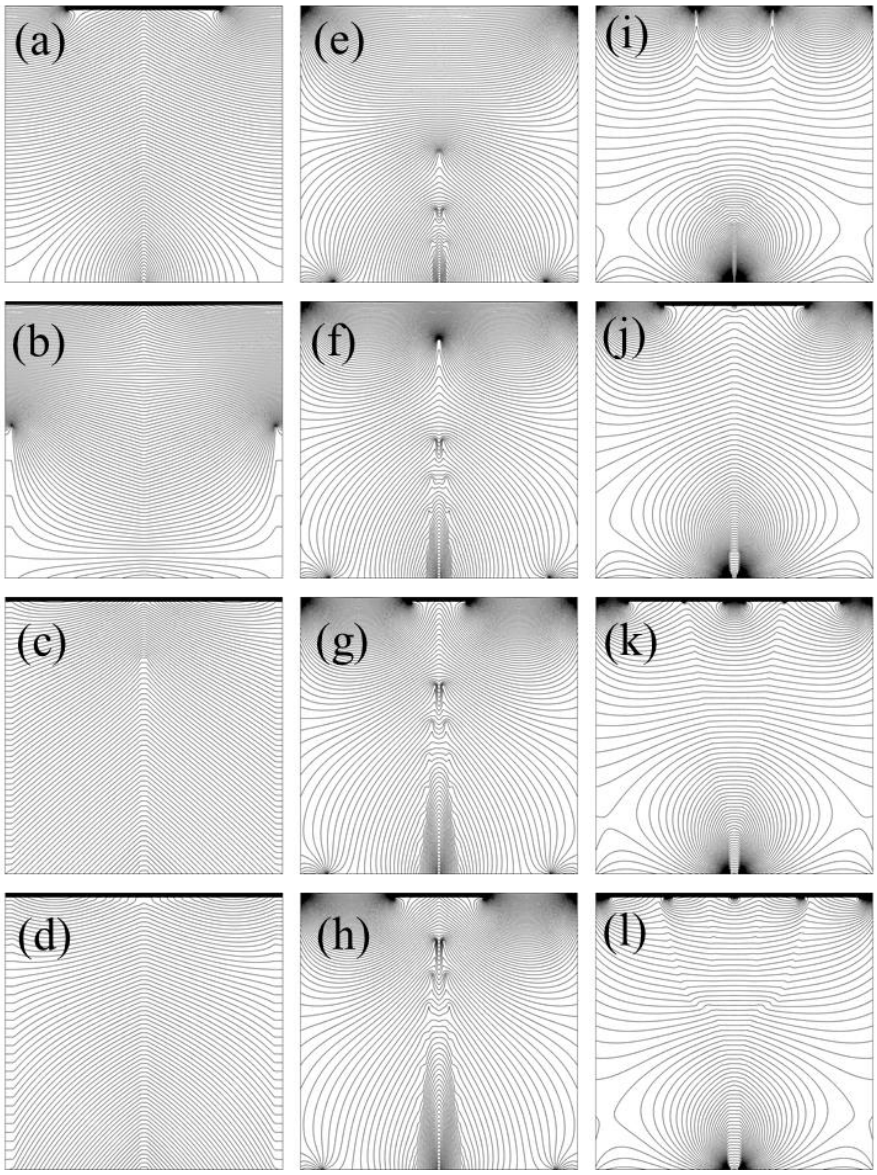

Fig. 20 Temperature distributions for k_s^* = 0.1 and the SGM with ε = 0 (left), the SGM with ε = 0.4 (middle), and TO (right) for $A_s \times 10^3$ = 0.05 m^2 (a, e, i), 0.1 m^2 (b, f, j), 0.15 m^2 (c, g, k), and 0.2 m^2 (d, h, l) [**P3**].

Table 4 Thermal resistances and figures of merit associated with $k_s^* = 0.1$ [**P3**].

$A_s \times 10^3$ (m^2)	Method	$R'_{\mathrm{tot}}(\frac{\mathrm{m \cdot K}}{\mathrm{W}})$	$R'_{\mathrm{cond}}(\frac{\mathrm{m \cdot K}}{\mathrm{W}})$	F
0.05	SGM, $\varepsilon = 0$	4.742	4.742	590.9
	SGM, $\varepsilon = 0.4$	0.8540	28.78	3281
	TO, $\varepsilon = 0.4$	1.274	6.966	2199
0.1	SGM, $\varepsilon = 0$	4.261	4.261	328.7
	SGM, $\varepsilon = 0.4$	0.8134	14.44	1730
	TO, $\varepsilon = 0.4$	1.029	2.926	1362
0.15	SGM, $\varepsilon = 0$	2.317	2.317	403.1
	SGM, $\varepsilon = 0.4$	0.8063	4.385	1158
	TO, $\varepsilon = 0.4$	0.9504	2.135	982.6
0.2	SGM, $\varepsilon = 0$	1.946	1.946	360
	SGM, $\varepsilon = 0.4$	0.8101	3.448	864.6
	TO, $\varepsilon = 0.4$	0.9226	1.696	759.2

Dual Solid Method (Paper P4) 5

An overview of Paper **P4** is provided here, and the publication can be found in its entirety in Chapter 8. The Dual Solid Method, developed during the course of the dissertation, is novel and represents the most rigorous design method presented in this dissertation.

5.1 Physical and Numerical Modeling

The same physical situation considered in Paper **P3** is considered in Paper **P4**. As will be detailed in Section 5.2, the design method relies on both a continuous and discrete description of the solid distribution. The discrete solid distribution is employed to evaluate radiation heat transfer as detailed in Section 4.1 of this dissertation. The continuous distribution is used in conjunction with a topology optimization method to determine optimal solid shapes. Because the discrete description methodology has already been discussed, the following sections are concerned with the governing equations and discretization of the continuous solid model.

5.1.1 Governing Equations: Continuous Solid Distribution

The continuous solid model utilizes a spatial distribution of local solid fraction, $\gamma(x,y)$, where $0 \leq \gamma \leq 1$. Radiation heat transfer is incorporated by a spatially distributed source term, $S_{\mathrm{rad},cm}(x,y)$, that is related to the radiation heat transfer of the discrete solid model and is independent of $\gamma(x,y)$. The heat diffusion equation is recast as:

$$\frac{\partial}{\partial x}\left(k\frac{\partial T}{\partial x}\right)+\frac{\partial}{\partial y}\left(k\frac{\partial T}{\partial y}\right)+S_{\mathrm{rad},cm}(x,y)=0 \tag{14}$$

where local thermal conductivities depend on $\gamma(x,y)$ such that $k_f \leq k \leq k_s$. At the adiabatic boundary

$$-k\frac{\partial T}{\partial n_b}+q_b''=0 \tag{15}$$

where $q_b''=0$ or q_{rad}'' depending on information provided from the discrete model. The remaining boundary conditions are similar to that of the discrete model.

5.1.2 Discretization: Continuous Solid Distribution

Equation (14) is solved using the finite volume method with control volumes co-located with those of the discrete solid model. The Solid Isotropic Material with Penalization (SIMP) method (Bendsoe and Sigmund 2003) is used to calculate local thermal conductivities as

$$k(\gamma)=k_f+\gamma^P(k_s-k_f) \tag{16}$$

where *P* is a penalization parameter. The purpose of the SIMP method is to discourage intermediate solid fraction values and leads to optimal continuous solid distributions that are closer to discrete.

The spatial distribution of source terms present in Eq. (14) is determined from the discrete solid model as

$$S_{\mathrm{rad},cm}(x,y) = S_{\mathrm{rad},dm}(x,y) \tag{17}$$

where $S_{\mathrm{rad},dm}(x,y)$ is the source term distribution of the converged discrete solid model. The boundary condition of Eq. (15) is enforced by specifying the source term at the boundary as:

$$S_{\mathrm{rad},cm}(x,y) = -q_b''/\Delta w \tag{18}$$

where $\Delta w = \Delta x = \Delta y$ is the control volume width.

5.2 Design Method

5.2.1 Topology Optimization

The continuous solid distribution is adjusted using a sensitivity-based TO method for which the objective function

$$f_o(\gamma, T) = T(H/2, 0) \tag{19}$$

is minimized. This is equivalent to minimizing the total thermal resistance subject to

$$\sum_{i=1}^{N} \gamma_i \leq V_o \times N \tag{20}$$

and

$$0 \leq \gamma_i \leq 1 \tag{21}$$

while satisfying the governing equations. Here, γ_i is the solid fraction of an arbitrary control volume *i*, V_o is the total solid fraction of the entire domain, and *N* is the total number of computational control volumes in the domain. The local solid fraction distribution is optimized using the Method of Moving Asymptotes (Svanberg 1987) which relies on the sensitivities of the objective function to the individual solid fraction values, $\partial f_o/\partial \gamma$, to generate a convex approximation of f_o. At each design iteration of the TO process a new convex sub-problem is formed and its solution is taken as the new solid fraction distribution. An adjoint method is used to calculate the sensitivities, which is described in detail in Appendix B of Paper **P4**.

The main components of the TO process are depicted in Fig. 21. Initially, the solid fraction is spatially uniform, $\gamma(x,y) = V_o$, and the radiation source term is specified to be either $S_{\mathrm{rad},cm}(x,y)$ = 0 or $S_{\mathrm{rad},cm}(x,y) = S_{\mathrm{rad},dm}(x,y)$. Then, $k(\gamma)$ is determined based on the SIMP method and the discretized

equations are solved to determine $T(x,y)$ and f_o. The sensitivities are then calculated and filtered (Appendix B of Paper **P4**). Lastly, $\gamma(x,y)$ is adjusted based on the filtered sensitivities using the MMA. This process is repeated until the maximum change in local solid fraction $\Delta\gamma_{\max}$, is less than a convergence criterion, *CC* = 0.001. Note that the optimal solid distribution is dependent on $S_{\mathrm{rad},cm}(x,y)$. Therefore, the iterative process of Fig. 21 must be completed for each unique $S_{\mathrm{rad},dm}(x,y)$ distribution that is transferred from the discrete model by way of Eq. (17).

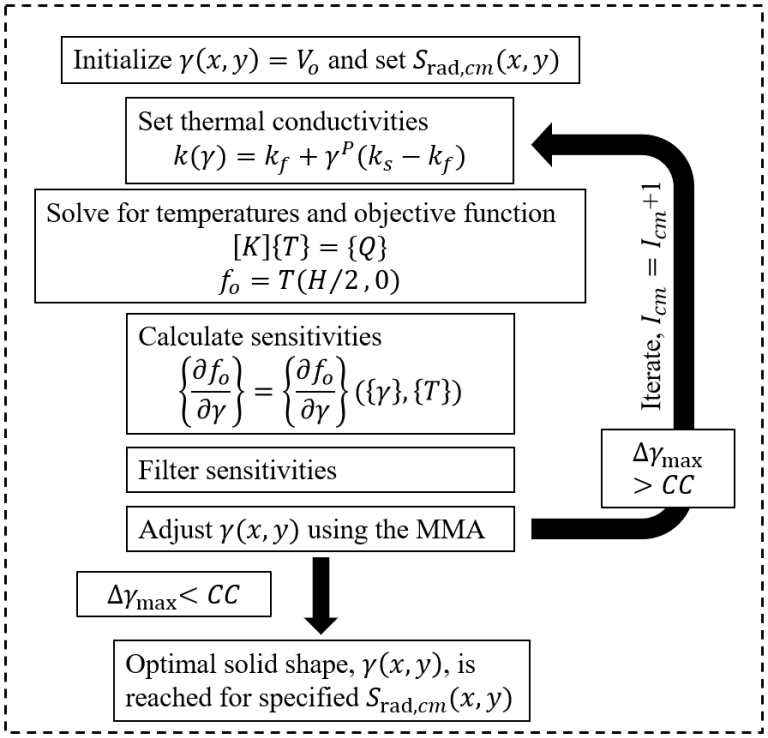

Fig. 21 Topology optimization process for adjusting the continuous solid distribution, $\gamma(x,y)$. I_{cm} = 0 at the start of the first iteration [**P4**].

5.2.2 Dual Solid Method

The DSM process is outlined in Fig. 22. The first step is to obtain the optimal continuous solid distribution for the pure conduction problem ($S_{\mathrm{rad},cm} = 0,\ I_{\mathrm{DSM}} = 0$), using the process of Fig. 21. An equivalent discrete solid distribution is then obtained from the optimal continuous solid distribution. To ensure the total solid fraction, V_o, is the same for both models, the number of solid control volumes in the discrete model is determined from $N_s = V_o \times N$. The solid fraction values, γ, of individual control volumes of the continuous model are sorted, and the N_s control volumes with the largest values of γ are specified to be solid in the discrete solid model. The remaining control volumes are specified to be fluid.

With the equivalent discrete solid obtained, the coupled radiation-conduction problem is solved as detailed previously. The radiation source term distribution of the discrete model is then passed to the continuous model by way of Eq. (17), and the TO process of Fig. 21 is repeated ($I_{\mathrm{DSM}} = 1$, $S_{\mathrm{rad},cm}(x,y) \geq 0$) to obtain a new continuous solid distribution. This process is repeated until (*i*) the discrete solid shape does not change between iterations, (*ii*) the discrete solid shape oscillates between two distinct solid shapes, or (*iii*) a sufficiently large number of iterations have been performed. Note that there are two iteration counters involved in the DSM. Specifically, I_{DSM} tracks the number of times the discrete solid distribution is adjusted (Fig. 22), while I_{cm} tracks the number of times the continuous solid distribution is adjusted for each unique $S_{\mathrm{rad},cm}(x,y)$ (Fig. 21).

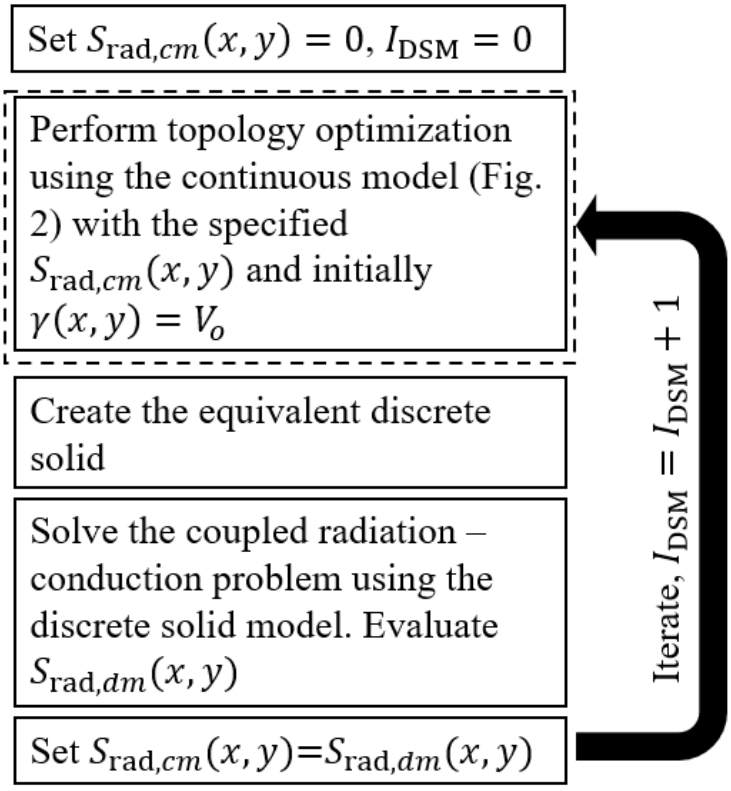

Fig. 22 The dual solid method (DSM) process. Dashed box represents the topology optimization process of Fig. 2. $I_{\mathrm{DSM}} = 0$ for the $S_{\mathrm{rad},cm}(x,y) = 0$ case [**P4**].

5.3 Results and Discussion

5.3.1 Base Case Results

The DSM is first demonstrated in detail for a base case of T_o = 750 K, k_s^* = 1. The first step is to obtain the optimal continuous solid distribution for the pure conduction problem. The evolution history of the thermal resistance associated with the continuous solid distribution through the initial TO process (Fig. 21) as well as the continuous solid distribution for various I_{cm} are reported in Fig. 23. The thermal resistance rapidly decreases as the solid shape converges towards the branching structure shown. The solid distribution becomes more distinct throughout the TO process as a result of the SIMP method (Section 5.1.2). The optimal continuous solid distribution and corresponding temperature distribution for the pure conduction problem are shown in Fig. 24a.

Once the optimal continuous distribution is obtained, an equivalent discrete distribution is generated as described in Section 5.2.2 and is used to solve the coupled radiation-conduction problem. The discrete solid distribution and corresponding temperature distribution with ε = 1 are shown in Fig. 24b. Note that there is a slight increase in the conduction thermal resistance as a result of the mapping between continuous and discrete solid models.

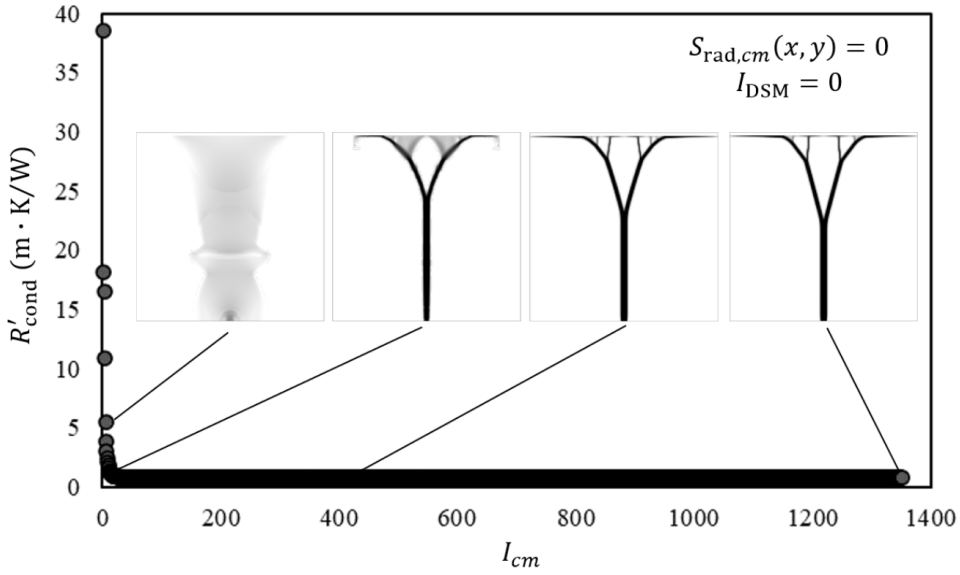

Fig. 23 Pure conduction base case evolution history of the conduction resistance and solid shapes associated with the continuous solid model using the TO process of Fig. 21. Solid distributions are shown at I_{cm} = 5, 20, 400, and 1350 [**P4**].

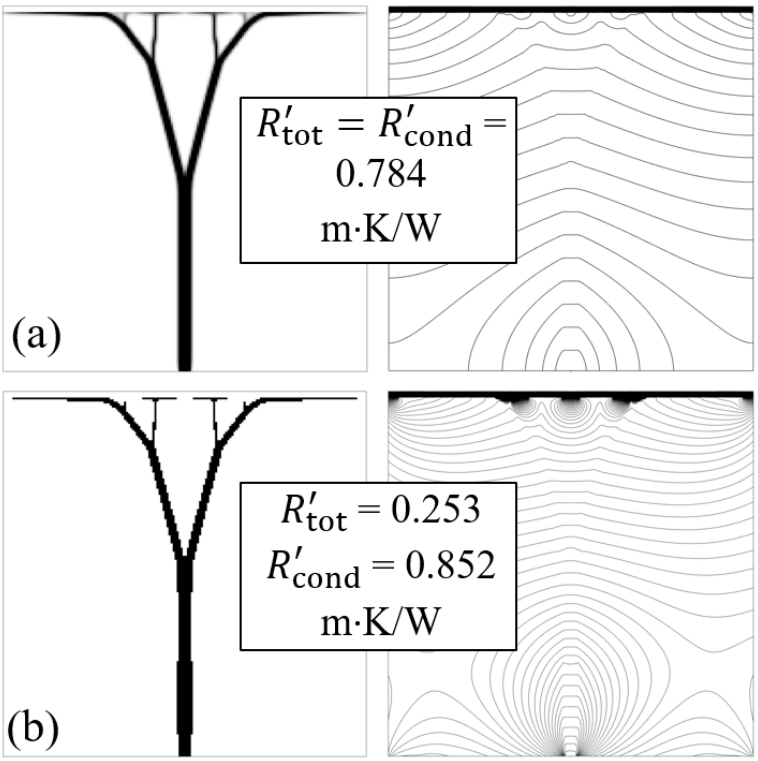

Fig. 24 The base case solid distribution (left) and temperature distribution (right) associated with (a) the optimized continuous solid of the pure conduction solution (I_{cm} = 1350 of Fig. 23), and (b) the equivalent discrete solid with radiation and conduction included (I_{DSM} = 0) [**P4**].

The radiation conditions of Fig. 24b are then incorporated into the TO process of Fig. 21 by way of Eq. (17). The detailed results of I_{DSM} = 1 are also presented in Paper **P4** (Section 5.3, Figs. 6 and 7 of Paper **P4**). After one iteration of the DSM, the incorporation of the radiation source terms results in a slight change to the discrete solid shape and a small reduction in the overall thermal resistance.

The evolution histories of the total and pure conduction thermal resistances associated with the discrete solid model throughout the DSM process are shown in Fig. 25. As evident, there is an initial sharp decrease in the total thermal resistance, coinciding with a sharp increase in the pure conduction resistance. Both resistances approach constant values at $I_{\text{DSM}} \approx 15$, with the total thermal resistance achieving a minimum value at I_{DSM} = 54, as identified by the filled data symbol. The discrete solid distribution and associated temperature distribution at I_{DSM} = 54 are shown in Fig. 26. In comparison to the solid shape of Fig. 24, the points at which the solid branches bifurcate have shifted lower in the domain. Also, the gap at the top of the domain has increased in width, creating a better window for radiation transfer between the top, isothermal boundary and the high-temperature sections at the bottom of the domain. The decrease in overall thermal resistance, along with the increase in conduction thermal

resistance, demonstrate the ability of the DSM to determine solid geometries with enhanced radiation heat transfer.

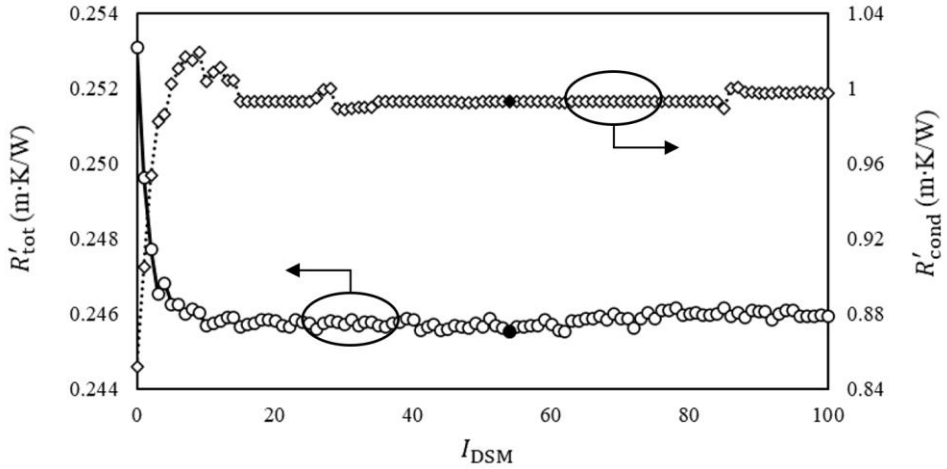

Fig. 25 Base case evolution history of the total pure conduction thermal resistances associated with the discrete solid for the first 100 iterations of the DSM. The minimum total thermal resistance occurs at I_{DSM} = 54 [**P4**].

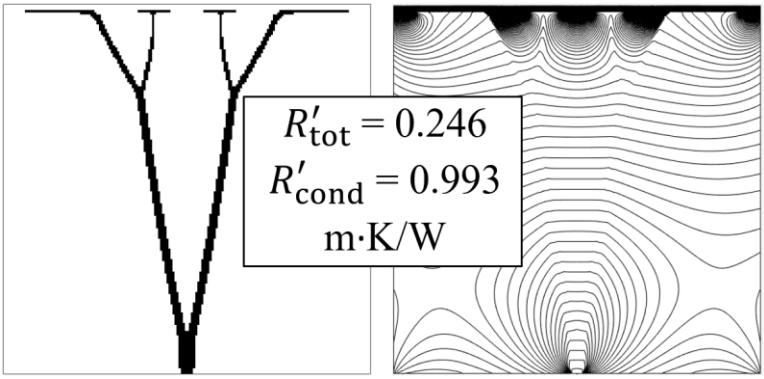

Fig. 26 Base case discrete solid and temperature distributions associated with $R'_{\text{tot,min}}$ the of Fig. 25 at I_{DSM} = 54 [**P4**].

5.3.2 Parametric Simulations

The DSM was then applied to a range of T_o and k_s^* values to determine the influence of the relative strengths of radiation and conduction, respectively, on the predicted optimal geometries and thermal resistances. The evolution histories of the total and conduction thermal resistances associated with the discrete solid distribution for the T_o = 1000 K and 500 K cases are shown in Fig. 27. As evident by Fig. 27a, the overall thermal resistance of the T_o = 1000 K case monotonically approaches the optimal value. In contrast, the T_o = 500 K case (Fig. 27b) exhibits a more complex evolution and struggles to identify an

optimal solution. In fact, the lowest overall thermal resistance is associated with $I_{\mathrm{DSM}} = 0$. Due to the relatively weak strength of radiation for the T_o = 500 K case, the DSM is not able to achieve an overall thermal resistance lower than the solid shape generated from the pure conduction analysis.

The discrete solid shapes and temperature distributions associated with $R'_{\mathrm{tot,min}}$ for the three T_o cases are shown in Fig. 28. As T_o is increased, the location at which the solid first bifurcates moves lower in the domain, resulting in more space between the two main branches. The gap in the solid at the top of the domain is also widened as T_o is increased. These changes in the solid shape reduce shielding and increase radiation heat transfer.

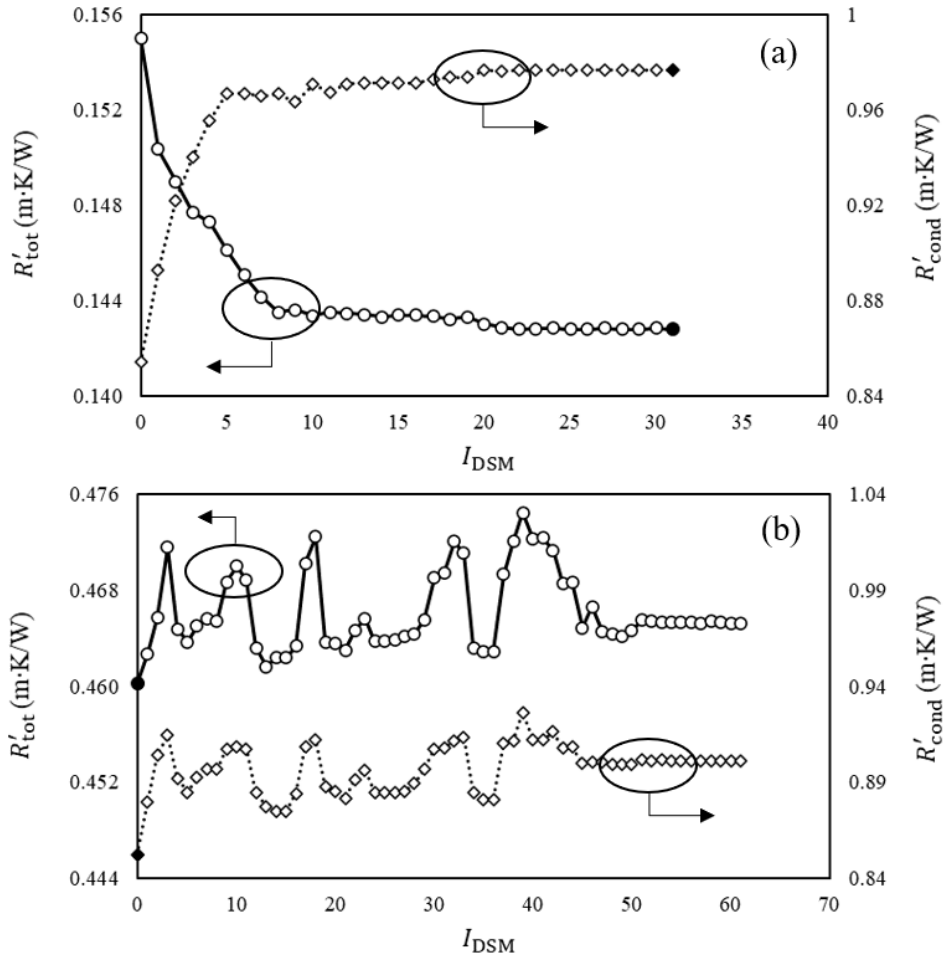

Fig. 27 Evolution history of the total and pure conduction thermal resistances associated with the discrete solid for (a) T_o = 1000 K and (b) T_o = 500 K [**P4**].

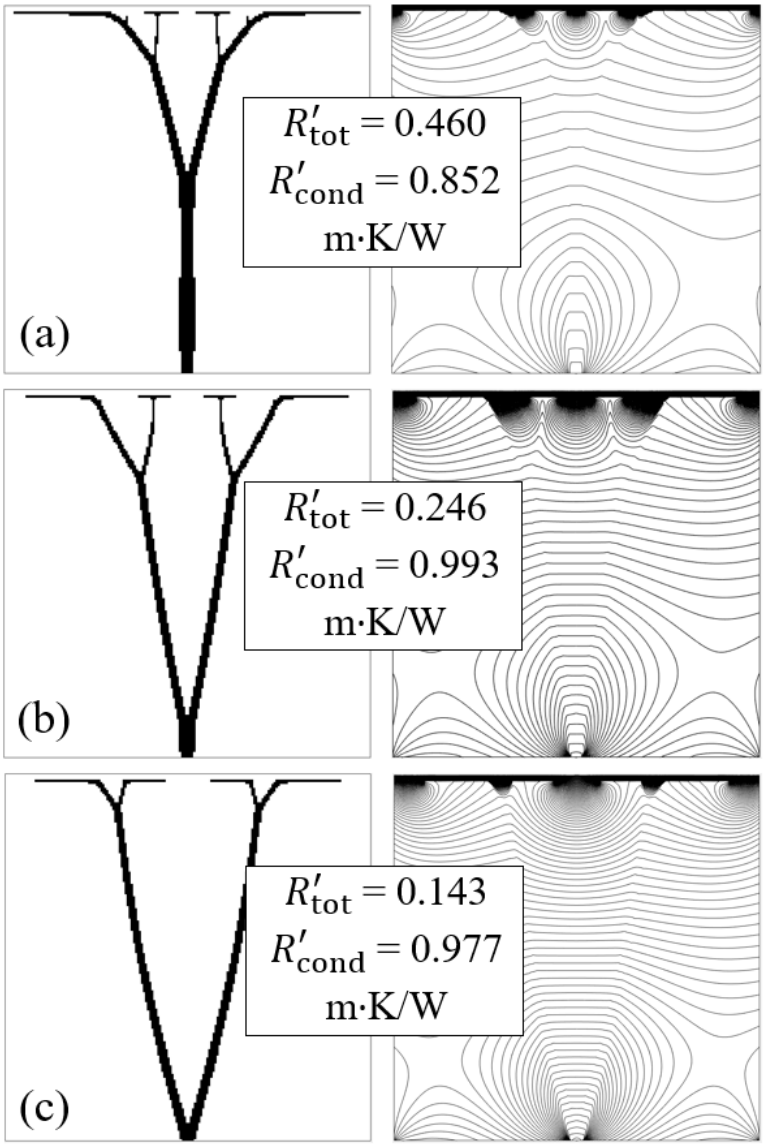

Fig. 28 Discrete solid shapes and temperature distributions associated with $R'_{\text{tot,min}}$ for (a) $T_o = 500$ K (I_{DSM} = 0), (b) $T_o = 750$ K (I_{DSM} = 54), and (c) $T_o = 1000$ K (I_{DSM} = 31) [**P4**].

The evolution histories of the total and conduction thermal resistances associated with the discrete solid distribution for the k_s^* = 0.01 and 0.1 cases are shown in Fig. 29. The case with the weaker strength of conduction (k_s^* = 0.01), and therefore stronger relative strength of radiation, exhibits a monotonic decrease in overall thermal resistance and converges to the optimal solution (Fig. 29a). The k_s^* = 0.1 case, however, has a sharp initial decrease in overall thermal resistance coinciding with a sharp increase in the conduction thermal resistance. The resistance values are roughly constant for the remainder of the DSM process (Fig. 29b).

Both the initial (I_{DSM} = 0) and the optimal (I_{DSM} > 0) discrete solid shapes and temperature distributions associated with the various k_s^* cases are reported in Fig. 30. Again, the discrete solid shapes associated with I_{DSM} = 0 (left column of Fig. 13) are obtained from the pure conduction TO. As evident in the second and third rows of the first column of Fig. 30, the optimal discrete solid shapes that were generated from the continuous model with ε = 0 are similar for k_s^* = 0.1 and 1. For the k_s^* = 0.01 case, however, there is a higher concentration of solid near the vertical centerline and less branching. The optimal geometries associated with ε = 1 (third column of Fig. 30) are substantially different than those associated with ε = 0. This is especially evident for the weak conduction (strong radiation) case, $k_s^* = 0.01$, where parts of the solid propagate laterally outward, forming two horizontal, petal-like structures that do little to reduce the conduction resistance but serve as radiatively active surfaces that improve radiative exchange with the cold, upper surface. Another feature that is unique to the $k_s^* = 0.01$, ε = 0.4 case is that all the solid material resides in the lower half of the domain, which prevents shielding of radiation transfer.

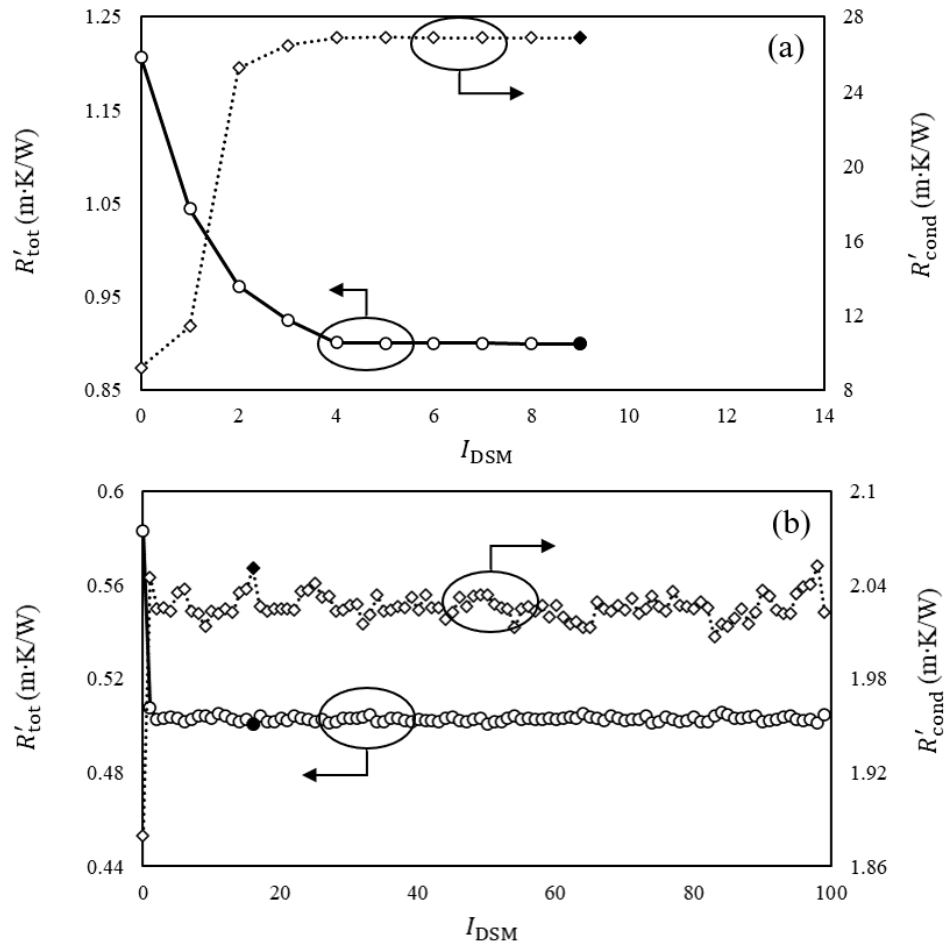

Fig. 29 Evolution history of the total and pure conduction thermal resistances associated with the discrete solid for (a) $k_s^* = 0.01$ and (b) $k_s^* = 0.1$ with $T_o = 750$ K [**P4**].

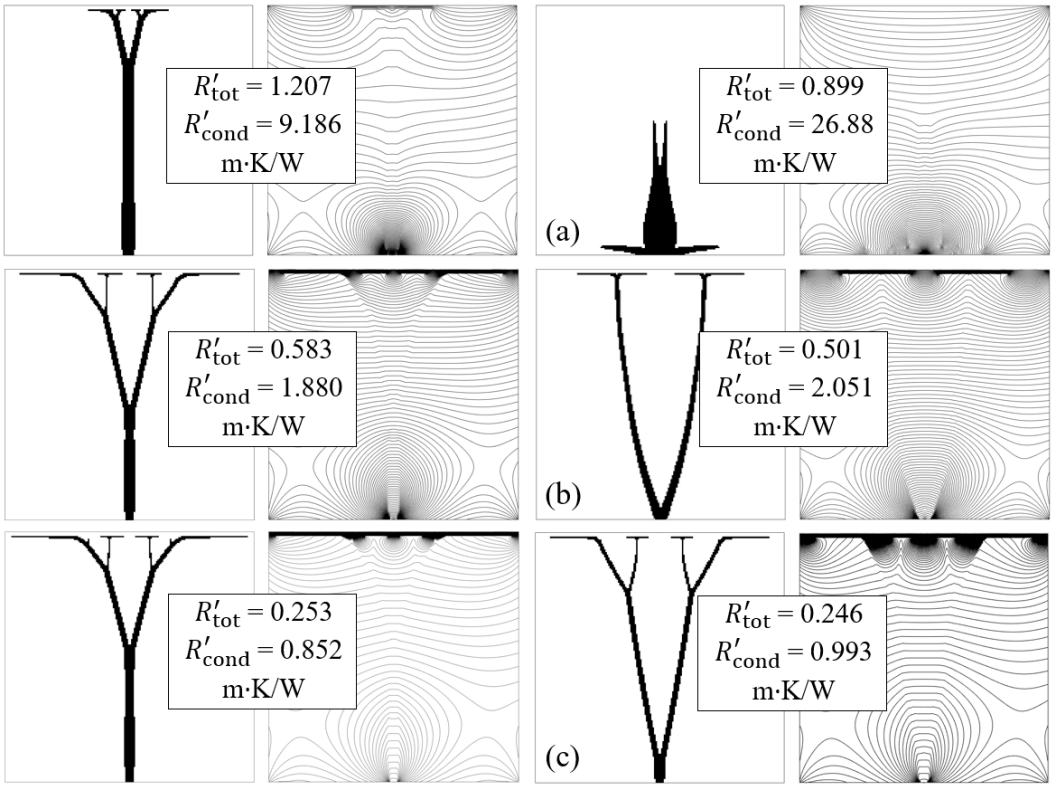

Fig. 30 Discrete solid shapes and temperature distributions associated with T_o = 750 K and k_s^* = 0.01 (top), k_s^* = 0.1 (middle), and k_s^* = 1 (bottom). I_{DSM} = 0 for the first and second columns. The third and fourth columns are associated with $R'_{tot,min}$ and (a) I_{DSM} = 9, (b) I_{DSM} = 16, and (c) I_{DSM} = 54 [**P4**].

Discussion 6

6.1 Comparison of Methods

Three design methods (EDM, SGM, and DSM) that incorporate the effects of radiation have been developed and shown to have merit. The EDM and SGM are both heuristic methods that are not founded on rigorous optimization methodologies but rather on rules based on intuition. Although they are heuristic and their implementation is relatively simple and straightforward, it was shown that these design methods resulted in favorable geometries with reduced overall thermal resistances. The DSM utilizes a formal TO method that is based on rigorous optimization theory and is fueled by sensitivity information. Like the EDM and SGM, the DSM was shown to reduce the overall thermal resistance in most physical cases considered.

In order to make a direct comparison between a heuristic method and a formal optimization method, the DSM is now applied to the physical conditions of Paper **P3** and compared to the SGM. Note that the initial solid shape of the DSM ($I_{\mathrm{DSM}} = 0$) is already included in Paper **P3** as the TO comparison. The solid shapes generated by the (*i*) SGM with $\varepsilon = 0$, (*ii*) SGM with $\varepsilon = 0.4$, (*iii*) TO with $\varepsilon = 0$, and (*iv*) DSM with $\varepsilon = 0.4$ are shown in Fig. 31 for the $k_s^* = 1$ case. The iteration (I_{DSM}) at which the DSM achieves the minimum thermal resistance is also reported in Fig. 31. The corresponding temperature distributions are shown in Fig. 32. The thermal resistance values and figures of merit are reported in Table 5. Note that Figs. 31 and 32 and Table 5 are extensions of the figures from Paper **P3**.

In comparing the DSM (Figs. 31m - 31p) and TO (Figs. 31i – 31l), there are subtle changes in the solid configurations as a result of incorporating radiation. The point at which the solid initially bifurcates has moved lower in the domain, as was observed in Paper **P4**. There is also a slight decrease in overall thermal resistance between TO and DSM as reported in Table 5. The DSM (Figs. 31m - 31p) results in solid configurations with more complexity than the SGM (Figs. 31e - 31h). Also, the lowest overall thermal resistance for every A_s value of the $k_s^* = 1$ cases is achieved by the DSM (Table 5). It was already shown in Paper **P3** that the TO method resulted in favorable thermal performance for most A_s values, so this result is not surprising.

The solid configurations and corresponding temperature distributions associated with $k_s^* = 0.1$ are shown in Figs. 33 and 34, respectively. The thermal resistances and figures of merit are reported in Table 6. With the lower solid thermal conductivity, the relative strength of conduction is lower, thus radiation is relatively stronger. As a result, there is a more significant difference between the solid shapes of the DSM (Figs. 33m - 33p) and TO (Figs. 33i - 33l). Correspondingly, there is a more dramatic decrease in R'_{tot} and

increase in R'_{cond} between TO and DSM (Table 6). However, even though the DSM has better thermal performance than the TO method, the heuristic SGM (Figs. 33e - 33h) achieves the lowest overall thermal resistance for every A_s value of the k_s^* = 0.1 cases. This somewhat unexpected result is attributable to the high concentration of vertical columns extending from the bottom center of the domain in Figs. 33e - 33h. This feature results in a large surface area of solid that participates in radiation exchange with the top, colder isothermal boundary. A sensitivity filter (Appendix B of Paper **P4**) is employed in TO and the DSM to prevent unrealistic checkerboard patterns from emerging. As a result, the high concentration of alternating solid and fluid control volumes present in Figs. 33e - 33h cannot be achieved by TO or the DSM.

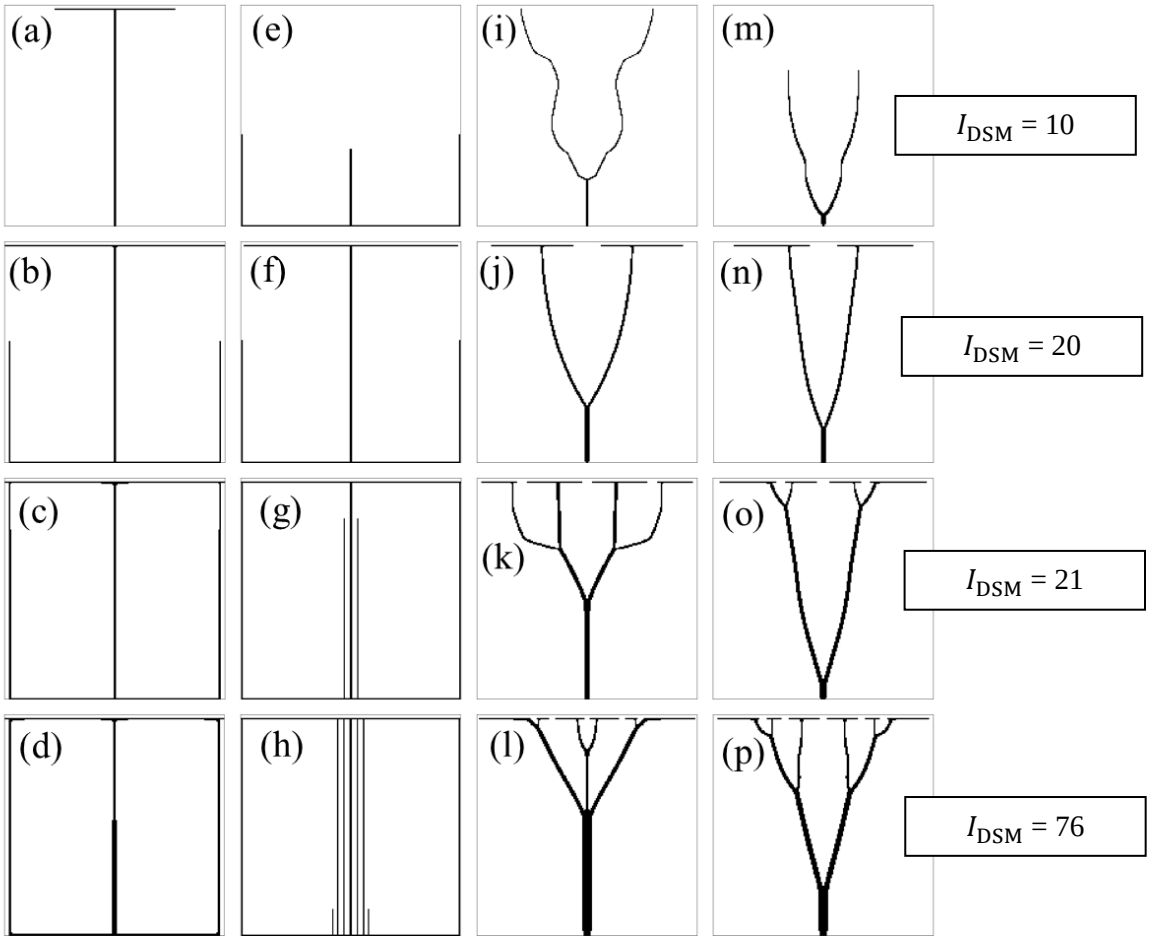

Fig 31 Solid configurations for k_s^* = 1 and the SGM with ε = 0 (left), the SGM with ε = 0.4 (second column), TO (third column), and DSM (right) for $A_s \times 10^3$ = 0.05 m^2 (a, e, i, m), 0.1 m^2 (b, f, j, n), 0.15 m^2 (c, g, k, o), and 0.2 m^2 (d, h, l, p). The I_{DSM} corresponding to the minimum thermal resistance (m-p) are also reported.

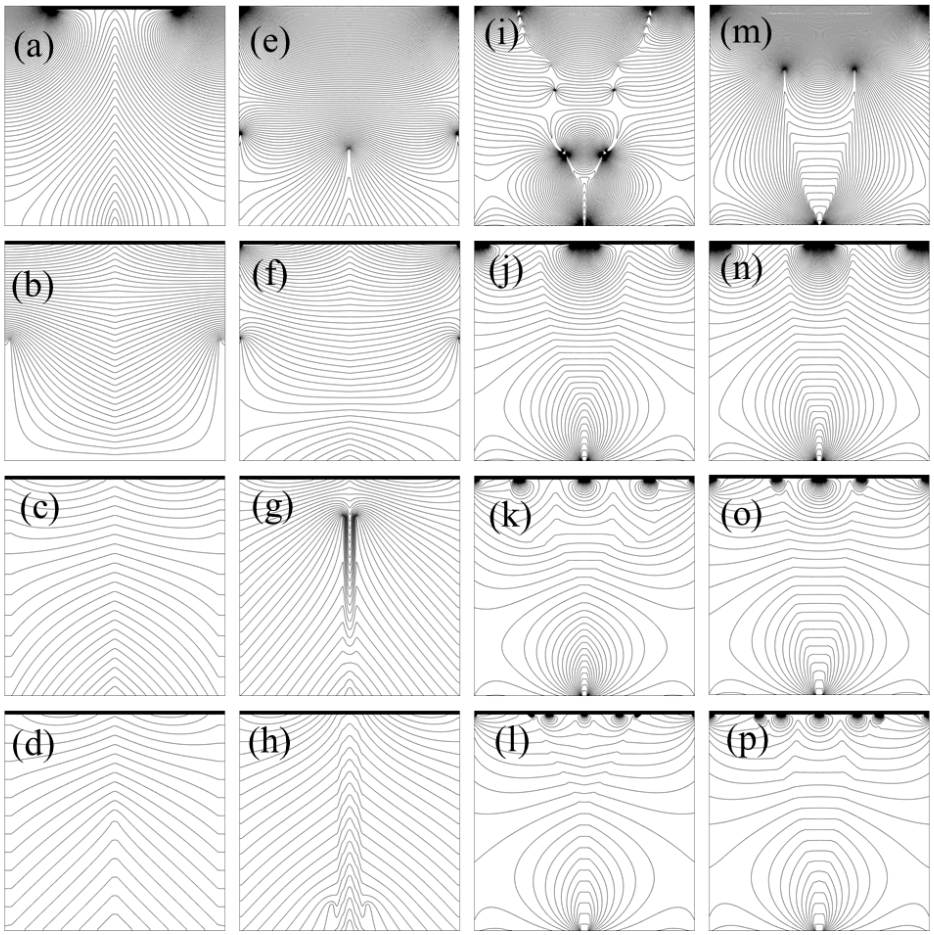

Fig 32 Temperature distributions for $k_s^* = 1$ and the SGM with $\varepsilon = 0$ (left), the SGM with $\varepsilon = 0.4$ (second column), TO (third column), and DSM (right) for $A_s \times 10^3 = 0.05$ m^2 (a, e, i, m), 0.1 m^2 (b, f, j, n), 0.15 m^2 (c, g, k, o), and 0.2 m^2 (d, h, l, p).

Table 5 Thermal resistances and figure of merit for $k_s^* = 1$.

$A_s \times 10^3$ (m^2)	Method	$R'_{\mathrm{tot}}(\frac{\mathrm{m \cdot K}}{\mathrm{W}})$	$R'_{\mathrm{cond}}(\frac{\mathrm{m \cdot K}}{\mathrm{W}})$	F
0.05	SGM, $\varepsilon = 0$	1.468	1.468	1909
	SGM, $\varepsilon = 0.4$	0.6307	27.72	4442
	TO, $\varepsilon = 0.4$	0.9816	21.12	2854
	DSM, $\varepsilon = 0.4$	0.6286	16.20	4457
0.1	SGM, $\varepsilon = 0$	1.071	1.071	1308
	SGM, $\varepsilon = 0.4$	0.6144	1.080	2280
	TO, $\varepsilon = 0.4$	0.5341	1.015	2623
	DSM, $\varepsilon = 0.4$	0.5235	1.051	2676
0.15	SGM, $\varepsilon = 0$	0.8514	0.8514	1097
	SGM, $\varepsilon = 0.4$	0.5286	0.8706	1767
	TO, $\varepsilon = 0.4$	0.4946	0.8591	1888
	DSM, $\varepsilon = 0.4$	0.4750	0.8545	1966
0.2	SGM, $\varepsilon = 0$	0.7935	0.7935	882.7
	SGM, $\varepsilon = 0.4$	0.4777	0.7783	1466
	TO, $\varepsilon = 0.4$	0.4506	0.7821	1554
	DSM, $\varepsilon = 0.4$	0.4434	0.8034	1579

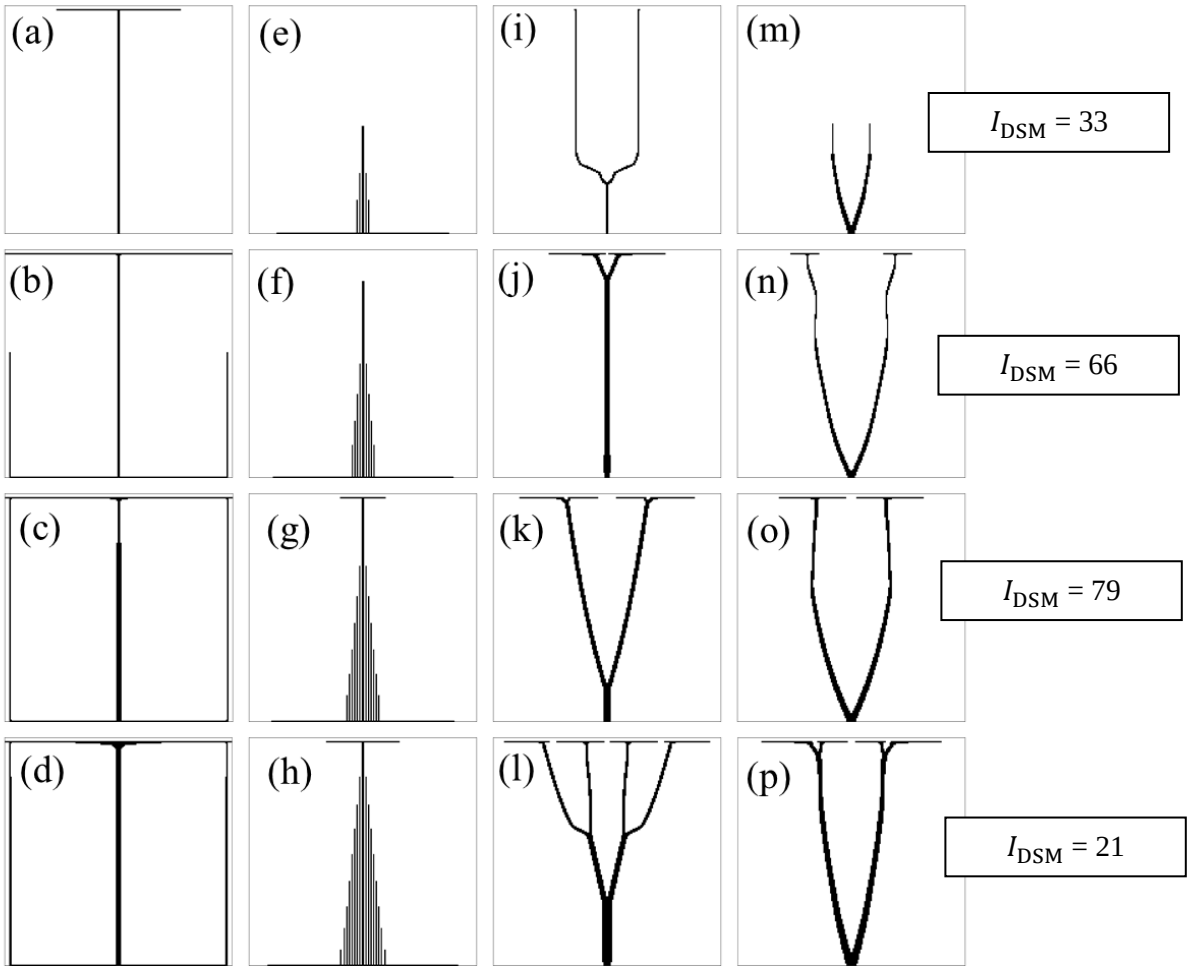

Fig 33 Solid configurations for k_s^* = 0.1 and the SGM with ε = 0 (left), the SGM with ε = 0.4 (second column), TO (third column), and DSM (right) for $A_s \times 10^3$ = 0.05 m^2 (a, e, i, m), 0.1 m^2 (b, f, j, n), 0.15 m^2 (c, g, k, o), and 0.2 m^2 (d, h, l, p). The I_{DSM} corresponding to the minimum thermal resistances (m-p) are also reported.

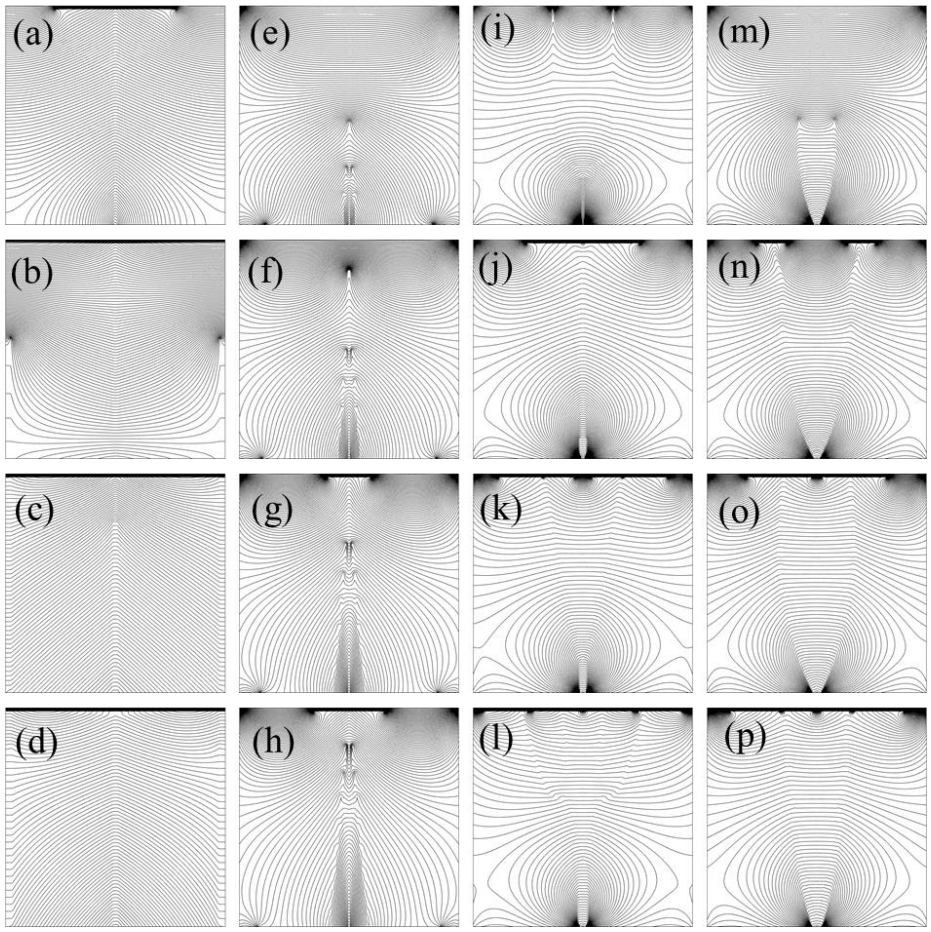

Fig 34 Temperature distributions for k_s^* = 0.1 and the SGM with ε = 0 (left), the SGM with ε = 0.4 (second column), TO (third column), and DSM (right) for $A_s \times 10^3$ = 0.05 m^2 (a, e, i, m), 0.1 m^2 (b, f, j, n), 0.15 m^2 (c, g, k, o), and 0.2 m^2 (d, h, l, p).

Table 6 Thermal resistances and figure of merit for $k_s^* = 0.1$.

$A_s \times 10^3$ (m^2)	Method	$R'_{\mathrm{tot}}(\frac{\mathrm{m \cdot K}}{\mathrm{W}})$	$R'_{\mathrm{cond}}(\frac{\mathrm{m \cdot K}}{\mathrm{W}})$	F
0.05	SGM, $\varepsilon = 0$	4.742	4.742	590.9
	SGM, $\varepsilon = 0.4$	0.8540	28.78	3281
	TO, $\varepsilon = 0.4$	1.274	6.966	2199
	DSM, $\varepsilon = 0.4$	0.9001	26.58	3112
0.1	SGM, $\varepsilon = 0$	4.261	4.261	328.7
	SGM, $\varepsilon = 0.4$	0.8134	14.44	1730
	TO, $\varepsilon = 0.4$	1.029	2.926	1362
	DSM, $\varepsilon = 0.4$	0.8914	3.728	1571
0.15	SGM, $\varepsilon = 0$	2.317	2.317	403.1
	SGM, $\varepsilon = 0.4$	0.8063	4.385	1158
	TO, $\varepsilon = 0.4$	0.9504	2.135	982.6
	DSM, $\varepsilon = 0.4$	0.8592	2.295	1087
0.2	SGM, $\varepsilon = 0$	1.946	1.946	360
	SGM, $\varepsilon = 0.4$	0.8101	3.448	864.6
	TO, $\varepsilon = 0.4$	0.9226	1.696	759.2
	DSM, $\varepsilon = 0.4$	0.8302	1.760	843.7

6.2 Conclusions and Recommendations

An overview of the four publications which constitute this dissertation has been provided, and a brief comparison of the heuristic and formal design methods has been discussed. The main contributions of this body of work are summarized as follows:

- A novel evolutionary design method (EDM) has been developed in Paper **P1** and shown to have some merit by reducing the overall thermal resistance. While better thermal performance is achieved by a topology optimization (TO) method, the EDM has the advantage of being relatively simple and straightforward, which allows for the effects of radiation to be easily incorporated.
- To the author's knowledge, Paper **P2** is the first study to apply a design method that does not require geometric features to be specified *a priori* to a conducting solid cooled by conjugate free convection and surface-to-surface radiation. The study demonstrates the influence that thermal radiation has on (*i*) the physics of the problem (fluid flow and temperature distribution) and (*ii*) the predicted optimal geometry. It was found that, in general, increasing

the strength of radiation results in increased symmetry about the vertical centerline for both the physics and predicted solid geometries.

- Paper **P3** introduces a novel solid growth method (SGM), which is distinct from the EDM in that the solid mass is not constant throughout the design process. It was demonstrated that the relative strength of radiation had a significant effect on the solid growth and thermal performance. The SGM was also compared to a formal TO method that neglects the effects of radiation. It was found that when a low amount of solid material or a relatively low solid thermal conductivity is considered, the SGM produces favorable solid configurations with lower overall thermal resistances.
- In Paper **P4**, the effects of thermal radiation were incorporated into a formal TO method, by introducing a novel dual solid method (DSM) that utilizes both a continuous and discrete description of the solid distribution. To the author's knowledge, the DSM is the first TO method to iterate between two distinct solid descriptions and Paper **P4** represents the first study to apply a formal TO method to a strongly coupled radiation-conduction problem. Once again, it was shown that radiation has a significant effect on the predicted optimal geometry and thermal performance.
- The results of Papers **P2**, **P3**, and **P4** demonstrate that thermal radiation can have a significant effect on optimal geometries and should, therefore, be considered in thermal design methods. This is particularly true for physical situations with dominant radiation heat transfer, such as (*i*) high temperatures and emissivities, (*ii*) low amounts of solid material, (*iii*) low solid thermal conductivity, and (*iv*) low or negligible advective effects.
- Lastly, a comparison of heuristic (SGM) and formal (DSM) design methods was made. Somewhat surprisingly, the SGM resulted in better thermal performance when a low solid thermal conductivity was considered. This is attributed to the high concentration of vertical columns that is unattainable by the DSM due to its filtering routine.

Based on the results of this dissertation, several recommendations for future research are as follows:

- The DSM was applied to a coupled radiation-conduction problem. It would be beneficial, however, to incorporate the effects of free convection. This could be achieved by using the discrete numerical model of Paper **P2** in conjunction with the continuous TO methods developed in the literature for free convection problems (Alexandersen *et al*. 2014).
- Throughout this dissertation, the radiative surfaces are assumed to be diffuse and gray, however, many solids are characterized by both directional and spectral radiative properties. Incorporating these effects could lead to significantly different optimal geometries.

- It was also assumed that the fluid is radiatively transparent. The design methods could be adapted for situations involving semi-transparent media. This would require a more advanced radiation model.
- Lastly, due to their complexity, the optimal solid geometries obtained in this dissertation might require additive manufacturing methods to be fabricated. Therefore, it would be beneficial to incorporate manufacturing constraints and effective thermophysical properties associated with additive processes into the design methods.

References 7

Ahmed, H.E., Salman, B.H., Kherbeet, A.S., and Ahmed, M.I., 2018, "Optimization of Thermal Design of Heat Sinks: a Review," *Int. J. Heat Mass Transfer*, **118**, pp. 129-153. https://doi.org/10.1016/j.ijheatmasstransfer.2017.10.099

Alexandersen, J., Aage, N., Andreasen, C.S., and Sigmund, O., 2014, "Topology Optimisation for Natural Convection Problems," *Int. J. Numer. Methods Fluids*, **76**(10), pp. 699-721. https://doi.org/10.1002/fld.3954

Alexandersen, J., Sigmund, O., and Aage, N., 2016, "Large Scale Three-Dimensional Topology Optimisation of Heat Sinks Cooled by Natural Convection," *Int. J. Heat Mass Transfer*, **100**, pp. 876-891. https://doi.org/10.1016/j.ijheatmasstransfer.2016.05.013

Alexandersen, J., Sigmund, O., Meyer, K.E., and Lazarov, B.S., 2018, "Design of Passive Coolers for Light-Emitting Diode Lamps Using Topology Optimisation," *Int. J. Heat Mass Transfer*, **122**, pp. 138-149. https://doi.org/10.1016/j.ijheatmasstransfer.2018.01.103

Almogbel, M., and Bejan, A., 2001, "Constructal Optimization of Nonuniformly Distributed Tree-Shaped Flow Structures for Conduction," *Int. J. Heat Mass Transfer*, **44**(22), pp. 4185-4194. https://doi.org/10.1016/S0017-9310(01)00080-1

Audunson, T., and Gebhart, B., 1972, "An Experimental and Analytical Study of Natural Convection with Appreciable Thermal Radiation Effects," *J. Fluid Mechanics*, **52**(1), pp. 57-95. https://doi.org/10.1017/S0022112072002976

Bar-Cohen, A., 1979, "Fin Thickness for an Optimized Natural Convection Array of Rectangular Fins," *ASME J. Heat Transfer*, **101**(3), pp. 564-566. https://doi.org/10.1115/1.3451032

Bar-Cohen, A., Iyengar, M., and Kraus, A.D., 2003, "Design of Optimum Plate-Fin Natural Convective Heat Sinks," *ASME J. Electron Packag*, **125**(2), pp. 208-216. https://doi.org/10.1115/1.1568361

Bejan, A., 1997, "Constructal-Theory Network of Conducting Paths for Cooling a Heat Generating Volume," *Int. J. Heat Mass Transfer*, **40**(4), pp. 799-816. https://doi.org/10.1016/0017-9310(96)00175-5

Bendsøe, M.P., and Sigmund, O., 2003, *Topology Optimization: Theory, Methods, and Applications*. Springer, Berlin. https://doi.org/10.1007/978-3-662-05086-6

Bergman, T.L., and Lavine, A.S., 2017, *Fundamentals of Heat and Mass Transfer*, 8th edition, John Wiley and Sons, New Jersey.

Bruns, T.E., 2007, "Topology Optimization of Convection-Dominated, Steady-State Heat Transfer Problems," *Int. J. Heat Mass Transfer*, **50**(15-16), pp. 2859-2873. https://doi.org/10.1016/j.ijheatmasstransfer.2007.01.039

Carpenter, J.R., Briggs, D.G., and Sernas, V., 1976, "Combined Radiation and Developing Laminar Free Convection Between Vertical Flat Plates with Asymmetric Heating," *ASME J. Heat Transfer*, **98**(1), pp. 95-100. https://doi.org/10.1115/1.3450476

Castro, D.A., Kiyono, C.Y., and Silva, E.C.N., 2015, "Design of Radiative Enclosures by Using Topology Optimization," *Int. J. Heat Mass Transfer*, **88**, pp. 880-890. https://doi.org/10.1016/j.ijheatmasstransfer.2015.04.077

Chu, W.X., Lin, Y.C., Chen, C.Y., and Wang, C.C., 2019, "Experimental and Numerical Study on the Performance of Passive Heat Sink Having Alternating Layout," *Int. J. Heat Mass Transfer,* **135**, pp. 822-836. https://doi.org/10.1016/j.ijheatmasstransfer.2019.02.034

Coffin, P., and Maute, K., 2016, "A Level-Set Method for Steady-State and Transient Natural Convection Problems," *Structural and Multidisciplinary Optimization,* **53**(5), pp. 1047-1067. https://doi.org/10.1007/s00158-015-1377-y

Gao, T., Zhang, W.H., Zhu, J.H., Xu, Y.J., and Bassir, D.H., 2008, "Topology Optimization of Heat Conduction Problem Involving Design-Dependent Heat Load Effect," *Finite Elem. Anal. Des.*, **44**(14), pp. 805-813. https://doi.org/10.1016/j.finel.2008.06.001

Gersborg-Hansen, A., Bendsøe, M.P., and Sigmund, O., 2006, "Topology Optimization of Heat Conduction Problems Using the Finite Volume Method," *Struct. Multidiscip. Optim.*, **31**(4), pp. 251-259. https://doi.org/10.1007/s00158-005-0584-3

Hall, D.A., Vliet, G.C., and Bergman, T.L., 1999, "Natural Convection Cooling of Vertical Rectangular Channels in Air Considering Radiation and Wall Conduction," *ASME J. Electron Packag.*, **121**(2), pp. 75-84. https://doi.org/10.1115/1.2792671

Hottel, H. C., 1954, "Radiant Heat Transmission" *Heat Transmission*, W.H. McAdams, ed., McGraw-Hill, New York.

Iga, A., Nishiwaki, S., Izui, K., and Yoshimura, M., 2009, "Topology Optimization for Thermal Conductors Considering Design-Dependent Effects, Including Heat Conduction and Convection," *Int. J. Heat Mass Transfer,* **52**(11), pp. 2721-2732. https://doi.org/10.1016/j.ijheatmasstransfer.2008.12.013

Lazarov, B.S., Sigmund, O., Meyer, K.E., and Alexandersen, J., 2018, "Experimental Validation of Additively Manufactured Optimized Shapes for Passive Cooling," *Applied Energy*, **226**, pp. 330-339. https://doi.org/10.1016/j.apenergy.2018.05.106

Li, Q., Steven, G.P., Querin, O.M., and Xie, Y.M., 1999, "Shape and Topology Design for Heat Conduction by Evolutionary Structural Optimization," *Int. J. Heat Mass Transfer*, **42**(17), pp. 3361-3371. https://doi.org/10.1016/S0017-9310(99)00008-3

Li, Q., Steven, G.P., Xie, Y.M., and Querin, O.M., 2004, "Evolutionary Topology Optimization for Temperature Reduction of Heat Conducting Fields," *Int. J. Heat Mass Transfer,* **47**(23), pp. 5071-5083. https://doi.org/10.1016/j.ijheatmasstransfer.2004.06.010

Marck, G., Nemer, M., and Harion, J.L., 2013, "Topology Optimization of Heat and Mass Transfer Problems: Laminar Flow," *Numer. Heat Transfer B*, **63**(6), pp. 508-539. https://doi.org/10.1080/10407790.2013.772001

Marck, G., Nemer, M., Harion, J.L., Russeil, S., and Bougeard, D., 2012, "Topology Optimization Using the SIMP Method for Multiobjective Problems," *Numer. Heat Transfer B*, **61**(6), pp. 439-470. https://doi.org/10.1080/10407790.2012.687979

Muzychka, Y.S., 2007, "Constructal Multi-scale Design of Compact Micro-tube Heat Sinks and Heat Exchangers," *Int. J. Thermal Sciences*, **46**(3), pp. 245-252. https://doi.org/10.1016/j.ijthermalsci.2006.05.002

Patankar, S.V., 1980, *Numerical Heat Transfer and Fluid Flow*, McGraw-Hill, New York.

Sigmund, O., and Maute, K., 2013, "Topology Optimization Approaches," *Struct. Multidiscip. Optim.*, **48**, pp. 1031-1055. https://doi.org/10.1007/s00158-013-0978-6

Svanberg, K., 1987, "The Method of Moving Asymptotes – a New Method for Structural Optimization," *Int. J. Numerical Methods in Engineering*, **24**(2), pp. 359-373. https://doi.org/10.1002/nme.1620240207

Wang, C., Yu, Z., Zhou, M., and Qian, X., 2022, "Topology Optimization of Thermophotonic Problem for Daytime Passive Radiative Cooling," *Int. J. Heat Mass Transfer*, **183**, pp. 122097. https://doi.org/10.1016/j.ijheatmasstransfer.2021.122097

Yan, S.N., Wang, F.W., Hong, J., and Sigmund, O., 2019, "Topology Optimization of Microchannel Heat Sinks Using a Two-Layer Model," *Int. J. Heat Mass Transfer*, **143**, p. 118462. https://doi.org/10.1016/j.ijheatmasstransfer.2019.118462

Yoon, G.H., 2010, "Topological Design of Heat Dissipating Structure with Forced Convective Heat Transfer," *J. Mech. Sci. Technol.*, **24**(6), pp. 1225-1233. https://doi.org/10.1007/s12206-010-0328-1

Zhang, B., Zhu, J., Xiang, G., and Gao, L., 2021, "Design of Nanofluid-Cooled Heat Sink Using Topology Optimization," *Chinese Journal of Aeronautics*, **34**(2), pp. 301-317. https://doi.org/10.1016/j.cja.2020.05.023

Zhang, Y., and Liu, S., 2008, "Design of Conducting Paths Based on Topology Optimization," *Heat Mass Transfer*, **44**, pp. 1217-1227. https://doi.org/10.1007/s00231-007-0365-1

Zhao, X., Yin, Y., He, Z., and Liu, X., 2021, "Inverse Design of Indoor Radiant Terminal Using the Particle Swarm Optimization Method with Topology Concept." *Building and Environment*, **204**, p. 108117. https://doi.org/10.1016/j.buildenv.2021.108117

Publications 8

Paper P1

Title:

An Iterative Design Method to Reduce the Overall Thermal Resistance in a Conjugate Conduction-Free Convection Configuration

Authors:

Chadwick D. Sevart

Theodore L. Bergman

Journal:

Frontiers in Heat and Mass Transfer

Frontiers in Heat and Mass Transfer

AN ITERATIVE DESIGN METHOD TO REDUCE THE OVERALL THERMAL RESISTANCE IN A CONJUGATE CONDUCTION-FREE CONVECTION CONFIGURATION

Chadwick D. Sevart*, Theodore L. Bergman

University of Kansas, Lawrence, Kansas, 66044, USA

ABSTRACT

A design approach is proposed and demonstrated to identify desirable two-dimensional solid geometries, cooled by natural convection, that offer superior thermal performance in terms of reduced overall (conduction-convection) thermal resistance. The approach utilizes (*i*) heat transfer modeling in conjunction with (*ii*) various novel shape evolution rules. Predictions demonstrate the evolution of the solid shape and associated reduction of the overall thermal resistance. Parametric simulations reveal the dependence of the predicted solid shape on the evolution rule employed, the thermal conductivity of the solid material, and the strength of advection within the fluid.

Keywords: *Topology Optimization, Heat Sinks, Natural Convection*

1. INTRODUCTION

The design of various thermal systems has long been a point of research with a common goal being to reduce the overall conduction-convection thermal resistance while minimizing the weight or volume of the solid. Relative to heat sink design, early on this was achieved using size and geometrical optimization of heat sinks that were comprised of geometrically well-defined sub-components (e.g. straight, circular, or pin fins of various cross sectional shapes). For example, Bar-Cohen (1979) developed expressions for optimum fin thicknesses, spacing between fins, and fin widths, that maximize the heat dissipation per unit fin cross sectional area. The correlations were developed based on the assumption of a uniform heat transfer coefficient and fin efficiency. In a later study by Bar-Cohen *et al.* (2003), the work was extended to incorporate experimentally validated correlations for the heat transfer coefficient (Nusselt number), including for non-isothermal plates. In a similar study, Kim (2012) optimized the size and shape of plate fin heat sinks that had a trapezoidal cross-section and found better thermal performance when compared to a similar optimized plate fin heat sink of uniform thickness.

While size and shape optimization provided good designs of traditional heat sink layouts comprised of, for example, plate fin or pin fin arrays, a truly optimal heat sink shape that achieves the best thermal performance is often complex and might consist of unanticipated geometrical features. To this end, topology optimization (TO) is an evolving design methodology which provides the best solid shapes that will achieve a specified goal while satisfying imposed constraints (Bendsøe and Sigmund, 2003).

The general TO process involves: (*i*) discretization of a computational domain consisting of a solid and perhaps an adjoining fluid, (*ii*) specification of an initial spatial distribution of solid material, (*iii*) solution of the appropriate equations that describe the physical process or processes of interest, and (*iv*) optimization of the solid material shape and configuration using an appropriate algorithm. Steps (*iii*) and (*iv*) are repeated until the final solid shape is achieved. A comprehensive review of the different variations of TO and their characteristics can be found in Sigmund and Maute (2013).

TO was first introduced by Bendsøe and Kichuchi (1988) and used as a method to most effectively distribute stresses in a structural member of unknown shape but has since been adapted to the fields of heat transfer and fluid flow.

* *Corresponding author. Email: cdsevart@ku.edu*

To this end, Li *et al.* (1999) applied TO to heat conduction problems; they used the principles of evolutionary structural optimization (ESO) to design solids that resulted in the most uniform distribution of a surface heat flux. Other works that apply TO to heat conduction problems include Gersborg-Hansen *et al.* (2006), Gao *et al.* (2008), Marck *et al.* (2012), Dirker and Meyer (2013) and Xia *et al.* (2018). Subsequently, several studies included convection heat transfer occurring at the boundary of solid structures into TO problems by use of a constant convection coefficient and Newton's law of cooling (Yin and Ananthasuresh, 2002; Bruns, 2007; Ahn and Cho, 2010).

To the authors' knowledge, the first investigators to apply TO to fluid flow configurations were Borrvall and Petersson (2003) who sought to minimize the pressure drop experienced by the fluid in low Reynolds number flows. A study by Yoon (2010) involved the application of TO to forced convection problems accounting for non-uniform convective conditions that were determined by solution of an advection-diffusion model. Similar studies which incorporate the effects of fluid flow by solving the advection-diffusion equations include Koga *et al.* (2013), Haertel and Nellis (2017), Qian and Dede (2016), and Subramaniam *et al.* (2019). Topology optimization for natural convection problems has been recently studied by Alexandersen *et al.* (2014) where the authors used density-based TO to design complex 2D heat sinks as well as micropumps driven by natural convection. In a later work, the same method was used to design a 3D heat sink for light emitting diodes (Alexandersen *et al.*,2018). In a similar study by Coffin and Maute (2016), a level-set TO method was introduced to determine optimal solid shapes experiencing steady-state and transient natural convection. Joo *et al.* (2017) used a simplified surrogate model for natural convection which incorporated a shape-dependent convection coefficient in order to design a 3D natural convection heat sink using density based TO.

Although TO is a powerful design methodology, it can be computationally expensive, especially when considering a complex physical problem such as conjugate heat transfer with conduction in the solid region and natural convection in the fluid. The objective of this work is to propose and demonstrate an overall *evolutionary design method* (*EDM*) for 2D solids cooled by natural convection. The EDM consists of a *heat transfer* (*HT*) *sub-model* and one of four proposed *shape evolution method* (*SEM*) *sub-models*. The proposed EDM is comparable to bidirectional evolutionary structural optimization (BESO), in which a solid structure evolves by the simultaneous removal of unnecessary material that is less stressed and addition of material to regions that are more stressed. Through this process the structure gradually approaches the maximum overall stiffness per unit material volume. The difference between BESO and the design method of this work is that the solid is reconfigured based on local temperatures or heat fluxes. Similar evolutionary design methods have been applied to heat conduction problems, such as (Li *et al.* 1999 and 2004). The proposed design method is relatively simple compared to many TO methods because (*i*) the shape evolution does not require a formal optimization analysis and (*ii*) the governing equations are solved using a finite volume method, making the solid redistribution straightforward. The predictions of the proposed EDM will be compared to an optimized heat sink design (Coffin and Maute, 2016) operating under identical conditions. A parametric study will also be conducted to observe the influence of solid thermal conductivity and the domain size (Rayleigh number) on the final solid shape.

2. PHYSICAL AND NUMERICAL MODELS

The situation of interest is depicted in Fig. 1. A two-dimensional, square domain is composed of a fixed amount of solid and an adjacent fluid. As shown, the solid is arbitrarily specified to have an initial, semi-circular cross-section of radius R and cross-sectional area $A_t = \pi R^2/2$. A heat rate per unit length, q', is applied at the bottom center of the domain, while the top boundary is isothermal at a reference temperature T_o. All remaining boundaries are adiabatic. The temperature of the solid at the location where q' is applied is to be minimized by allowing the solid shape to evolve under the constraint that the total amount of solid remains constant, affecting both conduction in the solid and free convection in the fluid. The conduction and convection processes are coupled at the solid-fluid interface.

The overall EDM simulation is initiated with the domain shown in Fig. 1. After the steady-state temperature distributions (including the maximum solid temperature at $x = H/2$, $y = 0$) are calculated with the HT sub-model (Section 2.1) the solid cross-sectional shape is modified according to a SEM (Section 2.2), the conjugate conduction-convection problem is re-solved, and the maximum solid temperature is re-calculated. The *heat transfer prediction – shape evolution – heat transfer prediction* process is continually repeated with the goal to reduce the solid temperature at the location where q' is applied.

2.1 Heat Transfer Sub-Model

Heat transfer within the fluid is described by (*i*) the conservation of mass equation, (*ii*) the Navier-Stokes equations and (*iii*) the conservation of energy equation. A Boussinesq, Newtonian fluid is considered, and viscous dissipation is neglected. The fluid flow and heat transfer processes are steady-state, and it is assumed that all thermophysical properties are constant. Conditions will be specified so that the fluid flow is laminar. Therefore, the governing equations for the fluid are

$$\frac{\partial(\rho_f u)}{\partial x} + \frac{\partial(\rho_f v)}{\partial y} = 0 \tag{1}$$

$$\frac{\partial(\rho_f uu)}{\partial x} + \frac{\partial(\rho_f uv)}{\partial y} = -\frac{\partial p}{\partial x} + \mu_f \frac{\partial^2 u}{\partial x^2} + \mu_f \frac{\partial^2 u}{\partial y^2} \tag{2}$$

$$\frac{\partial(\rho_f vu)}{\partial x} + \frac{\partial(\rho_f vv)}{\partial y} = -\frac{\partial p}{\partial y} + \mu_f \frac{\partial^2 v}{\partial x^2} + \mu_f \frac{\partial^2 v}{\partial y^2} + \rho_f g \beta_f \Delta T \tag{3}$$

$$\frac{\partial(\rho_f c_{p,f} uT)}{\partial x} + \frac{\partial(\rho_f c_{p,f} vT)}{\partial y} = \frac{\partial}{\partial x}\left(k_f \frac{\partial T}{\partial x}\right) + \frac{\partial}{\partial y}\left(k_f \frac{\partial T}{\partial y}\right) \tag{4}$$

where u and v are the x and y components of the velocity respectively, p is the pressure, μ_f is the viscosity, ρ_f is the

density, β_f is the coefficient of thermal expansion, $c_{p,f}$ is the specific heat, and k_f is the thermal conductivity of the fluid. Heat transfer in the solid is governed by an energy equation similar to Equation (4), but with $u = v = 0$ and k_s specified instead of k_f. Radiation heat transfer is neglected, so at the solid-fluid interface the heat flux in the solid normal to the interface is equal to the heat flux in the fluid normal to the interface, and the temperature of the solid is equal to the temperature of the fluid. No-slip conditions are applied at the boundaries of the domain.

Local temperatures and heat fluxes are obtained using the finite volume method (Patankar 1980), with each control volume being entirely solid or entirely fluid. A staggered grid was used to solve the discretized forms of the Navier-Stokes equation, the power-law differencing scheme was employed, and harmonic mean thermal conductivities were calculated to properly determine thermal conditions at the control volume surfaces that separate the solid and fluid phases. The equations were solved using the SIMPLE algorithm. Because it is not known *a priori* how the solid and fluid sub-domains will evolve, the entire computational domain was populated with control volumes of uniform size. The computational model was validated as discussed in the Appendix.

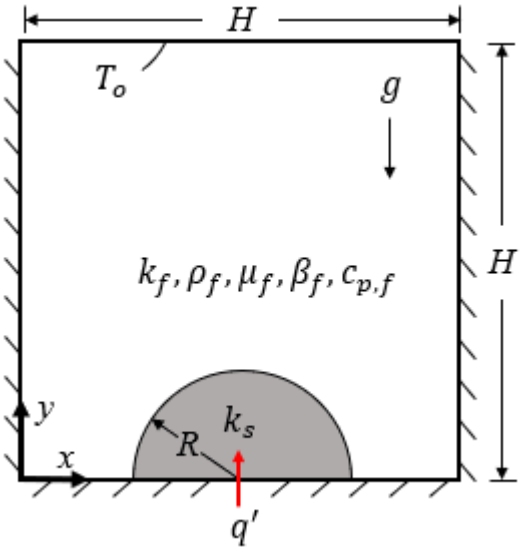

Fig. 1 Conjugate conduction-convection system showing the initial solid location and computational domain, relevant thermophysical properties, and thermal boundary conditions.

2.2 Shape Evolution Methods

A flow chart of the overall EDM is shown in Fig. 2. The simulation begins with specification of an initial solid geometrical shape (Fig. 1). The governing heat transfer equations are then solved using the HT sub-model, and all local heat fluxes and temperatures along the solid-fluid interface are calculated. Within each iteration of the EDM, one control volume is switched from solid to fluid, while a second control volume is concurrently switched from fluid to solid in adherence to a specified SEM.

As discussed in Section 1, the solid reallocation associated with the SEM is similar to that of structural evolutionary methods such as BESO, where solid is removed from locations where it is less beneficial and added to locations where it is more useful. Unlike structural problems, however, evolutionary solid reallocation schemes for conjugate conduction-convection heat transfer problems are less obvious because (*i*) addition or subtraction of solid along the interface will affect the fluid flow in a nonlinear manner and (*ii*) the solid is of relatively high thermal conductivity and therefore poses a small thermal resistance relative to that posed by the fluid. Four SEMs are considered here.

In SEM I, all solid (fluid) control volumes along the solid-fluid interface are checked, and the solid (fluid) is converted to fluid (solid) in the control volume that experiences the largest (smallest) heat flux to the fluid (from the solid). In SEM II, all solid (fluid) control volumes along the solid-fluid interface are checked, and solid (fluid) is converted to fluid (solid) in the control volume with the lowest (highest) surface temperature. SEM III is the opposite of SEM II, that is, all solid (fluid) control volumes along the solid-fluid interface are checked, and solid (fluid) is converted to fluid (solid) in the control volume with the highest (lowest) surface temperature. SEM IV is the opposite of SEM I, that is, all solid (fluid) control volumes along the solid-fluid interface are checked, and the solid (fluid) is converted to fluid (solid) in the control volume that experiences the smallest (largest) heat flux to the fluid (from the solid).

The overall EDM simulation is curtailed when either of two criteria is achieved. The first curtailment criterion is reached when part of the solid becomes disconnected from the rest of the solid and a boundary of the domain, resulting in some of the solid "floating" unrealistically within the surrounding fluid. The second curtailment criterion is met when the predicted solid shape oscillates from iteration-to-iteration, marking the end of the solid shape evolution.

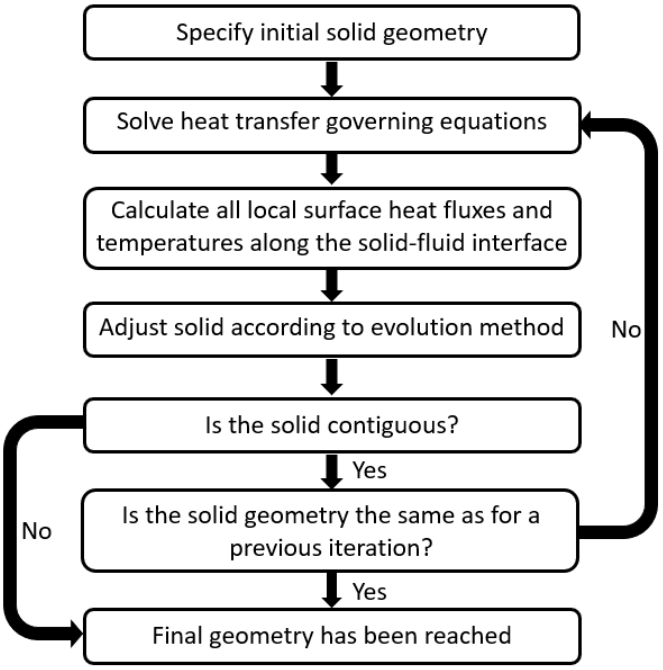

Fig. 2 The evolutionary design method (EDM).

3. EDM PREDICTIONS

Results are presented for the following cases. Prior to employing the full EDM, the HT sub-model (without utilizing a SEM) is used to both (*i*) replicate the heat transfer and fluid flow predictions and (*ii*) quantify the overall thermal resistance of the conjugate conduction/convection system, $R_t' \equiv [T(H/2\,,0) - T_o]/q'$, associated with the benchmark solid shape predicted by Coffin and Maute (2016). Second, using the same conditions specified by Coffin and Maute (2016), final solid shapes and the associated overall thermal resistances are reported for predictions generated by the overall EDM model using each of the four SEM sub-models described in Section 2.2. After these predictions are reported, an additional constraint is imposed in the EDM model of Fig. 2, and results are discussed. Finally, the influence of (*i*) the solid phase thermal conductivity and (*ii*) the domain size (Rayleigh number) on the final solid shape and overall thermal resistance is examined.

3.1 Replication of Benchmark Predictions and Quantification of the Benchmark Thermal Resistance

To test the HT sub-model and quantify R_t' associated with the benchmark study (Coffin and Maute, 2016), the materials (k_f = 0.0257 W/m·K; k_s = 237 W/m·K; ρ_f = 1.205 kg/m^3; μ_f = 1.511×10^{-5} Pa·s; $c_{p,f}$ = 1005 J/kg·K; $c_{p,s}$ = 910 J/kg·K, β_f = 3.43×10^{-3} K^{-1}), domain size (H = 30 mm), and thermal boundary conditions (q' = 0.05 W/m, T_o = 1 K) of the benchmark were specified for the problem of Fig. 1.

The optimal shape of the benchmark study is shown in Fig. 3a, along with the predicted benchmark temperature and streamline distributions. As evident, thermal and velocity conditions are not symmetric about $x = H/2$ despite the symmetric conditions of the problem and consist of a large clockwise circulation of the fluid (air) that sculpts an irregular, nearly-isothermal sloped solid that is thicker on the LHS of the computational domain. Note that no solid is in contact with the left adiabatic wall of the domain; this is attributed to the complexity of the conjugate conduction and convection heat transfer processes as well as inclusion of an additional constraint in the benchmark model. Specifically, the total perimeter of the solid was constrained by Coffin and Maute (2016); a similar constraint was not incorporated in this study due to the use of an orthogonal computational mesh. The consequence of this additional constraint will be discussed further in Section 3.3.

To demonstrate the veracity of the HT sub-model, the solid shape of Fig. 3a was replicated and is shown in Fig. 3b. The HT sub-model was then applied to the combined solid-fluid domain resulting in the predicted streamline (Fig. 3c) and temperature (Fig. 3d) distributions shown, which are in excellent qualitative agreement with those of the benchmark (Fig. 3a). The maximum temperature reported by Coffin and Maute (2016) is $T(H/2,0)$ = 2.16 K while the maximum temperature predicted by the HT sub-model is $T(H/2,0)$ = 2.19 K. The predicted thermal resistance associated with Fig. 3d is $R_t' = 23.888\ \mathrm{K \cdot m/W}$.

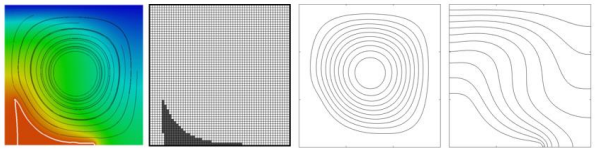

Fig. 3 Solid shape (white line), temperature and streamline distributions: (a) benchmark predictions (Coffin and Maute, 2016), (b) solid shape (black area) used in the HT sub-model, (c) streamline distribution predicted by the HT sub-model, (d) temperature distribution predicted by the HT sub-model. Figure 3(a) is reprinted by permission from Springer Nature Customer Service Centre GmbH: Springer, Structural and Multidisciplinary Optimization, "A Level-Set Method for Steady-State and Transient Natural Convection Problems," Peter Coffin and Kurt Maute, 2016.

3.2 Shape Evolution using the Four SEM Sub-models

With the accuracy of the HT sub-model demonstrated, the overall EDM model, composed of the HT and SEM sub-models, was used to predict the topology of the solid of total area A_t = 39.5 mm^2. Solid shapes at various stages of iteration of the overall EDM model, corresponding to a cumulative amount of displaced solid A_D, and number of design iterations, *iter*, are shown in Fig. 4 for each of the four SEM sub-models. For SEM Method IV, the final shape was reached after only A_D = 1 mm^2 of solid was displaced, which corresponds to 4 design iterations, and is shown in the upper right corner of the figure. With use of SEM IV, curtailment of the EDM was triggered by the oscillation between two solid shapes on subsequent iterations resulting in $R_t' = 28.008\ \mathrm{K \cdot m/W}$. Shapes corresponding to A_D = 1 mm^2 are also shown for the other three SEMs in the top row of the figure.

When A_D = 7 mm^2, the solid shape predicted using SEM III becomes separated from itself, resulting in part of the solid being artificially suspended in the fluid, and the simulation was curtailed. Just prior to solid separation, $R_t' = 27.375\ \mathrm{K \cdot m/W}$.

Although the solid shapes predicted with SEM I and SEM II are similar when A_D = 7 mm^2, the shape predicted using SEM II is noticeably more symmetric. Shortly thereafter, at A_D = 8 mm^2, the simulation associated with SEM II was curtailed due to oscillation between solid shapes in subsequent iterations with $R_t' = 27.041\ \mathrm{K \cdot m/W}$. In contrast, the solid shape predicted with use of SEM I continues to evolve, and eventually reaches its final configuration only after a significant amount of solid is displaced. (Interestingly, the amount of displaced solid exceeds the amount of solid present, A_D = 43 mm^2 > A_t).

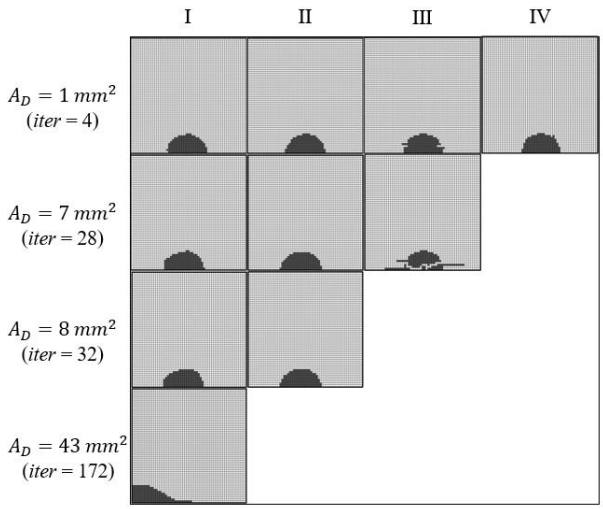

Fig. 4 Solid shapes generated by each of the four SEM sub-models. The final shapes are those at the bottom of each column.

The final shape predicted using SEM I bears similarity to that of the benchmark (Fig. 3a), with the sloped solid being thicker on the LHS of the domain. Unlike the benchmark, however, the solid makes contact with the vertical LHS insulated surface of the enclosure. The thermal resistance associated with the final shape is $R_t' = 26.126\ \mathrm{K \cdot m/W}$ Curtailment of the simulation was triggered by the oscillation between solid shapes on subsequent iterations of the EDM. Hence, the solid that is shown is the final shape generated by the overall EDM model.

A magnified view of the final (A_D = 43 mm^2) predicted solid shape using SEM I, along with the corresponding streamline and isotherm distributions are presented in Fig. 5.

Similar to the benchmark results of Fig. 3, the system displays highly asymmetrical behavior with the solid displaced in the direction of the adjacent fluid velocities, resulting in sculpting effects similar to those noted for the benchmark result shown in Fig. 3a. The streamline and temperature distributions of Figs. 3 and 5 are also qualitatively similar. Unlike the solid of the benchmark study (Fig. 3a), however, no constraints were employed to generate the results of Fig. 5 with respect to the solid's peripheral length, so the disparity between the details of final solid shape predicted here and that of the benchmark is not surprising.

The evolution (open symbols) of the predicted thermal resistance associated with each SEM, as well as that of the benchmark geometry (dashed line), is reported in Fig. 6. The filled symbols correspond to the four final geometries of Fig. 4. As is evident for all of the SEM sub-models employed, the thermal resistance generally decreases as more solid is displaced. This trend is attributed to the fact that the total area of the solid-fluid interface generally increases as adjustments are made to the solid shape. Compared to SEM II through SEM IV however, SEM I displaced over four times as much solid and has the smallest final thermal resistance.

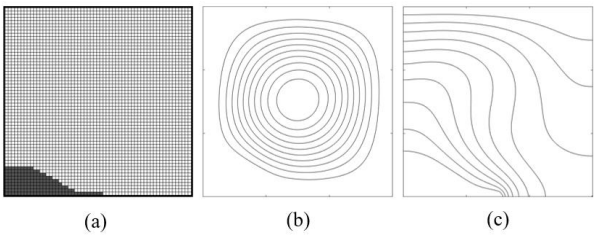

Fig. 5 EDM predictions using SEM I: (a) final solid geometry, (b) streamline distribution, (c) temperature distribution.

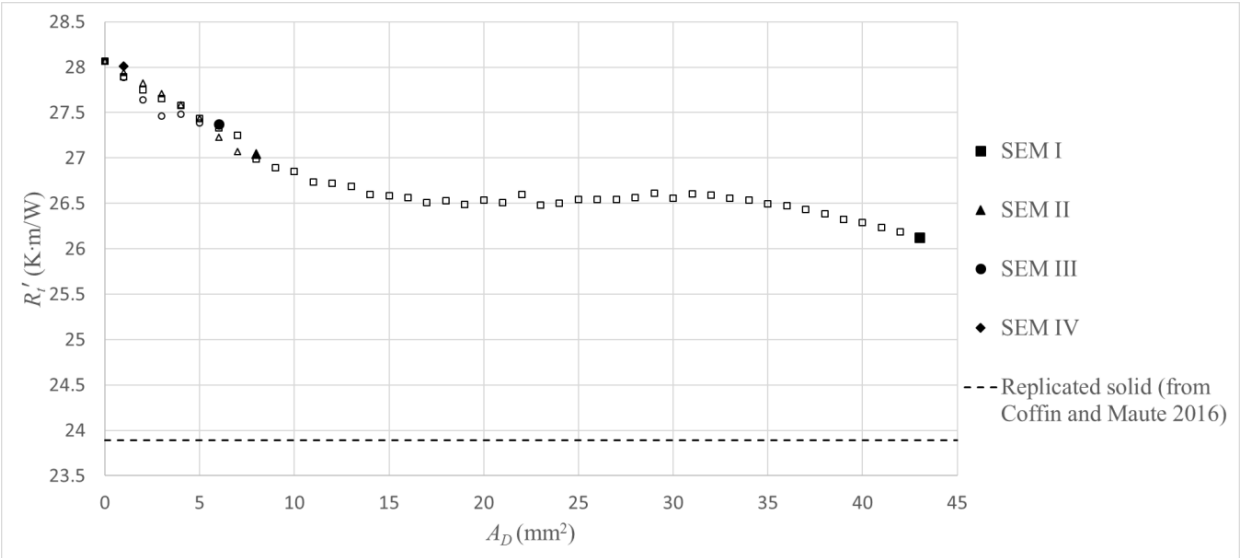

Fig. 6 Evolution of the thermal resistance for each SEM, and that of the benchmark geometry. Filled symbols are associated with the final geometries.

Although the solid geometry predicted by SEM I (Fig. 5a) is similar in shape to that of the benchmark (Fig. 3a) its thermal resistance ($R_t' = 26.126\ \mathrm{K \cdot m/W}$) is closer in value to that of the initial geometry (Fig. 1, $R_t' = 28.062\ \mathrm{K \cdot m/W}$) than to

that of the benchmark ($R_t' = 23.888\ \mathrm{K \cdot m/W}$). This result is unexpected, and is attributed to the buildup of solid adjacent to the insulated left face of the enclosure that is promoted by SEM I. The solid adjacent to the insulated vertical wall is relatively inactive thermally, and might be better utilized if it had been moved from the adiabatic boundary to the upper surface of the solid.

3.3 IMPLEMENTATION OF A CUTOFF CONSTRAINT IN SEM I

SEM I operates by moving solid to the solid-fluid interface location that experiences the smallest heat flux. Hence, the solid will accelerate toward an adiabatic boundary, eventually becoming thermally inactive as it makes contact with the boundary. In order to prevent the solid from reaching the insulated LHS of the domain, SEM I was modified by introducing an additional criterion that, as will become evident, prohibits the solid from making contact with the insulated vertical surface. This modification is based on a cutoff heat flux, q_c'' , that is quantified in terms of a cutoff ratio, R_c, and the maximum local heat flux along the solid-fluid interface, q_{max}''. If the local heat flux along the solid-fluid interface is below the cutoff heat flux, solid will not be added to that location. Therefore, the modified version of SEM I is as follows.

(1) Remove solid from the location of q_{max}'' and

(2) Add the same amount of solid to the location of the smallest q'' that is greater than q_C'' where

$$q_C'' = q_{max}'' \times R_C \tag{5}$$

To demonstrate the modified SEM I, a value of $R_C = 0.05$ was specified and the EDM predictions were compared to those using the un-modified version of SEM I ($R_C = 0$). The final solid shape, streamline distribution and temperature distribution are presented in Fig. 7. Clearly, implementation of the cutoff criterion prevents the solid from contacting the adiabatic wall, with the final solid shape (with $R_C = 0.05$) bearing more similarity to the benchmark shape than the shape predicted with the un-modified version of SEM I ($R_C = 0$). Despite being in better qualitative agreement with the benchmark shape, the thermal resistance associated with the final shape and $R_C = 0.05$ is $R_t' = 26.119\ \mathrm{K \cdot m/W}$ which is approximately the same as for the solid of Fig. 5a.

The evolution history of the thermal resistance generated by use of SEM I with and without the cutoff ratio criterion is shown in Fig. 8. The cutoff criterion using $R_C = 0.05$ comes into play only when $A_D = 24\ \mathrm{mm}^2$. For $A_D > 24\ \mathrm{mm}^2$, the thermal resistance is smaller for $R_C = 0.05$ than for $R_C = 0$, although the differences in the values of R_t' predicted with and without the cutoff ratio imposed are small.

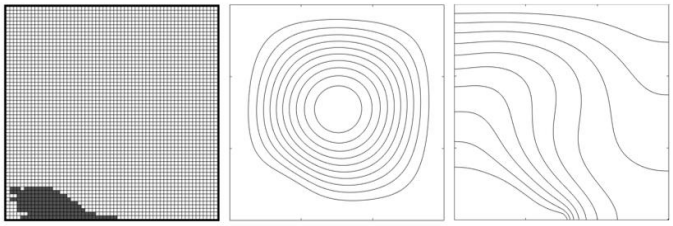

Fig. 7 EDM predictions using SEM I with $R_C = 0.05$: (a) final solid geometry, (b) streamline distribution, (c) temperature distribution.

3.4 Parametric Simulations

As demonstrated in Section 3.2 and 3.3, the EDM model is able to predict solid shapes that are in qualitative agreement with those of the benchmark, resulting in reduced thermal resistances across the computational domain. Because heat transfer across the domain is due to conduction in the solid phase and convection in the fluid, parametric simulations were performed in order to assess the sensitivity of the predicted solid shape (and the corresponding thermal resistance) to changes in the conduction process (i.e. variations in the thermal conductivity of the solid), and changes in the convection process (i.e. the size of the computational domain, or Rayleigh number).

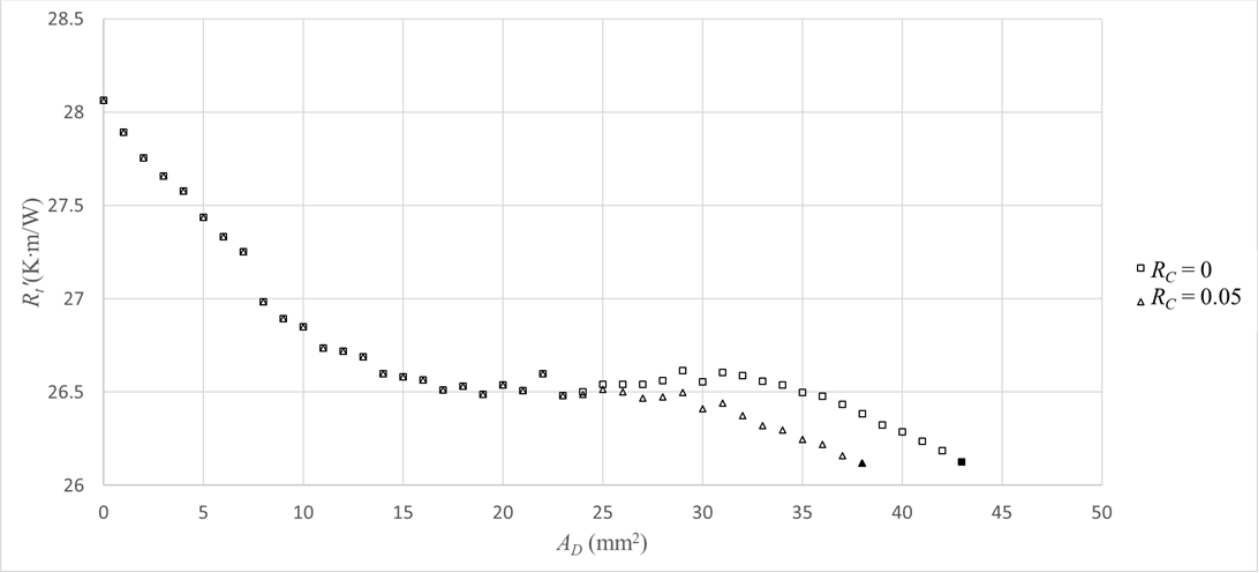

Fig. 8 Evolution of the thermal resistance for SEM I with and without a cutoff ratio constraint. Filled symbols are associated with the final geometries

Influence of the solid thermal conductivity The thermal conductivity of the solid used in the benchmark study and in the preceding simulations is approximately 5 orders of magnitude greater than that of the fluid. Therefore, the solid exhibits nearly isothermal conditions throughout. Figure 9 shows the final predicted solid shape, thermal resistance and amount of displaced solid using SEM I with $R_C = 0$ for k_s = 237, 23.7, and 2.37 W/m·K. Slight differences in the solid shapes corresponding to k_s = 237 and 23.7 W/m·K can be noted upon close inspection. Decreasing the solid's thermal conductivity would generally lead to a higher overall thermal resistance, but as evident, the thermal resistance is slightly lower for the k_s = 23.7 W/m·K case than for the k_s = 237 W/m·K benchmark case. This unexpected result is attributed to offsetting effects associated with the modest differences in the solid (and fluid) domain shapes of Fig. 9a and Fig. 9b. As the value of the solid phase thermal conductivity is further reduced to k_s = 2.37 W/m·K (Fig. 9c), the solid shape exhibits a notably different shape relative to the two higher thermal conductivity simulations, and the thermal resistance begins to increase. Additional reductions in k_s (not shown) result in even greater values of the overall thermal resistance.

Predictions using SEM I and R_C = 0.05 are shown in Fig. 10 and exhibit the same trends as noted in Fig. 9. Again, the k_s = 23.7 W/m·K case (Fig. 10b) yields the lowest overall thermal resistance.

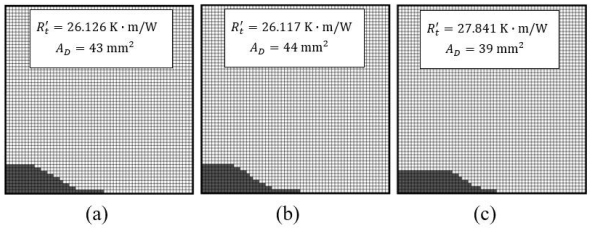

Fig. 9 Predicted solid shape and thermal resistance for SEM I, R_C = 0: (a) k_s = 237 W/m·K, (b) k_s = 23.7 W/m·K, (c) k_s = 2.37 W/m·K.

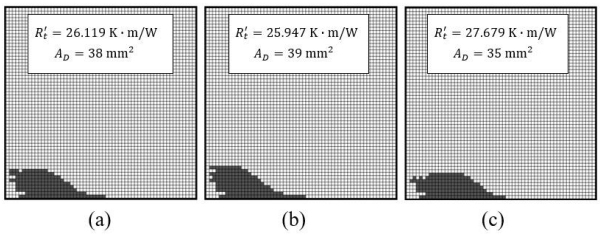

Fig. 10 Predicted solid shape and thermal resistance for SEM I, R_C = 0.05: (a) k_s = 237 W/m·K, (b) k_s = 23.7 W/m·K, (c) k_s = 2.37 W/m·K.

Influence of the strength of convection (Rayleigh number) Uniformly increasing the size of the overall domain, while holding all other conditions constant, will strengthen convection heat transfer and is expected to reduce the overall thermal resistance. Figure 11 shows the final solid shape, thermal resistance, and amount of solid displaced using SEM I with R_C = 0 for H = 30, 45, and 60 mm. Note that the Rayleigh number associated with each domain size is calculated using the maximum predicted temperature difference, $Ra = g\beta_f \Delta T H^3/\nu_f \alpha_f$, where $\alpha_f = k_f/\rho_f c_{p,f}$. As evident in the figure, (*i*) the overall resistance is decreased by approximately 40 percent as a result of doubling H and (*ii*) the solid shapes associated with larger Ra exhibit better qualitative resemblance to the optimized shape of Coffin and Maute (2016). The effect of the increased strength of convection on the final solid shape is as expected. Figure 12 illustrates the sensitivity of the final solid shape, thermal resistance, and amount of solid displaced using SEM I and $R_C = 0.05$ on the domain size. As for the R_C = 0 case, the solid shapes associated with higher Rayleigh numbers have lower thermal resistances and are in better qualitative agreement with those of the benchmark prediction.

The evolution history of the overall thermal resistance using SEM I and H = 60 mm is shown in Fig. 13. Unlike the

trends evident in Fig. 8 (H = 30 mm), the predictions exhibit a more substantial increase in thermal resistance (for $10 \lesssim A_D \lesssim 25$) followed by a decrease in the thermal resistance to its final value. For $10 \lesssim A_D \lesssim 25$, the solid is being moved toward the LHS vertical adiabatic boundary. As the boundary is approached, the solid becomes less thermally active, increasing the overall thermal resistance. The increase in the thermal resistance is not as pronounced for the lower Rayleigh number cases (Fig. 8) because the solids for those cases retain somewhat semi-circular shapes as they approach the LHS boundary, whereas the solids associated with Fig. 13 transition from semi-circular shapes to flatter shapes in the range $10 \lesssim A_D \lesssim 25$. The flattening solids become further removed from the cold top boundary, increasing the overall thermal resistances to a more significant degree than for the lower Ra cases. For either case, for $A_D \gtrsim 30$ the solids become less flat and evolve upward as shown in Figs. 11a and 11c, increasing the exposed solid surface area and reducing the thermal resistance.

The percentage reductions in thermal resistance for the three different domain sizes, using SEM I with and without implementation of the cutoff ratio, are presented in Table 1. The largest reduction in thermal resistance is associated with the lowest Rayleigh number. Implementation of the cutoff ratio has a greater effect for the larger Rayleigh number cases

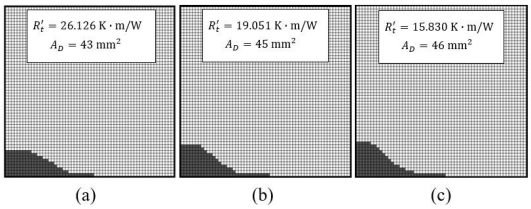

Fig. 11 Predicted solid shape and thermal resistance for SEM I, R_C = 0: (a) H = 30 mm (Ra = 4460), (b) H = 45 mm (Ra = 10980), (c) H = 60 mm (Ra = 21620).

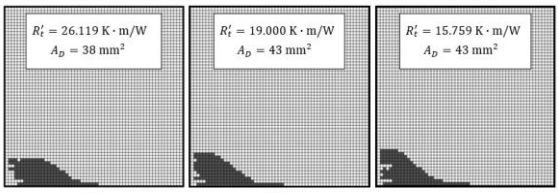

Fig. 12 Predicted solid shape and thermal resistance for SEM I, R_C = 0.05: (a) H = 30 mm (Ra = 4458), (b) H = 45 mm (Ra = 9079), (c) H = 60 mm (Ra = 21520).

Table 1 Percent reduction of R_t' from initial shape to final shape generated by EDM.

	R_C = 0	R_C = 0.05
H = 30 mm	6.90%	6.92%
H = 45 mm	3.20%	3.46%
H = 60 mm	2.93%	3.37%

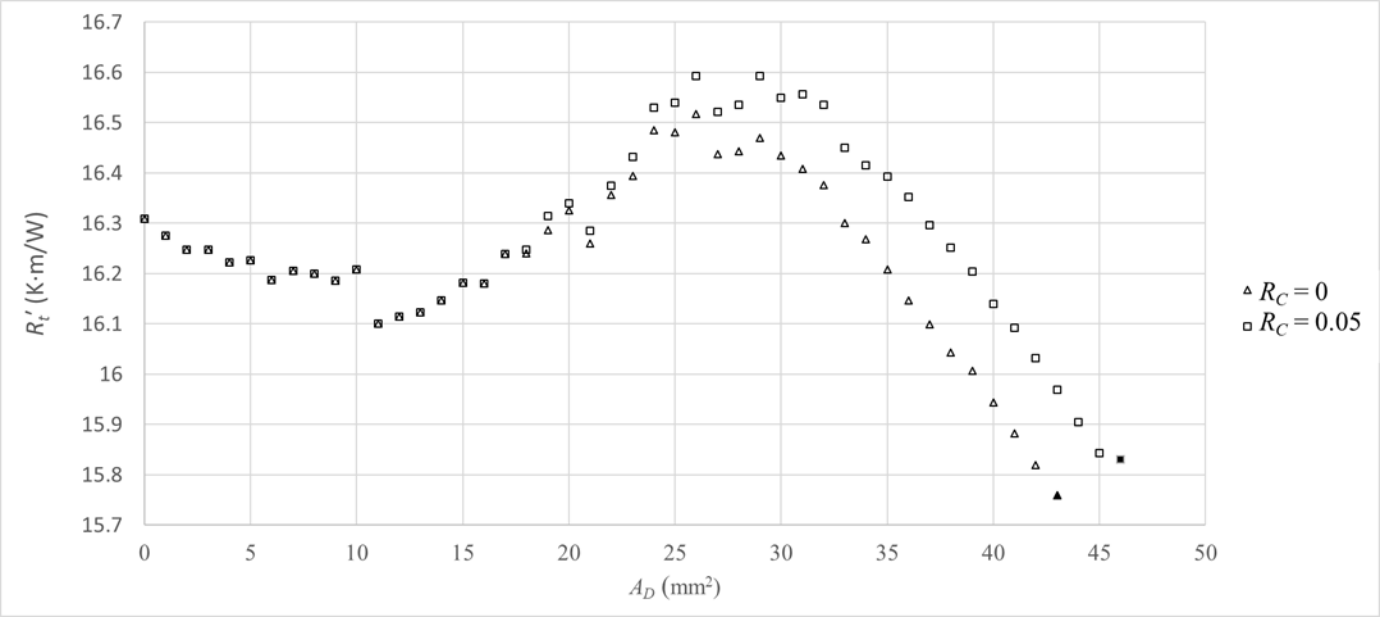

Fig. 13 Evolution of the thermal resistance for SEM 1 when H = 60 mm with and without a cutoff ratio constraint. Rayleigh numbers range from Ra_{min} = 21,520 at A_D = 43 mm² with R_c = 0.05 to Ra_{max} = 22,660 at A_D = 26 mm² with R_c = 0. Filled symbols are associated with the final geometries.

4. SUMMARY, CONCLUSIONS, AND RECOMMENDATIONS

A novel EDM model, consisting of heat transfer (HT) and shape evolution method (SEM) sub-models was developed and its use was demonstrated. Four SEMs were considered, and predictions were compared to a benchmark optimized design. The best performance was achieved using SEM I in which high thermal conductivity material is removed from the location of the largest interfacial heat flux and added to the location of the smallest flux. An additional constraint was proposed and examined, with the objective of prohibiting the solid from contacting the adiabatic side boundary of the domain. This constraint lead to a thermal resistance similar in value to that predicted without the constraint. Parametric simulations were conducted to assess the influence of conduction (solid thermal conductivity) and convection (Rayleigh number). Perhaps unexpectedly, a solid thermal conductivity value (23.7 W/m·K) lower than that used in the benchmark led to a final solid shape with a lower overall thermal resistance. Increasing the strength of convection decreased the thermal resistance and resulted in final solid shapes that bear a closer resemblance to the benchmark study.

The decrease in R_t' and qualitative similarity of the solid shape generated by SEM I relative to a benchmark solid shape suggest there is merit to using SEM I. However, the predicted thermal resistance is greater than that of the optimized design. Hence, although the EDM proposed here is straightforward and easily implemented, it lacks the accuracy of more complex optimization routines.

General recommendations for future research include: (*i*) improving the relatively straightforward evolutionary methods proposed here to achieve the high accuracy of TO methods or (*ii*) developing new computational techniques to reduce the expense of high accuracy TO methods. More specifically, improving the evolutionary methods proposed here might entail: (*i*) specification of different material re-distribution rules, (*ii*) incorporation of additional or new constraints to guide the evolution of the solid shape, and (*iii*) developing new or additional curtailment criteria to allow the solid to more fully evolve.

ACKNOWLEDGEMENTS

The authors acknowledge Dr. Hamidreza Shabgard of the University of Oklahoma for his assistance. The first author acknowledges support from the University of Kansas by way of the Wallace S. Strobel Scholarship.

NOMENCLATURE

A_D	area of displaced solid (mm^2)
A_t	total solid area (mm^2)
c_p	specific heat (J/kg·K)
g	gravitational acceleration (m/s^2)
H	domain length (mm)
k	thermal conductivity (W/m·K)
Nu	Nusselt number
p	pressure (Pa)
q'	heat rate per unit length (W/m)
q''	heat flux (W/m^2)
Ra	Rayleigh number
R_C	cutoff ratio
R_t'	thermal resistance (K·m/W)
T	temperature (K)
T_o	reference temperature (K)
u	x-velocity (m/s)
v	y-velocity (m/s)
x	x-coordinate (m)
y	y-coordinate (m)

Greek Symbols

α	thermal diffusivity (m^2/s)
β	coefficient of thermal expansion (K^{-1})
μ	dynamic viscosity (Pa·s)
ρ	density (kg/m^3)

Subscripts

c	cutoff
f	fluid
max	maximum
min	minimum
s	solid

REFERENCES

Ahn, S.H., and Cho, S., 2010, "Level Set-Based Topological Shape Optimization of Heat Conduction Problems Considering Design-Dependent Convection Boundary," *Numerical Heat Transfer Part B-Fundamentals*, **58**(5), 304-322. https://doi.org/10.1080/10407790.2010.522869

Alexandersen, J., Aage, N., Andreasen, C.S., and Sigmund, O., 2014, "Topology Optimization for Natural Convection Problems," *International Journal for Numerical Methods in Fluids*, **76**(10), 699-721. https://doi.org/10.1002/fld.3954

Alexandersen, J., Sigmund, O., Meyer, K.E., and Lazarov, B.S., 2018, "Design of Passive Coolers for Light-Emitting Diode Lamps Using Topology Optimisation," *International Journal of Heat and Mass Transfer*, **122**, 138-149. https://doi.org/10.1016/j.ijheatmasstransfer.2018.01.103

Bar-Cohen, A., 1979, "Fin Thickness for an Optimized Natural Convection Array of Rectangular Fins," *Journal of Heat Transfer*, **101**(3), 564-566. https://doi.org/10.1115/1.3451032

Bar-Cohen, A., Iyengar, M., and Kraus, A., 2003 "Design of Optimum Plate-Fin Natural Convective Heat Sinks," *Journal of Electronic Packaging*, **125**(2), 208-216 https://doi.org/10.1115/1.1568361

Bendsøe, M.P., and Kikuchi, N., 1988, "Generating Optimal Topologies in Structural Design Using a Homogenization Method," *Computer Methods in Applied Mechanics and Engineering*, **71**(2), 197-224. https://doi.org/10.1016/0045-7825(88)90086-2

Bendsøe, M.P., and Sigmund, O., 2003, *Topology Optimization: Theory, Methods, and Applications.* Springer, Berlin. https://doi.org/10.1007/978-3-662-05086-6

Borrvall, T., and Petersson, J., 2003, "Topology Optimization of Fluids in Stokes Flow," *International Journal for Numerical Methods in Fluids*, **41**(1), 77-107. https://doi.org/10.1002/fld.426

Bruns, T.E., 2007, "Topology Optimization of Convection-Dominated, Steady-State Heat Transfer Problems," *International Journal of Heat and Mass Transfer*, **50**(15-16), 2859-2873. https://doi.org/10.1016/j.ijheatmasstransfer.2007.01.039

Coffin, P., and Maute, K., 2016, "A Level-Set Method for Steady-State and Transient Natural Convection Problems," *Structural and Multidisciplinary Optimization*, **53**(5), 1047-1067. https://doi.org/10.1007/s00158-015-1377-y

Costa, V.A.F., 2012, "Natural Convection in Partially Divided Square Enclosures: Effects of Thermal Boundary Conditions and Thermal Conductivity of the Partitions," *International Journal of Heat and Mass Transfer*, **55**(25-26), 7812-7822. https://doi.org/10.1016/j.ijheatmasstransfer.2012.08.004

de Vahl Davis, G., 1983, "Natural Convection of Air in a Square Cavity: A Bench Mark Numerical Solution," *International Journal for Numerical Methods in Fluids*, **3**(3), 249-264. https://doi.org/10.1002/fld.1650030305

Dirker, J., and Meyer, J.P., 2013, "Topology Optimization for an Internal Heat-Conduction Cooling Scheme in a Square Domain for High Heat Flux Applications," *Journal of Heat Transfer*, **135**(11), 111010. https://doi.org/10.1115/1.4024615

Gao, T., Zhang, W.H., Zhu, J.H., Xu, Y.J., and Bassir, D.H., 2008, "Topology Optimization of Heat Conduction Problem Involving Design-Dependent Heat Load Effect," *Finite Elements in Analysis and Design*, **44**(14), 805-813. https://doi.org/10.1016/j.finel.2008.06.001

Gersborg-Hansen, A., Bendsøe, M.P., and Sigmund, O., 2006, "Topology Optimization of Heat Conduction Problems Using the Finite Volume Method," *Structural and Multidisciplinary Optimization*, **31**(4), 251-259. https://doi.org/10.1007/s00158-005-0584-3

Haertel, J.H.K., and Nellis, G.F., 2017, "A Fully Developed Flow Thermofluid Model for Topology Optimization of 3D-printed Air-cooled Heat Exchangers," *Applied Thermal Engineering*, **119**, 10-24. https://doi.org/10.1016/j.applthermaleng.2017.03.030

Joo, Y. Lee, I. and Kim, S.J., 2017, "Topology Optimization of Heat Sinks in Natural Convection Considering the Effect of Shape-Dependent Heat Transfer Coefficient," *International Journal of Heat and Mass Transfer*, **109**, 123-133. https://doi.org/10.1016/j.ijheatmasstransfer.2017.01.099

Kim, D., 2012, "Thermal Optimization of Plate-fin Heat Sinks with Fins of Variable Thickness Under Natural Convection," *International Journal of Heat and Mass Transfer*, **55**(4)**,** 752-761. https://doi.org/10.1016/j.ijheatmasstransfer.2011.10.034

Koga, A.A., Lopes, E.C.C., Nova, H.F.V., de Lima, C.R., and Silva, E.C.N., 2013, "Development of Heat Sink Device by Using Topology Optimization," *International Journal of Heat and Mass Transfer*, **64,** 759-772. https://doi.org/10.1016/j.ijheatmasstransfer.2013.05.007

Li, Q., Steven, G.P., Querin, O.M., and Xie, Y.M., 1999, "Shape and Topology Design for Heat Conduction by Evolutionary Structural Optimization," *International Journal of Heat and Mass Transfer*, **42**(17), 3361-3371. https://doi.org/10.1016/S0017-9310(99)00008-3

Li, Q., Steven, G.P., Xie, Y.M., and Querin, O.M., 2004, "Evolutionary Topology Optimization for Temperature Reduction of Heat Conducting Fields," *International Journal of Heat and Mass Transfer*, **47**(23), 5071-5083. https://doi.org/10.1016/j.ijheatmasstransfer.2004.06.010

Marck, G., Nemer, M., Harion, J.L., Russeil, S., and Bougeard, D., 2012, "Topology Optimization Using the SIMP Method for Multiobjective Problems," *Numerical Heat Transfer Part B*, **61**(6), 439-470. https://doi.org/10.1080/10407790.2012.687979

Patankar, S.V., 1980, *Numerical Heat Transfer and Fluid Flow*, 1st ed., McGraw-Hill, New York.

Qian, X., and Dede, E.M., 2016, "Topology Optimization of a Coupled Thermal-Fluid System Under a Tangential Thermal Gradient Constraint," *Structural and Multidisciplinary Optimization*, **54**(3), 531-551. https://doi.org/10.1007/s00158-016-1421-6

Sigmund, O., and Maute, K., 2013, "Topology Optimization Approaches," *Structural and Multidisciplinary Optimization*, **48**(6), 1031-1055. https://doi.org/10.1007/s00158-013-0978-6

Subramaniam, V., Dbouk, T., and Harion, J.L., 2019, "Topology Optimization of Conjugate Heat Transfer Systems: A Competition Between Heat Transfer Enhancement and Pressure Drop Reduction," *International Journal of Heat and Fluid Flow*, **75**, 165-184. https://doi.org/10.1016/j.ijheatfluidflow.2019.01.002

Xia, Q., Shi, T., and Xia, L., 2018, "Topology Optimization for Heat Conduction by Combining Level Set Method and BESO Method," *International Journal of Heat and Mass Transfer*, **127**, 200-209. https://doi.org/10.1016/j.ijheatmasstransfer.2018.08.036

Yin, L., and Ananthasuresh, G., 2002, "A Novel Topology Design Scheme for the Multi-Physics Problems of Electro-Thermally Actuated Compliant Micromechanisms," *Sensors and Actuators A*, **97-98**, 599-609. https://doi.org/10.1016/S0924-4247(01)00853-6

Yoon, G.H., 2010, "Topological design of heat dissipating structure with forced convective heat transfer," *Journal of Mechanical Science and Technology*, **24**(6), 1225-1233. https://doi.org/10.1007/s12206-010-0328-1

APPENDIX

The HT and SEM sub-models were validated to the extent possible as follows. First, predictions of the convection heat transfer aspects of the HT model were compared to the classic benchmark solution provided by de Vahl Davis (1983) involving a square cavity containing air with adiabatic top and bottom surfaces and isothermal side walls. Values of the average Nusselt number were predicted for Rayleigh numbers ranging from 10^3 to 10^6. Using a 60 × 60 uniform mesh, the largest difference between predicted average Nusselt numbers was 3.1 percent at $Ra = 10^6$. The difference between the maximum local Nusselt numbers was 7.1 percent at $Ra = 10^6$. The HT sub-model was then used to predict a benchmark solution (Costa, 2012) for natural convection of air in a partitioned cavity involving conjugate conduction-free convection heat transfer, as shown in Fig. 14. Two cases were considered: (*i*) hotter wall on the right and (*ii*) hotter wall on the left. Both a 50 × 50 mesh and a 100 × 100 mesh were employed in the comparison exercise. The average Nusselt numbers for each case are shown in Table 2. The predictions generated by the HT sub-model are in good agreement with the benchmark solutions, and there is only a slight improvement in agreement with the benchmark as the mesh is refined from 50 × 50 to 100 × 100. Based on the preceding discussion, a 60 × 60 mesh was deemed to be adequate for the computations of this study.

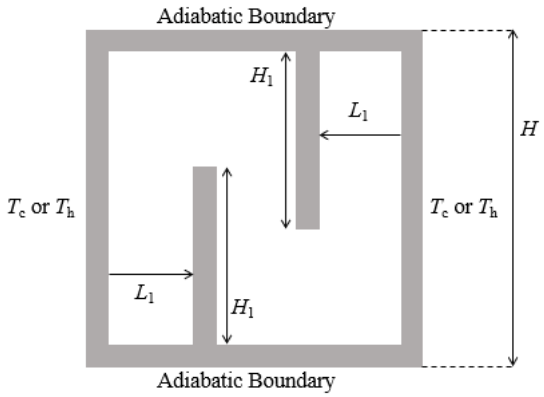

Fig. 14 Domain for the conjugate conduction-free convection benchmark solutions (Costa, 2012).

Table 2 Predicted and benchmark (Costa, 2012) average Nusselt numbers.

	Predicted $\overline{Nu}$ 50 × 50 (% error)	Predicted $\overline{Nu}$ 100 × 100 (% error)	$\overline{Nu}$ (Costa 2012)
Hot wall on left	4.374 (3.45%)	4.266 (0.90%)	4.228
Hot wall on right	5.500 (3.64%)	5.416 (2.05%)	5.307

A third comparison was made to predict the evolution of a geometrical shape in a conduction scenario similar to that considered by Li *et al.* (1999). In this comparison, an initially square domain is (*i*) completely filled with a conducting material and a second isothermal material at its square center and is (*ii*) exposed to isothermal exterior boundaries. The solid shape (defined by the interface between white and black areas in Fig. 15) evolves by continually removing control volumes adjacent to the boundaries of the solid that experience the smallest average heat flux. The boundary of the solid shape is maintained at the same temperature as the original boundary of the square domain. As evident in Fig. 15, the qualitative agreement between the two predicted solid shapes is excellent. The iteration history, showing evolution of the minimum and maximum local heat fluxes along the solid boundary is shown for both studies in Fig. 16. As in Fig. 15, the predictions and benchmark results are in good qualitative agreement, especially at later stages of the iteration when the solid shapes approach their final configurations. Differences between the current and benchmark results are attributed to the different numerical techniques used (finite volume versus finite element of Li *et al*., 1999).

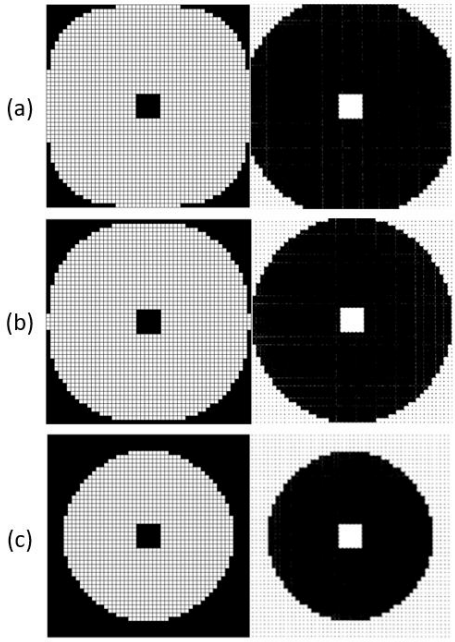

Fig. 15 Predicted solid shapes (right column) of Li *et al.* (1999) and those of the current study (left column). Shapes are shown at volume-to-initial volume ratios of (a) 88 percent, (b) 79 percent and (c) 55 percent.

RHS is reprinted from International Journal of Heat and Mass Transfer, 42-17, Li, Q., Steven, G.P., Querin, O.M., and Xie, Y.M. "Shape and Topology Design for Heat Conduction by Evolutionary Structural Optimization" 3361-3371, 1999, with permission from Elsevier.

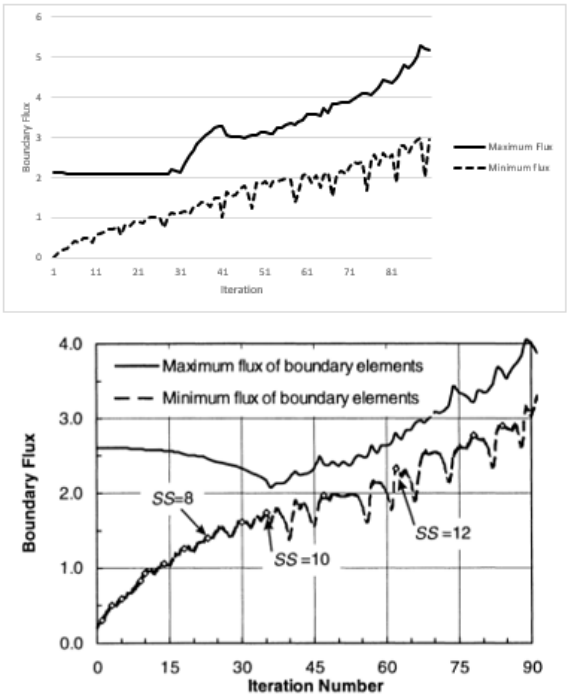

Fig. 16 Iteration history of predicted maximum and minimum local heat fluxes along the solid boundary of Fig. 15. The top figure is from the results of the current model while the bottom is from Li *et al*.(1999). Bottom figure is reprinted from International Journal of Heat and Mass Transfer, 42-17, Li, Q., Steven, G.P., Querin, O.M., and Xie, Y.M. "Shape and Topology Design for Heat Conduction by Evolutionary Structural Optimization" 3361-3371, 1999, with permission from Elsevier.

A final verification exercise was conducted to determine the sensitivity of the final predicted solid shape to the initial solid shape specified in the overall EDM model of Fig. 2. Specifically, predictions based on the semicircular initial solid considered in this study were compared to those generated by specifying an initially nearly rectangular solid containing the same amount of material as the semicircle. Figure 17 includes the initial shape (top row) and final shape without (R_C = 0, middle row) and with (R_C = 0.05, bottom row) the cutoff criterion applied. As evident, the final shapes associated with R_C = 0 are nearly independent of the initial specified shape. For R_C = 0.05, the final shapes are similar but exhibit more noticeable yet minor variations; the initially rectangular shape yielded a slightly lower (2.5 percent difference) thermal resistance than the initially semicircle shape simulation as reported in Table 3.

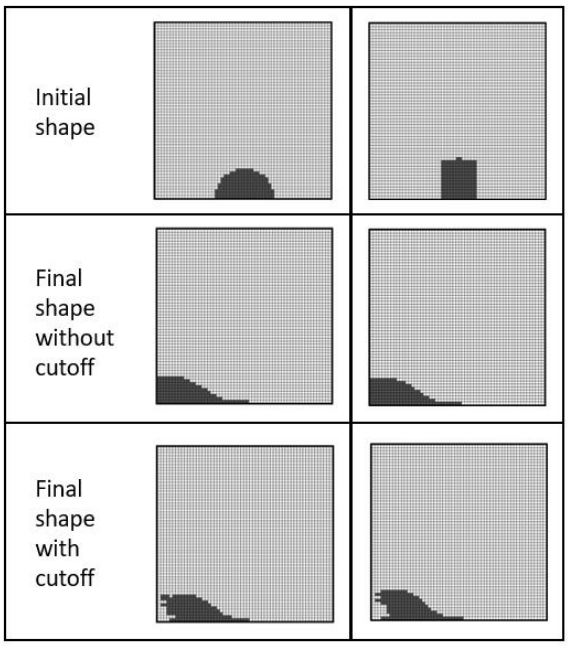

Fig. 17 Influence of the initial solid shape on the final solid shapes without (R_C = 0) and with (R_C = 0.05) the cutoff criterion.

Table 3 Predicted thermal resistances for initially semicircular and rectangular solid shapes.

	Semicircle		Rectangle	
	A_D (mm²)	R_t' (K·m/W)	A_D (mm²)	R_t' (K·m/W)
Without cutoff	43	26.126	48	25.710
With cutoff	38	26.119	48	25.525

Paper P2

Title:

Evolutionary Design Method for a Conducting Solid Cooled by Combined Free Convection and Radiation

Authors:

Chadwick D. Sevart

Theodore L. Bergman

Journal:

ASME Journal of Heat Transfer

Evolutionary Design Method for a Conducting Solid Cooled by Combined Free Convection and Radiation

Chadwick D. Sevart[1]
Department of Mechanical Engineering
University of Kansas
Lawrence, KS, 66044
e-mail: cdsevart@ku.edu

Theodore L. Bergman
Department of Mechanical Engineering
University of Kansas
Lawrence, KS, 66044
e-mail: tlbergman@ku.edu

Abstract – An iterative design algorithm is used to adjust the shape of a conducting solid body that is subjected to a surface heat flux and cooled simultaneously by free convection and radiation in order to reduce the overall thermal resistance. Parametric simulations are carried out over a range of domain dimensions and emissivity values to determine the sensitivity of (*i*) the predicted solid shape and (*ii*) the overall thermal resistance to the relative strength of convection or radiation. Results show that, for the conditions considered, surface radiation has a significant influence on the predicted optimal solid geometry and overall thermal resistance.

Keywords – *Topology Optimization, Conjugate Heat Transfer, Free Convection, Radiation*

1. Introduction

The optimal geometrical configuration of solid objects, such as heat sinks, that are cooled simultaneously by free convection and radiation is important to achieve the desired thermal performance or limit the amount of solid material used. As applied to heat sink design, this goal has been historically achieved by shape and geometrical optimization. Such methods require the solid object to be composed of well-defined, basic geometrical features that can be easily parameterized. For example, Bar-Cohen [1]

considered rectangular plate fins cooled by free convection, and optimized the fin thickness, the spacing between fins, and the fin width in order to minimize the heat sink thermal resistance. While size and shape optimization are well-developed tools to improve the performance of traditional heat sink layouts, a true optimal design may be geometrically complex and not easily described by pre-defined basic geometrical features.

The challenge of identifying desirable complex solid shapes for heat sinks or other solid objects has led to recent developments in topological optimization (TO), which was initially developed for structural engineering problems and can be used to determine the optimal distribution of solid to achieve a specific goal while satisfying various constraints [2]. There are multiple TO techniques, with each approach characterized by unique methods and implementation procedures. In general, the TO process is as follows: (*i*) a computational domain is discretized and an initial material distribution is specified, (*ii*) the governing equations which describe the physics of the problem (*e.g.* conservation of thermal energy and the Navier-Stokes equations) are solved, and (*iii*) the material distribution is adjusted according to an algorithm in order to minimize or maximize an objective function. For heat transfer problems, the objective might be to minimize the overall thermal resistance or a local temperature. Steps (*ii*) and (*iii*) are repeated until an optimal geometry is identified.

The initial applications of TO to heat transfer problems considered only conduction. For example, Li *et al*. [3] used TO to determine the optimal distribution of a high thermal conductivity material in a conducting field that provided a minimum temperature at a specified location. Topology optimization for heat conduction problems has been researched extensively and is relatively well established, as evidenced by various studies and the references contained therein [4-8].

For practical applications, it is usually necessary to consider designs involving multiple modes of heat transfer. Several studies have incorporated the effects of forced convection through specification of a constant convection coefficient and incorporation of Newton's law of cooling [9-11]. This relatively simple approach can provide approximate optimal designs, but in order to accurately capture the local effects of convection, a detailed fluid flow model involving the solution of the Navier-Stokes equations

must be employed. An early investigation that applied TO to a conjugate conduction-convection problem was described by Yoon [12], who designed a heat dissipating structure cooled by forced convection that minimized the thermal compliance of the structure. In a similar study, Koga *et al.* [13] used TO to design a microchannel heat sink that minimized the pressure drop of the flowing coolant and maximized the heat dissipation for the problem at hand. A prototype of the heat sink was manufactured, and the computational results were validated experimentally.

Alexandersen *et al*. [14] applied TO to heat sinks cooled by free convection and found the resulting optimal geometries to be intricately complex, with the complexity being highly sensitive to the strength of the local advection processes within the fluid. These methods were later extended to three-dimensional geometries [15] and applied to the cooling of light emitting diodes [16]. Asmussen *et al*. [17] introduced a reduced-order Navier-Stokes equation for the same natural convection problem considered in [14] and found that the simplified model produced similar results to the full fluid model, but with reduced computational expense.

The heat sink designs obtained in [16] were manufactured for experimental testing in [18], demonstrating that the complex geometrical structures obtained through application of TO can be physically realized through advanced manufacturing methods. Although surface radiation was not accounted for in the prediction of the optimal solid shape, the authors investigated the effect of surface radiation by applying a graphite paint to the heat sink, thus increasing its emissivity and reducing the overall thermal resistance of the structure.

While radiation heat transfer can play an important role in various heat transfer systems including heat sink operation, it is seldom accounted for in the design and shape optimization of heat sinks, particularly heat sinks of complex geometrical shape. To the authors' knowledge only one study has utilized TO for a radiative heat transfer problem, but the study neglected convection. Specifically, Castro *et al.* [19] determined the optimal distribution of a low emissivity material inside a cubic radiative enclosure. Several objective functions were considered, including (*i*) minimizing or (*ii*) maximizing the net heat flux and (*iii*) minimizing the temperature at a specified region of the enclosure. For all cases

considered by the authors, it was found that the design method used resulted in unique material distributions which offered substantial thermal performance enhancement as described quantitatively by the objective functions.

Based on the literature review and to the authors' knowledge, use of TO to determine the optimal shape of a conducting solid that is cooled *simultaneously* by free convection and radiation, a scenario that is pertinent to nearly all heat sinks exposed to the free convection of gases, has not been reported. Although it is not surprising that increasing the surface emissivity experimentally will improve the thermal performance of a heat sink that has been computationally designed with TO without taking radiation into account [18], it is entirely unclear whether inclusion of radiation in the TO process itself would yield significantly different heat sink geometries. Therefore, the objective of this study is to investigate and quantify the influence of surface radiative heat transfer on the predicted optimal shape of a conducting solid body cooled simultaneously by free convection and radiation, with the goal being to reduce the overall thermal resistance that is influenced by conjugate conduction, convection, and radiation effects. A relatively simple and evolutionary design method introduced by Sevart and Bergman [20] was modified to include the radiation effects, and is employed here.

2. Physical and Numerical Model

The physical problem of interest is shown in Fig. 1, in which a two-dimensional, square domain consists of (*i*) a specified amount of solid material and (*ii*) a radiatively transparent, incompressible gas. The top boundary of the domain is isothermal at a reference temperature of T_o, and there is a heat rate per unit depth of q' applied at the bottom of the domain over a strip of width b that is centered at $x = H/2$. All other domain boundaries are adiabatic.

All exposed surfaces, including those of the solid and the interior boundaries of the domain, are radiatively active as well as diffuse and gray with an emissivity of ε. The shape of the solid, which is initially specified to be a semicircle of radius R as shown in Fig. 1, is adjusted iteratively according to the

evolutionary design method described in Section 2.4. The goal is to minimize the overall thermal resistance between the center of the bottom domain boundary and the top domain boundary ($R_t' = [T(H/2\,,0) - T_o]/q'$). As will become evident, the overall thermal resistance and, in turn, the optimal solid shape is influenced by conjugate effects including (*i*) conduction within the solid, (*ii*) free convection in the fluid, and (*iii*) radiation exchange involving all exposed solid surfaces. Both the physical model and the design iteration model that are used here are extensions of the models previously reported by the authors [20].

2.1 Governing Equations and Boundary Conditions

Temperature distributions within both the fluid and solid are determined by solution of (*i*) the conservation of mass equation, (*ii*) the Navier-Stokes equations, and (*iii*) the conservation of energy equation applied to both the solid and the fluid, along with pertinent boundary conditions that include the effects of thermal radiation transfer at all of the exposed solid surfaces. In developing the equations, the fluid is assumed to be Newtonian and Boussinesq, and viscous dissipation is assumed to be negligible. Steady-state conditions are assumed, and the thermophysical properties are assumed to be constant. As noted previously, the surfaces are assumed to be diffuse and gray, and the fluid is radiatively non-participating. With these assumptions, the governing equations for the fluid are

$$\frac{\partial(\rho_f u)}{\partial x} + \frac{\partial(\rho_f v)}{\partial y} = 0 \tag{1}$$

$$\frac{\partial(\rho_f uu)}{\partial x} + \frac{\partial(\rho_f uv)}{\partial y} = -\frac{\partial p}{\partial x} + \mu_f \frac{\partial^2 u}{\partial x^2} + \mu_f \frac{\partial^2 u}{\partial y^2} \tag{2}$$

$$\frac{\partial(\rho_f vu)}{\partial x} + \frac{\partial(\rho_f vv)}{\partial y} = -\frac{\partial p}{\partial y} + \mu_f \frac{\partial^2 v}{\partial x^2} + \mu_f \frac{\partial^2 v}{\partial y^2} + \rho_f g \beta_f \Delta T \tag{3}$$

$$\frac{\partial(\rho_f c_{p,f} uT)}{\partial x} + \frac{\partial(\rho_f c_{p,f} vT)}{\partial y} = \frac{\partial}{\partial x}\left(k_f \frac{\partial T}{\partial x}\right) + \frac{\partial}{\partial y}\left(k_f \frac{\partial T}{\partial y}\right) \tag{4}$$

where u and v are the x- and y-components of the velocity respectively, ρ_f is the fluid density, μ_f is the viscosity, p is the pressure, β_f is the thermal expansion coefficient, $c_{p,f}$ is the specific heat, and k_f is the thermal conductivity of the fluid. The conservation of energy equation for the solid is

$$\frac{\partial}{\partial x}\left(k_s \frac{\partial T}{\partial x}\right) + \frac{\partial}{\partial y}\left(k_s \frac{\partial T}{\partial y}\right) = 0 \tag{5}$$

where k_s is the solid thermal conductivity.

The temperature along the top boundary of the domain is constant, $T(x, y = H) = T_o$, while the boundary condition at the bottom center of the domain where the heat rate is applied (over the width b) is

$$-k_s \frac{\partial T}{\partial y} = q'/b \tag{6}$$

which incorporates the additional assumptions that (*i*) the solid reconfiguration is constrained so that it always occupies the region $H/2 - b/2 \leq x \leq H/2 + b/2$ at $y = 0$ and (*ii*) the heat flux is uniform over the strip of width b. Adiabatic domain boundaries that are covered by the solid (e.g., $R \leq x \leq H/2 - b/2$ and $H/2 + b/2 \leq x \leq H/2 + R$ in Fig. 1) are described by

$$-k_s \frac{\partial T}{\partial n} = 0 \tag{7}$$

where n is the direction normal to the domain boundary.

Radiation heat transfer occurs at all exposed surfaces of the solid, as well as at the interior domain boundaries. At the interface separating the fluid and the solid, the conduction heat flux in the solid to the solid-fluid interface is equal to the summation of the convection and radiation heat fluxes from the interface. That is,

$$-k_s \frac{\partial T}{\partial n} = q''_{conv} + q''_{rad} \tag{8}$$

At locations where the adiabatic boundary is directly exposed to radiation (e.g., $0 \leq x < H/2 - b/2$ and $H/2 + b/2 < x \leq H$ in Fig. 1) local convection fluxes are offset by local radiation fluxes leading to

$$q''_{conv} + q''_{rad} = 0 \tag{9}$$

which can also be expressed as

$$-k_f \frac{\partial T}{\partial n} + q''_{rad} = 0 \tag{10}$$

Evaluation of the radiation fluxes that appear in Eqs. (6) through (10) is described in Sections 2.2 and 2.3.

2.2 Discretization of the Governing Equations and Boundary Conditions

The governing equations were discretized and solved using the finite volume method and the SIMPLER algorithm [21]. The boundary condition of Eq. (6) is approximated by incorporating the net radiation flux into a source term, S_{rad}, in Eq. (5) for only the solid control volumes immediately adjacent to the interface between the fluid and the conducting solid. The boundary condition at the exposed adiabatic boundaries of the domain is accommodated by iteratively adjusting local wall temperatures until Eq. (10) is satisfied.

In order to calculate the local radiation heat fluxes, each exposed control surface of the computational domain is assumed to be isothermal at its respective solid control volume temperature, and characterized by uniform radiosity and irradiation. The exposed control surfaces are also assumed to be opaque, diffuse, and gray. With these assumptions, the net radiation heat flux leaving an arbitrary exposed control surface i, is calculated as

$$q_i'' = \frac{E_{bi} - J_i}{(1-\varepsilon_i)/\varepsilon_i}, \tag{11}$$

where E_{bi} is the emissive power for a black surface ($E_{bi} = \sigma T_i^4$), and J_i is the radiosity of surface *i*. The net radiation heat flux leaving control surface *i* is also equal to the sum of the radiation heat fluxes from surface *i* to all other control surfaces

$$\frac{E_{bi} - J_i}{(1-\varepsilon_i)/\varepsilon_i} = \sum_{j=1}^{N} F_{ij}(J_i - J_j) \tag{12}$$

where F_{ij} is the view factor from arbitrary surface *i* to arbitrary surface *j*, and *N* is the number of control surfaces involved in the radiative exchange. Equations (11) and (12) are derived in [22]. The system of equations involving the unknown radiosities is solved using Gaussian elimination based upon most-recently calculated values of the control surface temperatures.

Because of the highly coupled nature of the conduction, convection, and radiation heat transfer processes, an iterative solution is required. First, Eqs. (1-5) are solved without considering radiation (S_{rad} = 0). Then, the radiosities and radiation heat fluxes are calculated using Eqs. (11) and (12), and these fluxes are subsequently used to re-calculate the temperature distribution within the entire computational domain. The governing equations are solved repeatedly until the maximum relative change in local temperature is less than 10^{-8}.

2.3 Evaluation of View Factors

The view factors, F_{ij}, in Eq. (12) are calculated using Hottel's crossed string method [23]. For simple, two-dimensional geometries, view factor evaluation using this method is a straightforward process. In this study, however, some of the view factors can be affected as the solid shape evolves since the two arbitrary control surfaces *i* and *j* can become partially (or completely) obstructed from one another by the opaque

solid. This situation is handled as follows. First, numerical values of the view factors are found for each solid shape using an initial calculation that is subsequently adjusted in order to satisfy the conservation of radiation energy requirement [24, 25]. The calculation and adjustment scheme is: (*i*) a ray is projected from the center of surface *i* to the center of surface *j*, as shown in Fig. 2a, (*ii*) if the ray passes through any solid control volume, the view factor is set to zero. Otherwise, the view factor is calculated as if surfaces *i* and *j* were unobstructed, (*iii*) after all initial values of the view factors are obtained, the summation rule [22] is applied with $sum_i = \sum_{j=1}^{N} F_{ij}$ calculated for all of the exposed control surfaces, (*iv*) if $sum_i \neq 1$, two additional rays are projected from the edges of surface *i* to the edges of surface *j* (Figs. 2b and 2c) to determine if the view between *i* and *j* is partially obstructed, (*v*) if $sum_i < 1$, all view factors from surface *i* that were incorrectly set to zero, such as for the situation shown in Fig. 2b, are increased from zero to a value that forces $sum_i = 1$, (*vi*) if $sum_i > 1$, all view factors that were overpredicted, such as for the scenario shown in Fig. 2c, are decreased by an equal amount that ensures $sum_i = 1$. Throughout the view factor evaluation process, the reciprocity relation [22] is used. That is, if F_{ji} has already been calculated or corrected, then $F_{ij} = F_{ji}\frac{A_j}{A_i}$.

2.4 Evolutionary Design Method

A flow chart of the evolutionary design method used to adjust the solid shape, which is described in detail elsewhere [20], is shown in Fig. 3. First, an initial solid material distribution is specified, and the governing equations of Section 2.2 are solved. Then, the local heat fluxes along the solid-fluid interface are calculated. At the location of the largest surface heat flux, the adjacent solid control volume is converted to fluid. Concurrently, at the location of the smallest surface heat flux, the adjacent fluid control volume is converted to solid. Constraints are imposed on which control volumes can switch phase, in order to prevent the evolution of implausible solid shapes that are described in the literature [2] such as detached (*i.e.* floating) solid control volumes or checkerboard patterns indicative of porous solids which are not of interest here. For example, if converting the solid control volume adjacent to the largest surface

heat flux to fluid would lead to a detached solid shape, then that control volume would not be selected for adjustment. The control volume at the location of the next largest surface heat flux would be selected instead. As noted previously, the control volumes at the location of the applied heat rate, q', are forced to remain solid. The criterion to stop the iterative design for all cases is the onset of oscillation of the solid between two distinct shapes which marks the end of the solid shape evolution. Note that the amount of solid (and air) remains constant even though the solid changes shape.

3. Results

The physical model and evolutionary design method are applied to a range of domain sizes and emissivity values in order to investigate the influence of convection and radiation on the predicted optimal solid shape and overall thermal resistance between the bottom center of the domain boundary and the top, isothermal boundary of the domain, $R_t' = [T(H/2\,,0) - T_o]/q'$. For all cases, the thermophysical properties are associated with air and aluminum (k_f = 0.0257 W/m·K; k_s = 237 W/m·K; ρ_f = 1.205 kg/m^3; μ_f = 1.511×10^{-5} Pa·s; $c_{p,f}$ = 1005 J/kg·K; $c_{p,s}$ = 910 J/kg·K, β_f = 3.43×10^{-3} K^{-1}). The non-adiabatic boundary conditions are q' = 0.05 W/m and T_o = 300 K. In all cases, b/H=1/30 and R/H = 1/6. A 60 × 60 uniform control volume distribution is deemed to be adequate for the results reported here (see the Appendix).

3.1 The Influence of Radiation on the Thermal Behavior Associated with the Initial Geometry

To demonstrate the influence of radiation heat transfer on the free convection (and conduction) heat transfer processes, predicted streamline and temperature distributions associated with the initial solid geometry are provided in Fig. 4. As evident and as reported previously [20], flow conditions, which may be described in terms of a modified Rayleigh number, $Ra^* = g\beta q' H^4/bk_f\nu\alpha = 199{,}100$ are highly asymmetrical when radiation is neglected ($\varepsilon = 0$, Fig. 4a), as may be expected considering the proclivity of the fluid flow to exhibit strong asymmetry in situations involving natural

convection in enclosures characterized by horizontally-symmetric thermal boundary conditions [26].

The asymmetry of the fluid velocity (and temperature) distribution becomes less pronounced as radiation is included in the analysis, with nearly fully symmetric convective (and thermal) conditions established for $\varepsilon = 0.2$ (Fig. 4c). The establishment of nearly symmetrical conditions in Fig. 4c is attributed to two related effects. First, in the absence of fluid flow and for the boundary conditions of the problem, radiation heat transfer would induce perfectly symmetric thermal behavior. Second, even with fluid flow accounted for, the increasing strength of radiation (higher emissivities) will decrease the temperatures and temperature differences throughout the domain. These decreased temperature differences will, in turn, reduce buoyancy forces in the fluid which are ultimately responsible for the asymmetry noted in Figs. 4a and 4b. Maximum temperatures occur at $x = H/2$, $y = 0$ for all cases reported in Fig. 4 and are 301.42, 301.29, and 301.07 K, for $\varepsilon =$ 0, 0.1, and 0.2, respectively. As expected, the thermal resistance across the cavity is reduced as the emissivity increases with $R_t' = 28.46$, 25.86, and 21.46 K·m/W for Figs. 4a, 4b, and 4c, respectively.

Because of the important influence of the surface emissivity on local fluid velocities (and temperatures) associated with the initial semi-circular solid shape, it is expected that the solid shapes corresponding to minimized thermal resistances will also be influenced by radiation heat transfer. The relative strength of radiation to that of convection heat transfer increases as ε increases, or as Ra^* decreases, and the influence of both ε and H (*i.e.* Ra^*) on the optimal solid shapes are reported in the next section.

3.2 Thermal Performance, Solid Shapes, and Streamlines

The design method of Fig. 3 is now applied with Ra^* = 199,100, 671,800, and 1,592,000 (H = 30, 45, and 60 mm) and with emissivity values ranging from 0 to 0.5 in increments of 0.05 (11 distinct emissivity values representing a total of 33 individual conditions) to illustrate the sensitivity of both the final solid

shape and the overall thermal resistance to convection and radiation conditions. Predictions for higher emissivity values are not reported since, as will become evident, although the overall thermal resistance decreases with increasing emissivity as expected, the influence of radiation on the final solid shape becomes weak as the emissivity approaches 0.5.

Predicted thermal resistances, obtained as the design iterations proceed for each Ra^*, ε case, are provided in Figs. 5-7. Note that the results shown in Figs. 5-7 correspond to a total of 3406 individual simulations involving the conjugate conduction, convection, radiation analysis described in Section 2. For each Ra^*, ε case the design iterations continue until a final geometry is achieved. However (as evident for the $Ra^* = 199{,}100$, $\varepsilon = 0.05$ case of Fig. 5, for example) the final geometry (at design iteration 197) does not necessarily correspond to the geometry associated with the minimum thermal resistance, which is identified with a solid data symbol (at design iteration 160).

As expected, and as confirmed in Figs. 5-7, thermal resistances decrease as either Ra^* or ε increase. In general, but not in all cases, the final geometry is reached with fewer design iterations as the emissivity is increased, reflecting the behavior described in Section 3.1 in which the inclusion of radiation heat transfer leads to more symmetric behavior and, as will become evident, a tendency for the solid to remain in the vicinity of the vertical centerline of the enclosure. Note that asymptotic convergence to a geometry that provides the minimum overall thermal resistance is not expected since, because of the conjugate conduction - free convection - radiation nature of the problem, it is not certain that a single adjustment of the solid shape during its evolution will lead to a reduced resistance relative to that of its previous shape.

The solid shapes and streamlines in the fluid associated with the minimum thermal resistances (solid data points) of Figs. 5-7 are reported in Figs. 8-10. As shown in Fig. 8 for $Ra^* = 199{,}100$ ($H = 30$ mm), the solid shape associated with the minimum thermal resistance with $\varepsilon = 0$ has shifted to the bottom left of the enclosure. For this case, the solid is initially guided to the left by the highly asymmetric nature of the fluid velocity and temperature distributions of the first design iteration (the initial solid distribution, Fig.

4a). The solid shape evolution for the $\varepsilon = 0$ case of Figs. 5 and 8 is reported and discussed in detail elsewhere [20]. As also evident in Fig. 8, as the influence of the radiation heat transfer (ε) is increased the final solid shape shifts from its initial position to a lesser degree. As might be expected from inspection of Figs. 4c and 5, the solid shape is nearly unchanged from its initial semi-circular geometry when $\varepsilon \geq 0.2$.

As Ra^* increases (Figs. 6 and 7), the strength of convection increases relative to that of radiation, and the optimal solid shapes are not achieved as early in the design iteration process as in Fig. 5. For the $Ra^* = 671{,}800$ case ($H = 45$ mm), the solid shape associated with $\varepsilon = 0$ again resides at the bottom left of the enclosure (Fig. 9), similar to the situation reported in Fig. 8 for the $Ra^* = 199{,}100$ case. Because the relative strength of convection associated with Fig. 9 exceeds that of Fig. 8, flow conditions display some asymmetry, even at $\varepsilon = 0.5$, although the solid remains concentrated near the centerline of the cavity. Similar behavior is noted in Fig. 10 for the $Ra^* = 1{,}592{,}000$ ($H = 60$ mm) case. The flow remains highly asymmetric, even for $\varepsilon = 0.5$. The evolution of the solid shape for $\varepsilon = 0$ associated with Fig. 10 is discussed in detail elsewhere [20]. Temperature distributions associated with the extreme emissivity cases of Figs. 8-10 are reported in Fig. 11.

3.3 Impact of the Iterative Design Process on Overall Thermal Resistance and Final Solid Shape

As evident in Figs.5-7 there is, in general and as expected, a significant reduction in the overall thermal resistance as the strength of radiation (ε) or convection (Ra^*) is increased. For all of the cases considered here, there is a less significant, but still measurable change in the thermal resistance that is attributed to the reconfiguration of the solid during the design process of Fig. 3. As evident in the predictions discussed in Section 3.2, inclusion of radiation heat transfer leads to fluid flow (and temperature) distributions that exhibit more horizontal symmetry, with the final solid shape tending to remain in the vicinity of the vertical centerline of the enclosure as the strength of radiation increases.

For each *Ra**, the influence of radiation on the overall thermal resistance may be quantified by defining the relative difference between (*i*) the minimum thermal resistance for a particular emissivity value and (*ii*) the minimum thermal resistance of the $\varepsilon = 0$ case as

$$\hat{R}'_{t,1} = \frac{R'_{t,min}(\varepsilon=0) - R'_{t,min}}{R'_{t,min}(\varepsilon=0)} \tag{13}$$

and the results are shown in Fig. 12. In general, $\hat{R}'_{t,1}$ increases as ε increases. An exception to this trend occurs for the *Ra** = 199,100 (*H* = 30 mm) case where $\hat{R}'_{t,1}$ decreases as ε is increased from 0.1 to 0.15 which corresponds to a severe change in the final solid shape (Fig. 8). The dependence of the final solid shape on the emissivity is less pronounced for the *H* = 45 and 60 mm cases (Figs. 9 and 10) and reductions in $\hat{R}'_{t,1}$ as the emissivity is increased are not evident in Fig. 12.

The relative reduction in the thermal resistance due specifically to the reconfiguration of the solid from (*i*) the value associated with the initial semicircular solid, $R'_{t,i}$ to (*ii*) the value associated with the optimal solid $R'_{t,min}$ may be defined for each *Ra**, ε case as

$$\hat{R}'_{t,2} = \frac{R'_{t,i} - R'_{t,min}}{R'_{t,i}} \tag{14}$$

The relative thermal resistance reductions associated with the minimal thermal resistance cases of Figs. 5-7 are reported in Fig. 13. As evident in the figure and as expected from the discussion of Figs. 5-10, the smallest relative reductions are associated with the least severe deviations of the solid shape from the initial semi-circular configuration ($\varepsilon \gtrsim 0.15$ for *Ra** = 199,100, $\varepsilon \gtrsim 0.35$ for *Ra** = 671,800 and 1,592,000). In contrast, the most significant relative reductions occur at lower emissivity values ($\varepsilon \lesssim 0.15$ for *Ra** = 199,100, $\varepsilon \lesssim 0.35$ for *Ra** = 671,800 and 1,592,000) that correspond to the greater reconfigurations of the solid. Hence, for the cases considered here, inclusion of even modest amounts of

surface radiation in the heat transfer analysis significantly affects the natural convection (and conduction) processes, the optimal solid shape, and the overall thermal resistance values. It is also evident from Fig. 13 that for the cases with significant solid reconfiguration ($\varepsilon \lesssim 0.15$ for $Ra^* = 199{,}100$, $\varepsilon \lesssim 0.35$ for $Ra^* = 671{,}800$ and $1{,}592{,}000$), the cases with a smaller relative strength of convection experience a larger reduction in thermal resistance due to reconfiguration of the solid ($\hat{R}'_{t,2}$).

4. Conclusions and Recommendations

An evolutionary design method has been applied over a range of convection and radiation conditions in order to observe and quantify the influence of surface radiation on the predicted final solid shape and the corresponding overall thermal resistance across the domain. For the problem considered here, it was found that increasing the strength of radiation (ε) promotes temperature and fluid flow distributions that exhibit greater symmetry about the centerline of the domain, and thus a more symmetric optimal solid shape. The influence of radiation was quantified by introducing two parameters which quantify the relative reduction in thermal resistance in response to (*i*) increases in the surface emissivity ($\hat{R}'_{t,1}$) and (*ii*) reconfiguration of the solid ($\hat{R}'_{t,2}$). Because (*i*) the initial placement of the solid is symmetric about the centerline of the domain and (*ii*) increasing the strength of radiation leads to a solid shape that is symmetric about the centerline of the domain, the cases characterized by higher emissivity did not evolve much from their initial semicircular shape, and thus experienced small reductions in the thermal resistance.

Based on the findings of this study, recommendations for future research include: (*i*) incorporation of the effects of radiation in other, more complex and more accurate TO design methodologies, and (*ii*) experimental validation of the thermal performance of heat sink designs generated by methods which include the effects of radiation and natural convection. Incorporating radiation into more complex TO methods presents several challenges and may be prohibitively computationally expensive; to this end, it would be beneficial to develop simplified numerical models that include radiation transfer such as done in

the past for natural convection problems [17]. Finally, many of the heat sink (and other solid) designs identified through application of TO would require advanced manufacturing methods to realize, such as additive manufacturing. In turn, the specific additive manufacturing technique used would affect both the physical and thermophysical properties of the solid (*e.g.*, surface roughness, effective thermal conductivity, and surface emissivity) perhaps necessitating the incorporation of new sub-models that relate (*i*) the dependence of important physical and thermophysical properties to (*ii*) the manufacturing technique, into the entire TO design process.

Acknowledgment

The authors acknowledge Dr. Hamidreza Shabgard of the University of Oklahoma for his assistance and advice. The first author acknowledges support from the University of Kansas by way of the School of Engineering Dean's First Year Fellowship.

Nomenclature

A	area of control surface (m)
b	width of applied heat rate (m)
c_p	specific heat (J/kg·K)
E_b	black body emissive power (W/m^2)
F	view factor
g	gravitational acceleration (m/s^2)
H	domain length (m)
J	radiosity (W/m^2)
k	thermal conductivity (W/m·K)
Nu	Nusselt number
p	pressure (Pa)
q'	heat rate per unit length (W/m)
q''	heat flux (W/m^2)

Ra^* modified Rayleigh number

R_t' thermal resistance (K·m/W)

$\hat{R}'_{t,1}$ reduction in thermal resistance due to increasing emissivity

$\hat{R}'_{t,2}$ reduction in thermal resistance due to reconfiguration of the solid

S source term (W/m^3)

T temperature (K)

T_o reference temperature (K)

u x-velocity (m/s)

v y-velocity (m/s)

x, y coordinate directions

Greek Symbols

α thermal diffusivity (m^2/s)

β coefficient of thermal expansion (K^{-1})

ε emissivity

μ dynamic viscosity (Pa·s)

ρ density (kg/m^3)

Subscripts

conv convection

f fluid

max maximum

min minimum

rad radiation

s solid

Appendix

The numerical methods associated with the conduction and free convection components of the model were validated as described in detail elsewhere [20]. The detailed radiation modeling was validated as follows. First, in order to ascertain the accuracy of the view factor and radiation heat flux calculations when obstruction of individual radiation surfaces occur due to intervening solids, the pure radiation problem of [27], described in Fig. 14, was considered. All surfaces are isothermal and experience blackbody radiation exchange. The left boundary is at a uniform temperature of 320 K while the other boundaries and the central body are held at 300 K. Local radiation heat fluxes around the interior enclosure surfaces are shown in Fig. 15, where ζ is the distance from the bottom left of the domain measured in the clockwise direction. The predictions of the present study are in excellent agreement with the predictions of the reference.

Next, the model predictions involving combined free convection and blackbody radiation exchange were compared to the results reported in [28] in which an air-filled square cavity consists of adiabatic top and bottom surfaces, and isothermal side walls. Average convection Nusselt numbers, average radiation Nusselt numbers, and total average Nusselt number predicted with the current model are all within 1 percent of the reference values when a 60 × 60 uniform mesh is used.

The third verification exercise was to determine the sensitivity of the final solid shape and thermal performance to the grid size. The evolutionary design method was exercised for the Ra^* = 199,100 (H = 30 mm), ε = 0.15 case using uniform control volume distributions of 20 × 20, 40 × 40, and 60 × 60. The final solid shapes and streamlines corresponding to each mesh size are shown in Fig. 16. The thermal resistances associated with Figs. 16a-16c are $R_t' =$ 24.11, 23.90, and 23.66 K·m/W respectively. Because (*i*) there is only a modest change in both the solid shape and thermal resistance as the mesh size is increased from 40 × 40 to 60 × 60, and (*ii*) considering the significant total computational time required to generate Figs. 5-7, a 60 × 60 mesh was used in this study. To further justify the mesh size, simulations were performed using the initial geometry of Fig. 4c (H = 30 mm, ε = 0.2), and the final geometry of Fig.

9 (H = 30 mm, ε = 0.2) with a 120 × 120 grid. For either geometry, the overall thermal resistance changed by less than two percent relative to the predictions associated with the 60 × 60 grid.

The final validation compares the predictions of the detailed model to those generated by an approximate, analytical model for the situation involving the initial, semicircular solid and stagnant air. The approximate model is based on multiple simplifying assumptions including: (*i*) the exposed semicircular top of the solid is isothermal (*ii*) the adiabatic walls of the enclosure are also reradiating [22], and (*iii*) all exposed surfaces experience uniform irradiation, radiosity, and temperature [22]. With these assumptions, an approximate, thermal resistance model [22] can be developed that consists of one resistance (based on the conduction shape factor [22] for the semicircular solid) that acts in series with second and third resistances that are in parallel. The second resistance is based on the conduction shape factor for the stagnant air [29] while the third resistance is based on a three-surface enclosure radiation analysis involving one reradiating surface [22]. Maximum solid temperatures (at the location where the heat rate is applied) generated by the approximate and numerical models for the H = 45 mm, ε = 0.5 case are $T_{max} - T_o$ = 0.66 K and 0.53 K, respectively. As the emissivity is reduced to ε = 0.25, maximum temperatures increase to $T_{max} - T_o$ = 0.99 K and 0.80 K, for the two models. For the case of no radiation transfer, ε = 0, $T_{max} - T_o$ = 1.91 K for both the approximate and detailed numerical models. As evident, the trends involving the maximum temperatures are as expected, and the relatively good agreement between the predictions of the approximate and detailed models implies that the values of the overall thermal resistances reported in this study are of the correct order of magnitude. To lend insight to the coupled nature of the problem, the thermal resistance values for the semicircular solid of the approximate model is 0.0031 W·m/K. The conduction resistance of the stagnant air of the approximate model (which will be slightly larger than the convection resistance of the detailed model) is 38.4 W·m/K. Finally, the radiation resistances are ∞, 41.0, and 20.1 W·m/K for the ε = 0, 0.25, and 0.50 cases of the approximate model. As evident, the radiation and conduction resistances associated with the air are of similar magnitude for the two cases involving radiation, illustrating the coupled nature of the heat transfer processes.

References

[1] Bar-Cohen, A., 1979, "Fin Thickness for an Optimized Natural Convection Array of Rectangular Fins," ASME J. Heat Trans., **101**, pp. 564-566. https://doi.org/10.1115/1.3451032

[2] Bendsøe, M.P., and Sigmund, O., 2003, Topology Optimization: Theory, Methods, and Applications, Springer, Berlin. https://doi.org/10.1007/978-3-662-05086-6

[3] Li, Q., Steven, G.P., Xie, Y.M., and Querin, O.M., 2004, "Evolutionary Topology Optimization for Temperature Reduction of Heat Conducting Fields," Int. J. Heat Mass Trans., **47**, pp. 5071-5083. https://doi.org/10.1016/j.ijheatmasstransfer.2004.06.010

[4] Gersborg-Hansen, A., Bendsøe, M.P., and Sigmund, O., 2006, "Topology Optimization of Heat Conduction Problems Using the Finite Volume Method," Struct. Multidiscip. O., **31**, pp. 251-259. https://doi.org/10.1007/s00158-005-0584-3

[5] Gao, T., Zhang, W.H., Zhu, J.H., Xu, Y.J., and Bassir, D.H., 2008, "Topology Optimization of Heat Conduction Problem Involving Design-Dependent Heat Load Effect," Finite Elem. Anal. Des., **44**, pp. 805-813. https://doi.org/10.1016/j.finel.2008.06.001

[6] Marck, G., Nemer, M., Harion, J.L., Russeil, S., and Bougeard, D., 2012, "Topology Optimization Using the SIMP Method for Multiobjective Problems," Numer. Heat Trans., B, **61**, pp. 439-470. https://doi.org/10.1080/10407790.2012.687979

[7] Dirker, J., and Meyer, J.P., 2013, "Topology Optimization for an Internal Heat-Conduction Cooling Scheme in a Square Domain for High Heat Flux Applications," ASME J. Heat Trans., **135**, p. 111010. https://doi.org/10.1115/1.4024615

[8] Xia, Q., Shi, T., and Xia, L., 2018, "Topology Optimization for Heat Conduction by Combining Level Set Method and BESO Method," Int. J. Heat Mass Trans., **127**, pp. 200-209. https://doi.org/10.1016/j.ijheatmasstransfer.2018.08.036

[9] Yin, L., and Ananthasuresh, G., 2002, "A Novel Topology Design Scheme for the Multi-Physics Problems of Electro-Thermally Actuated Compliant Micromechanisms," Sens. Actuators, A, **97-98**, pp. 599-609. https://doi.org/10.1016/S0924-4247(01)00853-6

[10] Bruns, T.E., 2007, "Topology Optimization of Convection-Dominated, Steady-State Heat Transfer Problems," Int. J. Heat Mass Trans., **50**, pp. 2859-2873. https://doi.org/10.1016/j.ijheatmasstransfer.2007.01.039

[11] Ahn, S.H., and Cho, S., 2010, "Level Set-Based Topological Shape Optimization of Heat Conduction Problems Considering Design-Dependent Convection Boundary," Numer. Heat Trans., B, **58**, pp. 304-322. https://doi.org/10.1080/10407790.2010.522869

[12] Yoon, G.H., 2010, "Topological Design of Heat Dissipating Structure with Forced Convective Heat Transfer," J. Mech. Sci. Technol., **24**, pp. 1225-1233. https://doi.org/10.1007/s12206-010-0328-1

[13] Koga, A.A., Lopes, E.C.C., Nova, H.F.V., de Lima, C.R., and Silva, E.C.N., 2013, "Development of Heat Sink Device by Using Topology Optimization," Int. J. Heat Mass Trans., **64,** pp. 759-772. https://doi.org/10.1016/j.ijheatmasstransfer.2013.05.007

[14] Alexandersen, J., Aage, N., Andreasen, C.S., and Sigmund, O., 2014, "Topology Optimisation for Natural Convection Problems," Int. J. Numer. Methods Fluids, **76**, pp. 699-721. https://doi.org/10.1002/fld.3954

[15] Alexandersen, J., Sigmund, O., and Aage, N., 2016, "Large Scale Three-Dimensional Topology Optimisation of Heat Sinks Cooled by Natural Convection," Int. J. Heat Mass Trans., **100**, pp. 876-891. https://doi.org/10.1016/j.ijheatmasstransfer.2016.05.013

[16] Alexandersen, J., Sigmund, O., Meyer, K.E., and Lazarov, B.S., 2018, "Design of Passive Coolers for Light-Emitting Diode Lamps Using Topology Optimisation," Int. J. Heat Mass Transf., **122**, pp. 138-149. https://doi.org/10.1016/j.ijheatmasstransfer.2018.01.103

[17] Asmussen, J., Alexandersen, J., Sigmund, O., and Andreasen, C.S., 2019, "A 'Poor Man's' Approach to Topology Optimization of Natural Convection Problems," Struct. Multidiscip. O., **59**, pp. 1105-1124. https://doi.org/10.1007/s00158-019-02215-9

[18] Lei, T., Alexandersen, J., Lazarov, B., Wang, F., Haertel, J., De Angelis, S., Sanna, S., Sigmund, O., and Engelbrecht, K., 2018, "Investment Casting and Experimental Testing of Heat Sinks Designed by Topology Optimization," Int. J. Heat Mass Trans., **127**, pp. 396-412. https://doi.org/10.1016/j.ijheatmasstransfer.2018.07.060

[19] Castro, D.A., Kiyono, C.Y., and Silva, E.C.N., 2015, "Design of Radiative Enclosures by Using Topology Optimization," Int. J. Heat Mass Trans., **88**, pp. 880-890. https://doi.org/10.1016/j.ijheatmasstransfer.2015.04.077

[20] Sevart, C.D., and Bergman, T.L., 2019, "An Iterative Design Method to Reduce the Overall Thermal Resistance in a Conjugate Conduction-Free Convection Configuration," Front. Heat Mass Trans., **13** 10 pages. https://doi.org/10.5098/hmt.13.18

[21] Patankar, S.V., 1980, *Numerical Heat Transfer and Fluid Flow*, McGraw-Hill, NY.

[22] Bergman, T.L., and Lavine, A.S., 2017, *Fundamentals of Heat and Mass Transfer*, John Wiley and Sons, NJ.

[23] Hottel, H. C., 1954, "Radiant Heat Transmission", Heat Transmission, McAdams, W. H., ed., McGraw-Hill, NY.

[24] Emery, A.F., Johansson, O., Lobo, M. and Abrous, A., 1991 "A Comparative-Study of Methods for Computing the Diffuse-Radiation Viewfactors for Complex Structures," ASME J. Heat Trans., **113**, pp. 413-412. https://doi.org/10.1115/1.2910577

[25] Eftychiou, M.A., Bergman, T.L., and Masada, G.Y., 1993, "A Detailed Thermal Model of the Infrared Reflow Soldering Process," ASME J. Electron. Packaging, **115**, pp 55-62. https://doi.org/10.1115/1.2909302

[26] Holtzman, G.A., Hill, R.W., and K.S. Ball, 2000, "Laminar Natural Convection in Isosceles Triangular Enclosures Heated from Below and Symmetrically Cooled from Above," ASME J. Heat Trans., **122**, pp. 485-491. https://doi.org/10.1115/1.1288707

[27] Rowley, J.C. and Payne, J.B., 1964, "Steady State Temperature Solution for a Heat Generating Circular Cylinder Cooled by a Ring of Holes," ASME J. Heat Tran., 86, pp. 531-536. https://doi.org/10.1115/1.3688737

[28] Chai, J.C., Lee, H.S., and Patankar, S.V., 1994, "Treatment of Irregular Geometries Using a Cartesian Coordinates Finite-Volume Radiation Heat Transfer Procedure," Numer. Heat Trans., B, **26**, pp. 225-235. https://doi.org/10.1080/10407799408914927

[29] Akiyama, M., and Chong, Q.P., 1997, "Numerical Analysis of Natural Convection with Surface Radiation in a Square Enclosure," Numer. Heat Transf., A, **32**, pp. 419-433. https://doi.org/10.1080/10407789708913899

Figures

Parameter	Value
H (mm)	30, 45, 60
R (mm)	5, 7.5, 10
b (mm)	1, 1.5, 2

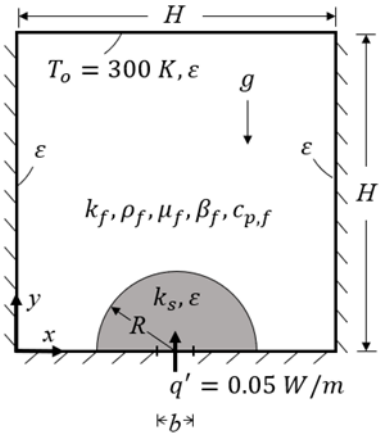

Fig. 1 The computational domain including thermal boundary conditions, thermophysical properties, and the initial solid shape.

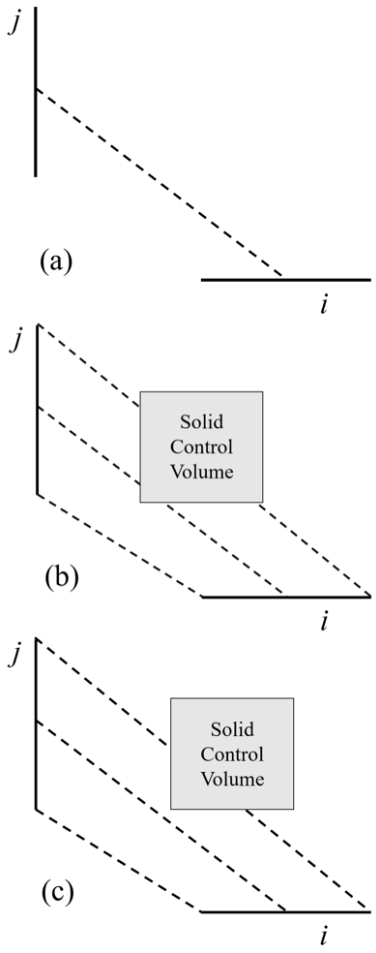

Fig. 2 View factor calculation and adjustment scheme: (a) a ray projected from the center of control surface *i* to the center of control surface *j*, (b) partially obstructed case where the view factor would initially be set to zero, then increased in value when corrected to conserve radiation energy, (c) partially obstructed view factor that is initially overpredicted, then decreased when corrected to conserve radiation energy.

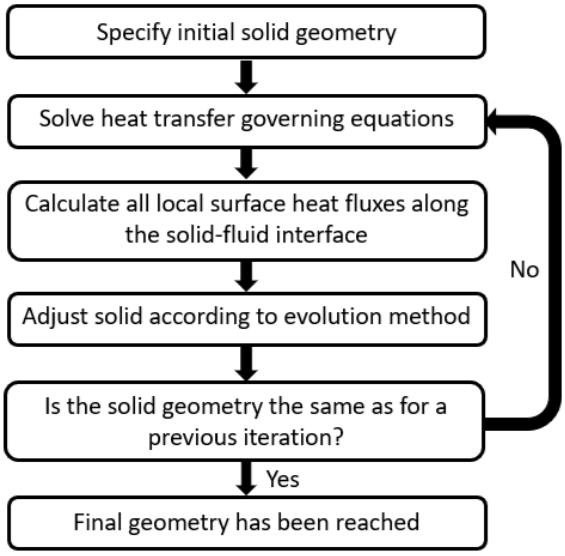

Fig. 3 Flow chart of the iterative design method.

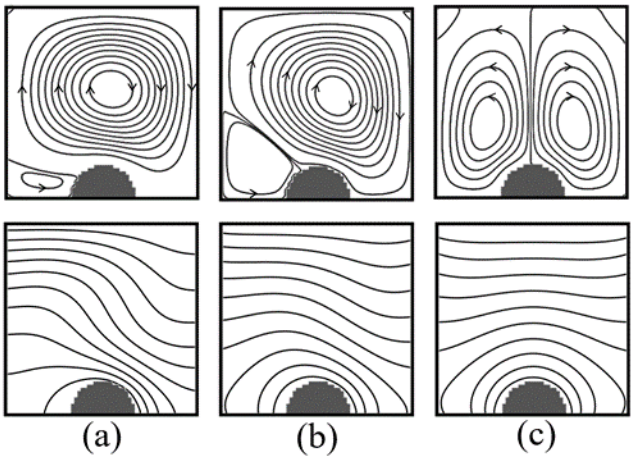

Fig.4 Streamlines (top) and temperature distributions (bottom) associated with H = 30 mm and the initial semicircular geometry (R/H = 1/6, b/H = 1/30, Ra^* = 199,100). (a) ε = 0, (b) ε = 0.1, (c) ε = 0.2. Temperature distributions are generated by plotting 12 evenly spaced isothermal contours between and including the maximum and minimum temperature.

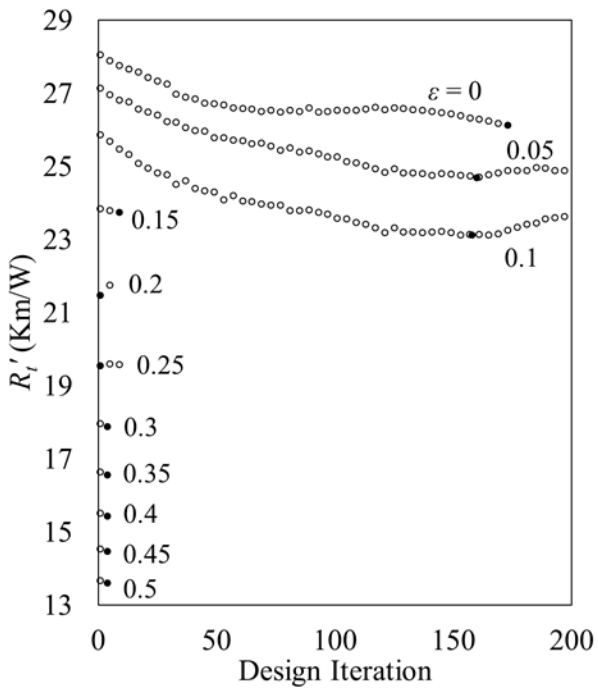

Fig. 5 Evolution history of thermal resistance for H = 30 mm, Ra^* = 199,100. Solid markers designate minimum thermal resistance.

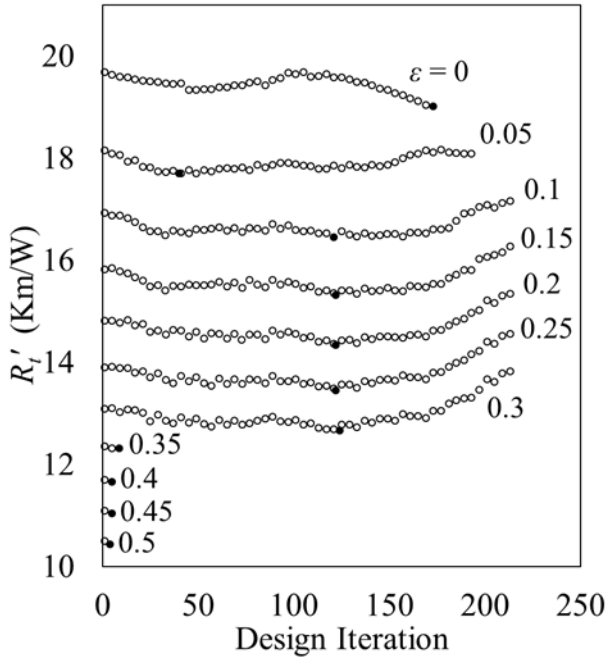

Fig. 6 Evolution history of thermal resistance for H = 45 mm, Ra^* = 671,800. Solid markers designate minimum thermal resistance.

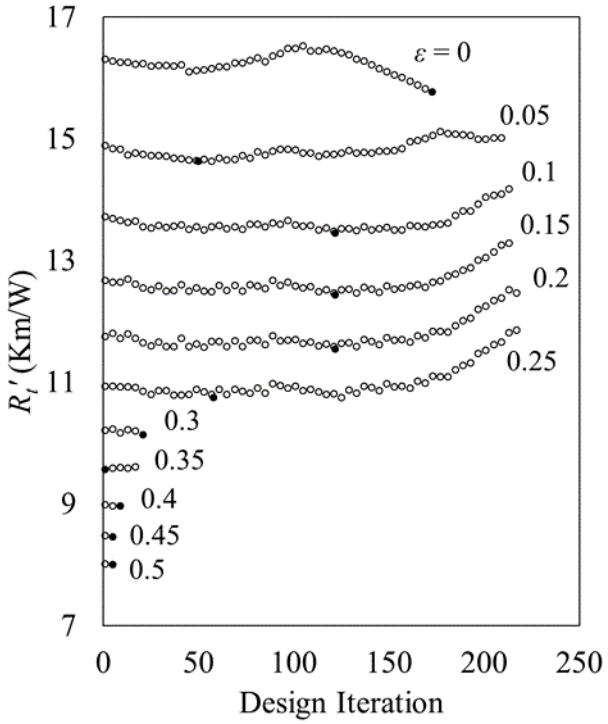

Fig. 7 Evolution history of thermal resistance for H = 60 mm, Ra^* = 1,592,000. Solid markers designate minimum thermal resistance.

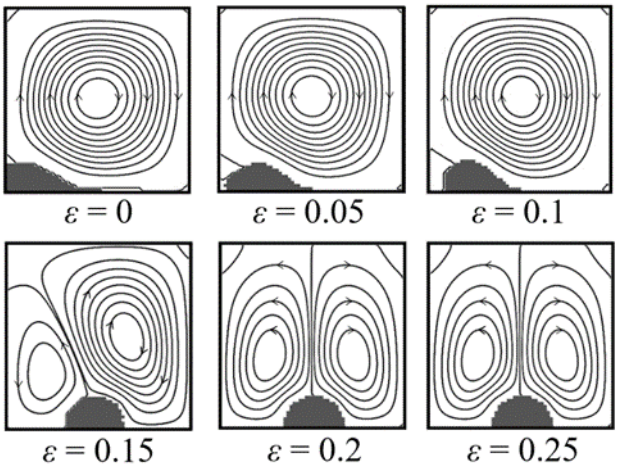

Fig. 8 Solid shape and streamlines associated with the minimum thermal resistances (solid markers in Fig. 5) of the H = 30 mm, Ra^* = 199,100 cases. Qualitatively, the streamlines of the $\varepsilon \geq 0.30$ cases are similar to those of the $\varepsilon = 0.25$ case. Note the sharp transition in the fluid flow and the solid shape at $\varepsilon \approx 0.2$.

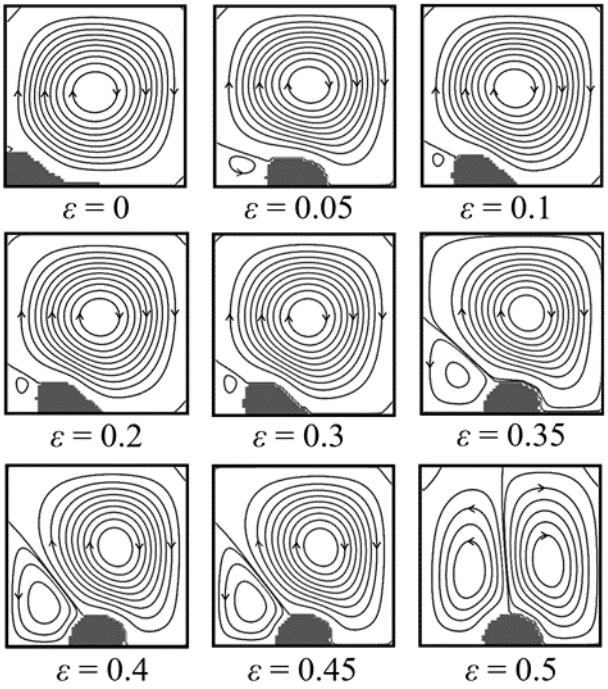

Fig. 9 Solid shape and streamlines associated with the minimum thermal resistances (solid markers in Fig. 6) of the H = 45 mm, Ra^* = 671,800 cases.

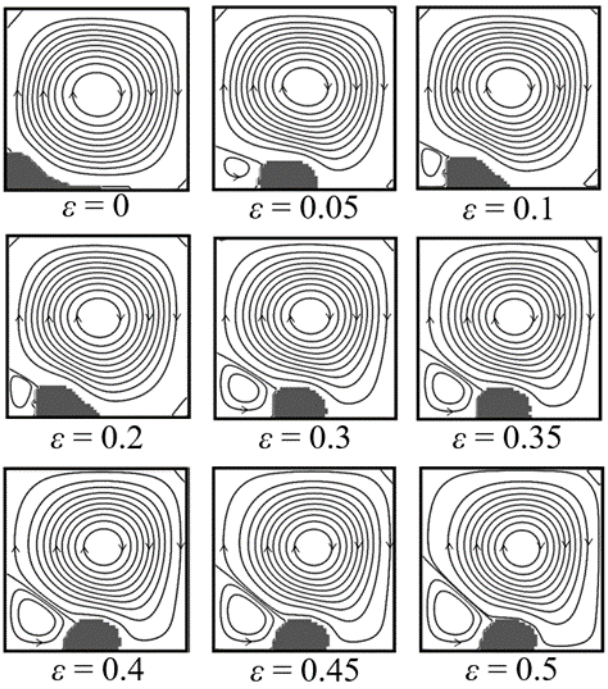

Fig. 10 Solid shape and streamlines associated with the minimum thermal resistances (solid markers in Fig. 7) of the H = 60 mm, Ra^* = 1,592,000 cases.

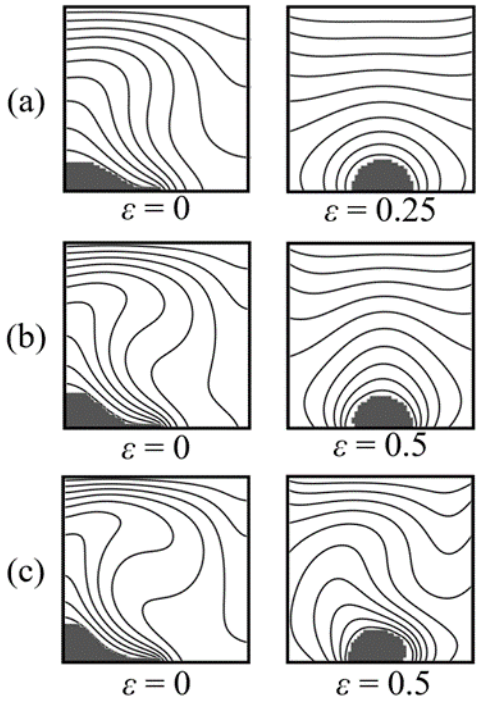

Fig. 11 Temperature distributions associated with the final solid shape for the case of the emissivity shown and (a) H = 30 mm, (b) H = 45 mm, (c) H = 60 mm. Temperature distributions are generated by plotting 12 evenly spaced isothermal contours between and including the maximum and minimum temperature.

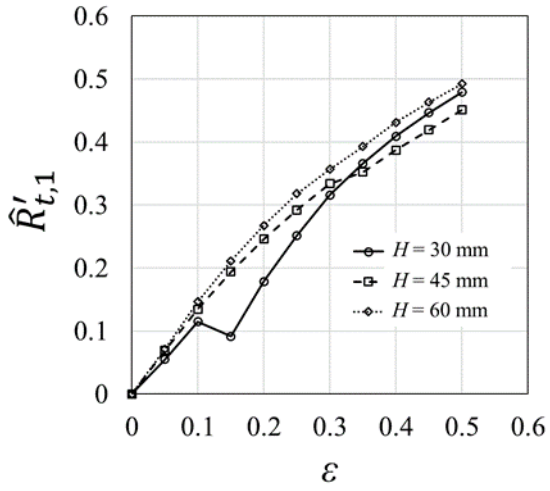

Fig. 12 Relative reduction between ε = 0 minimum thermal resistance and minimum thermal resistance of each emissivity value.

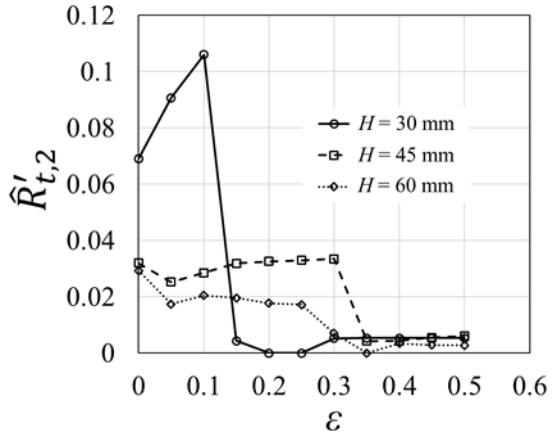

Fig. 13 Relative reduction between initial and minimum thermal resistance.

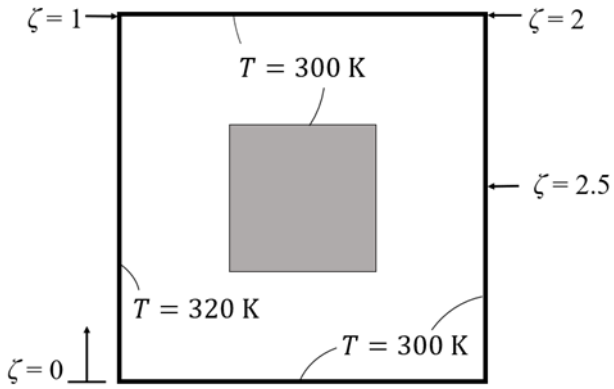

Fig. 14 Pure radiation example from [27].

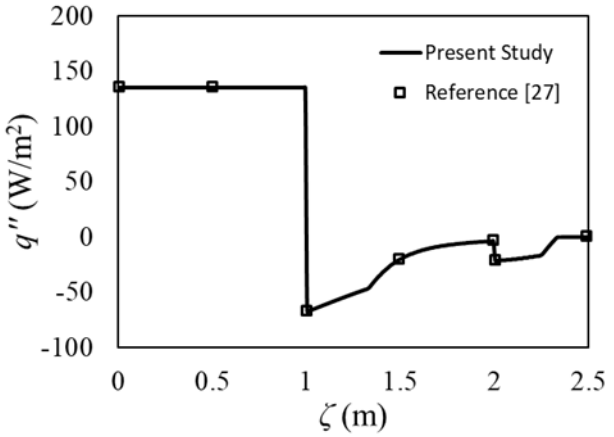

Fig. 15 Predicated local radiation heat fluxes along the interior boundary of the enclosure shown in Fig. 13 (solid line). Data points are from Fig. 8 of [28].

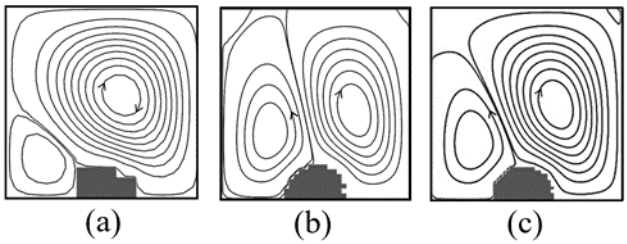

Fig. 16 Final solid shapes and streamlines for the Ra^* = 199,100 (H = 30 mm), ε = 0.15 case with a mesh size of (a) 20 × 20, (b) 40 × 40, and (c) 60 × 60.

Paper P3

Title:

Growth-Based Design of a Conducting Solid Cooled by Conjugate Gas Conduction and Surface Radiation

Authors:

Chadwick D. Sevart

Theodore L. Bergman

Journal:

Proceedings of the ASME, IMECE

Proceedings of the ASME 2022
International Mechanical Engineering Congress and Exposition
IMECE2022
October 30 – November 3, 2022, Columbus, Ohio

IMECE2022-95178

GROWTH-BASED DESIGN OF A CONDUCTING SOLID COOLED BY CONJUGATE GAS CONDUCTION AND SURFACE RADIATION

Chadwick D. Sevart, Theodore L. Bergman

University of Kansas, Lawrence, KS, USA

ABSTRACT

A solid growth model (SGM) is developed to identify desirable configurations of a conducting solid that is cooled by conduction through a stagnant gas and surface radiation. Thermal performance is quantified by the overall thermal resistance, as well as a figure of merit that rewards both (i) low thermal resistance and (ii) use of a small amount of solid. The results show that radiation affects both the evolution of the solid shape and the thermal performance. Predictions of the novel SGM are compared to those of a formal topology optimization (TO) method, which incorporates the effects of radiation after the solid shape is determined by considering conduction only. While application of the TO method yields a lower overall thermal resistance when a high solid thermal conductivity is considered, the SGM leads to better thermal performance when a low solid thermal conductivity is involved.

Keywords: Topology Optimization, Solid Growth Model, Conjugate Heat Transfer, Radiation

NOMENCLATURE

A	area
b	width of applied heat rate surface
E_b	blackbody emissive power
F_{ij}	view factor between surfaces i and j
F	figure of merit
H	domain dimension
J	radiosity
k	thermal conductivity
k_s^*	dimensionless solid thermal conductivity
n	normal direction
NS	number of exposed control surfaces
q'	heat rate per unit length
q''	heat flux
R'	thermal resistance
S	source term
T	temperature
T_o	boundary temperature
x, y	coordinate directions

Greek Symbols

ε	emissivity
σ	Stefan-Boltzmann constant

Subscripts

cond	conduction

f	fluid
i,j	surfaces *i* and *j*
max	maximum
rad	radiation
s	solid
tot	total

1. INTRODUCTION

Optimal thermal performance is sought in a wide range of thermal management applications. In the context of heat sink design, for example, a typical goal is to identify solid shapes that provide low overall thermal resistances while using a minimal amount of solid material. Methods used for heat sink design include but are not limited to: (*i*) standard techniques as described in heat transfer texts [1, 2], (*ii*) size and shape optimization [3, 4], (*iii*) constructal theory [5, 6], and (*iv*) topology optimization (TO) [7–10]. A drawback of the first three methods is that the basic geometric features (or sub-features) of the object are often specified *a priori*. For example, Bar-Cohen [3] utilized shape optimization to design finned heat sinks cooled by natural convection by varying the fin width and thickness, as well as by adjusting the spacing between fins.

Several methods are not restricted by specified geometrical features. For example, TO techniques are based on solid material redistribution methodologies that ultimately define the desired solid shape. With TO, the solid density distribution within a computational domain is adjusted according to an optimization scheme that uses predicted state variables such as temperature or fluid velocity [7]. TO applied to pure heat conduction problems is relatively straightforward, has been investigated extensively, and has been extended to the development of new TO methodologies such as those capable of incorporating local volumetric thermal generation rates [11] or solving multi-objective problems by minimizing both the average temperature and the temperature variance [12].

Multiple heat transfer modes must be considered for most practical applications. Relative to TO, a common situation involves the design of heat sinks subject to conjugate conduction-forced convection effects [8, 9, 13–16]. For example, TO was used to create a 3D, jet-impingement-air-cooled heat sink of complex shape [15] that was subsequently fabricated using additive manufacturing and tested experimentally. Several TO studies have addressed problems involving conjugate conduction-free convection [17–21]. For example, TO has been used to design 3D heat sinks for light emitting diodes that are cooled by natural convection [20]. Subsequently [21], the heat sinks of [20] were fabricated and tested experimentally to validate the predicted temperature distributions.

As is well known, surface radiation heat transfer can contribute significantly to thermal performance, and is dependent on the geometry of the radiating solid [22, 23]. In terms of size and shape optimization, several studies have considered radiation effects [25–29]. In contrast, the number of studies that have applied design approaches (similar to TO) to problems involving radiation is limited. Castro *et al.* [30] considered a cubic radiative enclosure to determine the optimal distribution of reflective material inside the enclosure to (*i*) minimize the net heat flux, (*ii*) maximize the net heat flux or (*iii*) minimize the temperature at a specified location. In [31], a particle swarm TO method was used to determine the optimal locations of low-temperature panels inside a room for purposes of developing a radiant cooling system. A weighted objective function involving both (*i*) occupant thermal comfort and (*ii*) energy consumption was utilized.

The preceding examples [30, 31] did not embody the more difficult problem of determining the most desirable *shapes* of solids cooled by radiation to maximize thermal performance. To address this challenge, Sevart and Bergman [32] developed an evolutionary design method (EDM) for determining desirable geometries of conducting solids cooled by conjugate radiation and natural convection. The EDM begins with fixed amounts of solid and fluid in a computational domain, after which the solid (and fluid) distribution was redistributed in an evolutionary manner based upon simple design rules. It was found that radiation had a substantial effect on the temperature distributions and fluid flow, and therefore on the predicted solid shapes.

The application of formal TO methods to determine optimal solid shapes for heat transfer problems involving surface radiation is challenging. This is because formal TO methods usually begin with a uniform, low-density solid distribution throughout the computational domain that is devoid of any surfaces, making evaluation of surface radiation heat transfer problematic. Recently however, Wang *et al*. [33], used TO to optimize the microscale features of a thin film including the effects of radiation. The conduction and radiation processes were only weakly coupled. It was found that the optimized structure was dependent on the interplay between conduction, convection, and radiation.

To the authors' knowledge, a situation that has not been investigated is the determination of the geometry of a solid with no pre-specified geometric features or sub-features, which is cooled by strongly coupled conduction and surface-to-surface radiation. Such a situation might be of interest for low pressure or aerospace applications when

natural convection is negligible. In this study, therefore, a solid growth method (SGM), distinct from the EDM of [32], is presented and used to determine conducting solid configurations (shapes) that are cooled by conjugate radiation heat exchange and conduction in an adjacent fluid. To quantify thermal performance, a figure of merit that rewards both (*i*) low thermal resistance and (*ii*) use of a small amount of solid material is introduced. The influence of the solid emissivity and solid thermal conductivity on the predicted solid configurations and thermal performance is investigated. SGM predictions are compared to radiation-conduction predictions for solid configurations that are determined by TO. Note that surface radiation is neglected during the TO simulation that determines the final solid shape because, as discussed previously, TO methodologies begin by assuming a uniform, low-density solid distribution within the computational domain that is devoid of surfaces, precluding inclusion of surface radiation transfer in the TO process. At any rate, once the final TO solid shape is found, radiation is then included to determine the conjugate conduction-radiation thermal processes associated with the TO-determined solid geometry.

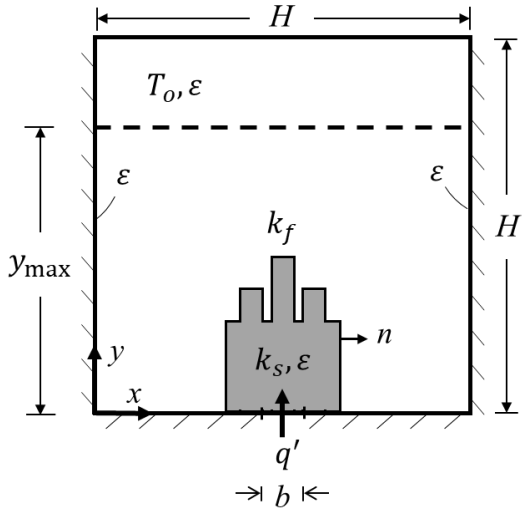

FIGURE 1: Physical domain and boundary conditions.

2. PHYSICAL SYSTEM AND SOLID GROWTH MODEL (SGM)

The physical system is described in Fig. 1. A 2D, $H \times H$ domain consists of a contiguous solid of thermal conductivity k_s and a radiatively transparent, stagnant fluid of thermal conductivity, $k_f < k_s$. Heat transfer occurs by conduction in the solid, conduction in the fluid, and surface-to-surface radiation transfer in response to an imposed heat rate per unit depth, q', that is applied over a section of the bottom boundary of width b, centered about $x = H/2$. The top boundary of the domain is isothermal at T_o, while the remaining portions of the domain boundaries are assumed to be adiabatic. The objective is to predict 2D solid shapes that pose low overall thermal resistances between the location of the applied heating and the top, cold boundary of the domain. The value of the overall resistance is determined by a complex interplay between the coupled conduction processes in the solid and the fluid which are, in turn, both coupled to the surface-to-surface thermal radiation processes occurring at all solid boundaries, including at the surface of a potentially complex solid-fluid structure whose geometry is initially unknown.

The SGM predictions begin with minimal solid in the domain (the initial solid occupies only two computational control volumes; Section 2.2) placed adjacent to the heated portion of the bottom boundary. Local temperatures and heat fluxes are then determined by solving the appropriate discretized forms (Sections 2.2 and 2.3) of the governing equations (Section 2.1), after which an incremental amount of solid is added to the domain according to the growth methodology described in Section 2.4. The governing equations are solved again, and an incremental amount of solid is again added. The process of repeatedly adding solid to (and subtracting fluid from) the domain and re-solving the governing equations continues, resulting in the gradual growth of the solid at the expense of the fluid. The solid is restricted to the portion of the domain below the horizontal dashed line of Fig. 1 located at $y = y_{\max}$. No restrictions are placed on the extent of the solid in the x-direction.

2.1 Governing Equations and Boundary Conditions

The temperature distribution in the entire solid-fluid domain is determined by solving the appropriate heat diffusion equations for the fluid and the solid. Steady state conditions are assumed, and all thermophysical properties

are taken to be constant for each case considered. The fluid does not participate in the radiation transfer and is assumed to be stationary with the effects of free convection being negligible. All exposed surfaces are assumed to be diffuse and gray, and characterized by the same emissivity, ε. With these assumptions, the heat diffusion equation applied to either the solid or the fluid is

$$\frac{\partial}{\partial x}\left(k\frac{\partial T}{\partial x}\right)+\frac{\partial}{\partial y}\left(k\frac{\partial T}{\partial y}\right)=0 \tag{1}$$

where $k = k_s$ in the solid, and $k = k_f$ in the fluid. The top boundary is isothermal, that is, $T(x, y = H) = T_o$. The applied heat rate at the bottom of the domain is uniform over the width b, so that

$$-k_s\frac{\partial T}{\partial y}\Big|_{y=0}=q'/b \tag{2}$$

Locally at the complex solid surface, the conduction heat flux in the opaque solid to the solid-fluid interface is equal to the conduction heat flux in the fluid from the solid-fluid interface plus the radiation heat flux from the exposed solid surface,

$$-k_s\frac{\partial T}{\partial n}=-k_f\frac{\partial T}{\partial n}+q''_{\mathrm{rad}} \tag{3}$$

where n is the outward normal direction at any location along the solid-fluid interface. From Eq. (3) it is evident that at the exposed adiabatic boundaries,

$$-k_f\frac{\partial T}{\partial n}+q''_{\mathrm{rad}}=0 \tag{4}$$

As the opaque solid grows and evolves in shape, it may come into contact with an adiabatic boundary, preventing radiation heat transfer from that section of the boundary. In such a situation,

$$-k_s\frac{\partial T}{\partial n}=0 \tag{5}$$

2.2 Discretization and Boundary Conditions

Equation (1) is solved using the finite volume method, with all interfacial effective thermal conductivities calculated using the harmonic mean approach [34]. The radiation heat flux appearing in Eq. (3) is treated by introducing an equivalent local source term in the solid, S_{rad}, into the discretized form of Eq. (1). The values of the source terms are determined from the radiation heat transfer analysis of Section 2.3. At the exposed adiabatic control surfaces, radiation is accounted for by employing a constant temperature boundary condition, utilizing an appropriate boundary temperature so that that Eq. (4) is satisfied.

Because the radiation and conduction processes are tightly coupled, an iterative solution is implemented for each individual solid geometry as follows: (*i*) local temperatures are determined by solving Eq. (1) without inclusion of the effects of radiation, ($S_{\mathrm{rad}} = 0$) then (*ii*) local surface radiation heat fluxes are calculated as will be described in Section 2.3. Next, (*iii*) S_{rad} is calculated, and the local temperatures of the exposed adiabatic boundaries are set so that they satisfy Eq. (4) after which (*iv*) Eq. (1) is solved again using the updated source terms and boundary conditions. Steps (*ii*) - (*iv*) are repeated until the change in each control volume temperature is less than 10^{-8} K. Because the ultimate size and shape of the solid is unknown, the computational domain is populated by control volumes of uniform dimension.

2.3 Calculation of Radiation Heat Fluxes

To calculate values of S_{rad}, each exposed control surface is assumed to be isothermal at the temperature of the corresponding solid control volume. As noted previously, all surfaces are assumed to be opaque, diffuse, and gray and of the same emissivity, ε. With these assumptions, the net radiation heat flux from an arbitrary solid-fluid control surface, i, is given as [1]

$$q''_i=\frac{E_{bi}-J_i}{(1-\varepsilon_i)/\varepsilon_i} \tag{6}$$

where $E_{bi} = \sigma T_i^4$ is the blackbody emissive power and J_i is the radiosity. The net radiation heat flux, q_i'', is also equal to the summation of radiation heat fluxes from surface *i* to each of the other *j* exposed control surfaces which leads to [1]

$$\frac{E_{bi}-J_i}{(1-\varepsilon_i)/\varepsilon_i} = \sum_{j=1}^{NS} F_{ij}(J_i - J_j) \tag{7}$$

where *NS* is the number of exposed control surfaces, and F_{ij} is the view factor between surface *i* and surface *j*. The method used to calculate the view factors accounts for the total or partial obstruction of individual *i* - *j* control surfaces by an intervening solid, as discussed in detail in [32]. In short, all view factors are first approximated without accounting for any obstruction(s), using Hottel's crossed string method [35]. The view factors are then adjusted, accounting for obstructions between individual control surfaces, in order to satisfy the summation rule and the reciprocity relation [1]. Equations (6) and (7) are solved using Gaussian elimination.

2.4 Growth Methodology

As discussed previously, there is initially only a small amount of solid (two computational control volumes) placed at the bottom center of the domain. After the first calculation of $T(x, y)$, additional solid (two control volumes) is added to the existing solid, at the location(s) of the maximum local heat flux from the solid to the solid-fluid interface. Two control volumes of solid are added at each step (one control volume somewhere in the left half of the domain and the second additional control volume at the corresponding location in the right half of the domain) to take advantage of the symmetry of the problem and reduce computational expense. The SGM is based on the premise that solid material should be added to the location(s) where it is already most effective in reducing the overall thermal resistance. The SGM is therefore heuristic. Nonetheless, it will become evident that the SGM is capable of producing solid distributions that compete well with solid distributions determined by TO in terms of their overall thermal performances.

In short, the steps of the SGM are: (*i*) local temperatures and surface radiation heat rates are calculated iteratively as described in Sections 2.2 and 2.3, (*ii*) the net heat fluxes (including both radiation and conduction) from each exposed control surface of the solid are determined, then (*iii*) the two fluid control volumes (one in the LHS of the domain and the other in the RHS) adjacent to the location of the maximum heat flux are switched to solid, resulting in the incremental growth of the solid at the expense of the fluid. Steps (*i*) - (*iii*) are repeated, allowing the solid shape to evolve in the growth domain, $0 \le x \le H,\ 0 \le y \le y_{\max}$.

3. TO MODEL AND DOMAIN MAPPING

The predictions of the SGM are compared to those of a formal TO model which neglects the effects of radiation in the generation of its solid configurations. The TO model utilized in this study incorporates the Solid Isotropic Material with Penalization method [7] for the material distribution and the Method of Moving Asymptotes [36] for the optimization algorithm. The objective function is the thermal resistance, and the adjoint method is employed for calculating sensitivities of the objective function on the solid distribution [12]. A penalization parameter of $P = 4$ is used for all TO cases.

Because the TO method utilizes a continuous description of the solid distribution (solid fractions of individual control volumes are not limited to values of 0 or 1), distinct solid-fluid interfaces are absent, making evaluation of surface radiation heat transfer problematic. By using an identical computational mesh in both the SGM and TO models, a discrete description (control volume solid fractions are either 0 or 1) of the solid and fluid distributions is generated using the optimal continuous solid distribution of the TO solution. The mapping of the continuous solid distribution to the discrete solid distribution utilizes the conservation of mass principle. Specifically, the control volumes of the continuous solid distribution are sequentially converted to pure solid starting with the highest density control volumes. The conversion process continues until the total mass represented by the discrete solid distribution equals the total mass of the continuous solid distribution. The remaining non-solid control volumes are converted to fluid. The resulting discrete solid-fluid distribution is then used to solve the coupled radiation-conduction problem as detailed in Sections 2.1 – 2.3. It is noted that the continuous and discrete solid distributions appear nearly identical in shape and size when inspected visually.

4. RESULTS AND DISCUSSION

The SGM was used to predict the evolution of a conducting solid, characterized by a range of thermal conductivities and emissivities, into a computational domain otherwise occupied by a stationary, radiatively transparent fluid. To quantify the thermal performance of the various solid-fluid configurations, the overall thermal

resistance between (*i*) the location $x = H/2$, $y = 0$ and (*ii*) the top cold, isothermal boundary, $R'_{\text{tot}} \equiv [T(H/2,0) - T_o]/q'$, is determined. The effects of conduction are isolated by calculation of the conduction resistance, R'_{cond}, of the various configurations by setting $\varepsilon = 0$. A figure of merit is introduced, $F \equiv (R'_{\text{tot}} \cdot k_f \cdot A_s/A_{\text{tot}})^{-1}$, where A_s is the cross-sectional area of the solid and A_{tot} is the area of the entire $H \times H$ computational domain. As evident, the figure of merit rewards (*i*) low thermal resistances and (*ii*) use of small amounts of solid.

In all cases the fluid is taken to be air, $k_f = 0.0257$ W/m·K, and the non-adiabatic boundary conditions are $q' = 1$ W/m and $T_o = 750$ K. The dimension of the square computational domain is arbitrarily chosen to be $H = 0.06$ m with $b/H = 1/90$ and $y_{\max}/H = 177/180$. The value of b/H and $y_{\max}/H$ are related to the use of a 180 × 180, uniform control volume computational domain that is employed for all of the simulations. As noted in Section 2, the growth history begins with a small amount of solid that is seeded in the computational domain. All interior surfaces of the domain are specified to be of the same emissivity as that of the solid.

4.1 Evolution of R'_{tot} and F

A dimensionless solid thermal conductivity is introduced as $k_s^* \equiv k_s/(240\ \text{W/m} \cdot \text{K})$ so that $k_s^* = 1$ corresponds to pure aluminum. The SGM is exercised with emissivity values of $\varepsilon = 0$ and 0.4 for $k_s^* = 1$ and 0.1, resulting in four physical condition cases.

The evolution history of the overall thermal resistance (R'_{tot}) and the figure of merit (F) for the four cases are shown in Figs. 2a and 2b, respectively. The TO method is applied at four arbitrarily selected A_s values for the four physical cases. The figure of merit and overall thermal resistance associated with the TO-determined solid configurations are represented by the isolated, filled data points in Fig. 2.

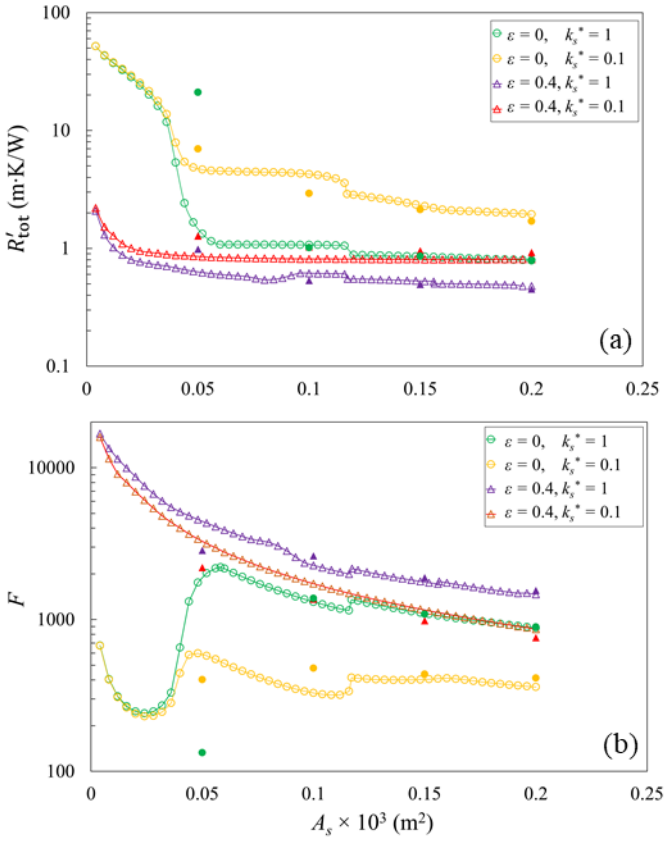

FIGURE 2: Evolution history of (a) overall thermal resistance and (b) figure of merit predicted by the SGM. Filled data points correspond to TO predictions.

For each SGM case, the largest R'_{tot} values correspond to the least amount of solid (Fig. 2a, $A_s \to 0$) and, initially, the smaller resistances are associated with the higher emissivity surfaces, as expected. Also, the figure of merit is larger for the higher emissivity cases (Fig. 2b, $A_s \to 0$) since the solid is initially of the same shape for all cases. For

the $\varepsilon = 0$ cases, R'_{tot} decreases as the solid expands (Fig. 2a), while F experiences a more complex evolution (Fig. 2b). In contrast, the two $\varepsilon = 0.4$ cases have A_s regions in which R'_{tot} increases as solid material is added to the domain. As will be discussed later, this is a result of solid material blocking radiation transfer between locations of high temperature and the colder isothermal boundary. The $\varepsilon = 0.4$, $k_s^* = 1$ case has a slightly more complex evolution of R'_{tot} and F compared to the $\varepsilon = 0.4$, $k_s^* = 0.1$ case. The TO predictions will be discussed in Section 4.2.3 and 4.3.3.

4.2 SGM and TO Predictions, $k_s^* = 1$

Representative solid configurations and temperature distributions associated with $k_s^* = 1$ are shown in Figs. 3 and 4, respectively. There are three solid geometries shown for each A_s value in Fig. 3 corresponding to (*i*) the SGM with $\varepsilon = 0$ (Figs. 3a - 3d), (*ii*) the SGM with $\varepsilon = 0.4$ (Figs. 3e - 3h), and (*iii*) the TO discrete solid distribution with $\varepsilon = 0$ and 0.4 (Figs. 3i - 3l). (Because the discrete TO geometries are derived from a pure conduction analysis, the TO solid shapes are the same for $\varepsilon = 0$ and $\varepsilon = 0.4$.) Also note that the temperature distributions shown for the TO solids in Fig. 4 are associated with $\varepsilon = 0.4$. One-hundred, uniformly spaced isotherms are included in the figures. The overall thermal resistance (R'_{tot}), thermal resistance due to conduction (R'_{cond}), and figure of merit for the solid configurations of Fig. 3 are reported in Table 1.

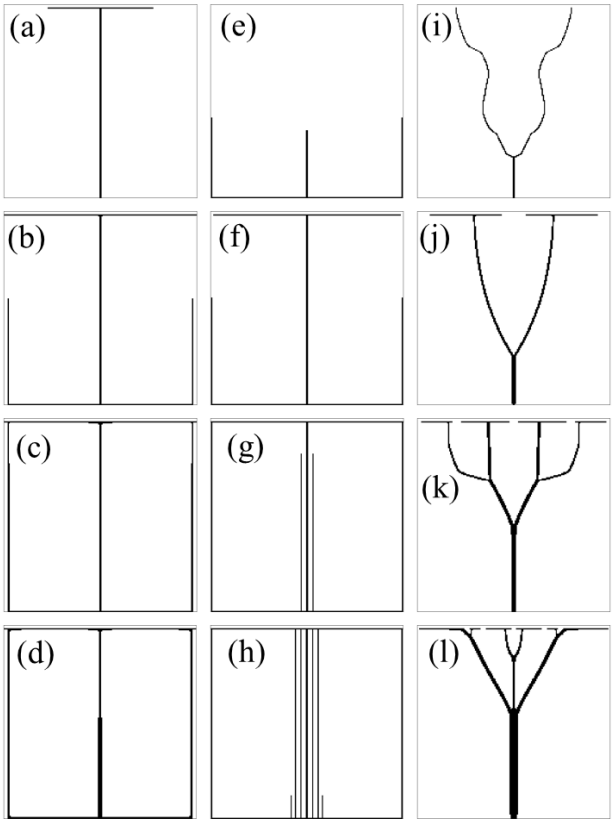

FIGURE 3: Solid configurations for $k_s^* = 1$ and the SGM with $\varepsilon = 0$ (left), the SGM with $\varepsilon = 0.4$ (middle), and TO (right) for $A_s \times 10^3 = 0.05$ m^2 (a, e, i), 0.1 m^2 (b, f, j), 0.15 m^2 (c, g, k), and 0.2 m^2 (d, h, l).

4.2.1 Solid Growth Method, $k_s^* = 1$, $\varepsilon = 0$

For the $\varepsilon = 0$ case (Figs. 3a - 3d and 4a - 4d), the solid initially grows upward from the location of the applied heat rate, toward the isothermal top boundary. After the vertical solid column reaches the top of the growth domain ($y = y_{\max}$) at $A_s \times 10^3 = 0.039$ m^2, it bifurcates and grows toward the side boundaries, resulting in the T-shaped structure of Fig. 3a. The thin, vertical solid column creates a pathway of high thermal conductivity material that effectively propagates high temperatures upward, as shown by the temperature distribution of Fig. 4a. As the central solid column approaches the top boundary, there is a sharp decrease in R'_{tot} and a steep increase in F (Fig. 2, 0.02 m$^2 \lesssim A_s \times 10^3 \lesssim 0.05$ m^2).

The thin horizontal solid section near the top of the growth domain evident in Fig. 3a continues to expand outward until it reaches the vertical adiabatic boundaries at $A_s \times 10^3 = 0.059\ \mathrm{m}^2$. Subsequently, the location of maximum heat flux shifts to the bottom center of the domain, and the solid begins to grow outward horizontally, taking a new path along the bottom adiabatic boundary. After the solid in the vicinity of $y = 0$ reaches the vertical adiabatic boundaries at $A_s \times 10^3 = 0.079\ \mathrm{m}^2$, it turns and grows upward, leading to the solid shape shown in Fig. 3b. This addition of solid does little to reduce R'_{tot} and therefore serves to decrease F (Fig. 2, $0.05\ \mathrm{m}^2 \lesssim A_s \times 10^3 \lesssim 0.1\ \mathrm{m}^2$). However, when the vertical solid sections located near the vertical boundaries come into contact with the horizontal solid section at the top of the domain at $A_s \times 10^3 = 0.1165\ \mathrm{m}^2$, there is a sharp decrease in R'_{tot} (Fig. 2a) and a corresponding increase in F (Fig. 2b).

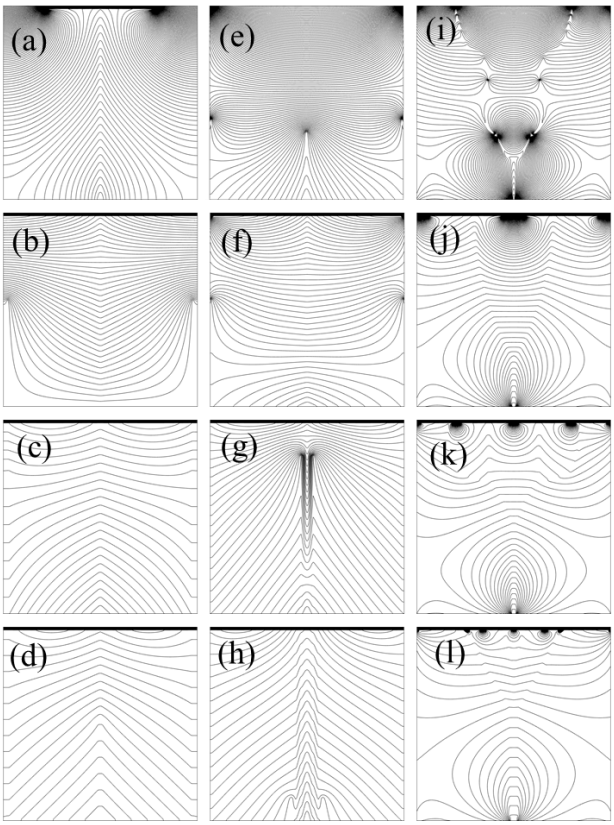

FIGURE 4: Temperature distributions for $k_s^* = 1$ and the SGM with $\varepsilon = 0$ (left), the SGM with $\varepsilon = 0.4$ (middle), and TO (right) for $A_s \times 10^3 = 0.05\ \mathrm{m}^2$ (a, e, i), $0.1\ \mathrm{m}^2$ (b, f, j), $0.15\ \mathrm{m}^2$ (c, g, k), and $0.2\ \mathrm{m}^2$ (d, h, l).

For the remainder of the growth process, solid is added along the three existing vertical columns, increasing their thickness, as shown in Figs. 3c and 3d. This additional solid leads to a slight reduction in R'_{tot}, and a corresponding monotonic reduction in F for $A_s \times 10^3 \gtrsim 0.1165\ \mathrm{m}^2$.

Table 1: Thermal resistances and figures of merit for $k_s^* = 1$.

$A_s \times 10^3$ (m^2)	Method	$R'_{tot}(\frac{m \cdot K}{W})$	$R'_{cond}(\frac{m \cdot K}{W})$	F
0.05	SGM, $\varepsilon = 0$	1.468	1.468	1909
	SGM, $\varepsilon = 0.4$	0.6307	27.72	4442
	TO, $\varepsilon = 0.4$	0.9816	21.12	2854
0.1	SGM, $\varepsilon = 0$	1.071	1.071	1308
	SGM, $\varepsilon = 0.4$	0.6144	1.080	2280
	TO, $\varepsilon = 0.4$	0.5341	1.015	2623
0.15	SGM, $\varepsilon = 0$	0.8514	0.8514	1097
	SGM, $\varepsilon = 0.4$	0.5286	0.8706	1767
	TO, $\varepsilon = 0.4$	0.4946	0.8591	1888
0.2	SGM, $\varepsilon = 0$	0.7935	0.7935	882.7
	SGM, $\varepsilon = 0.4$	0.4777	0.7783	1466
	TO, $\varepsilon = 0.4$	0.4506	0.7821	1554

4.2.2 Solid Growth Method, $k_s^* = 1$, $\varepsilon = 0.4$

In contrast to the $\varepsilon = 0$ case, the solid of the $\varepsilon = 0.4$ case (Figs. 3e - 3h and 4e - 4h) initially grows outward horizontally until it reaches the side adiabatic boundaries at $A_s \times 10^3 = 0.02$ m^2. Subsequently, the solid turns and grows upward along the side boundaries. When the vertical solid sections along the side boundaries reach a height of $y \approx H/3$ at $A_s \times 10^3 = 0.036$ m^2 the location of the maximum heat flux shifts to the bottom center of the domain, and the solid grows upward, leading to the solid configuration shown in Fig. 3e. The growth pathway for $\varepsilon = 0.4$ corresponds to a more gradual reduction in R'_{tot} compared to that of the $\varepsilon = 0$ case (Fig. 2, 0 m^2 $\lesssim A_s \times 10^3 \lesssim$ 0.05 m^2). With the effects of radiation included, the isotherms shown in Fig. 4e, are no longer perpendicular to the adiabatic boundary, as required by Eq. (4). Because all of the solid is located in the bottom half of the domain, heat transfer is dominated by radiation for this solid structure, as noted by the low overall thermal resistance (R'_{tot} = 0.6307 m·K/W) and relatively high conduction resistance (R'_{cond} = 27.72 m·K/W) reported in Table 1.

The vertical section in the middle of the domain continues to grow until it reaches the top of the growth domain at $A_s \times 10^3 = 0.076$ m^2, after which it bifurcates and grows outward horizontally. As the horizontal solid section at the top of the domain continues to grow outward, it serves to decrease the conduction resistance but increasingly shields radiation transfer between high temperature sections at the bottom of the domain and the colder, top isothermal boundary. This shielding effect leads to an increase in the total thermal resistance (Fig. 2a, 0.08 m^2 $\lesssim A_s \times 10^3 \lesssim$ 0.1 m^2). Although the $\varepsilon = 0$ and $\varepsilon = 0.4$ cases exhibit different initial growth histories, the two solid structures at $A_s \times 10^3 = 0.1$ m^2 (Figs. 3b and 3f) are nearly identical. The two cases also display similar temperature distributions (Figs. 4b and 4f), but the $\varepsilon = 0$ case has a more uniform temperature distribution in the lower half of the domain. In comparing the thermal resistances of the $\varepsilon = 0.4$ case at $A_s \times 10^3 = 0.05$ m^2 and 0.1 m^2 in Table 1, there is a slight decrease in R'_{tot} (from 0.6307 to 0.6144 m·K/W) but a significant decrease in R'_{cond} (from 27.72 to 1.080 m·K/W).

Beyond $A_s \times 10^3 = 0.1$ m^2, the vertical solid sections near the side boundary grow upward until coming into contact with the top solid section at $A_s \times 10^3 = 0.1165$ m^2, which causes a sharp decrease in R'_{tot} (Fig. 2a) and a corresponding sharp increase in F (Fig. 2b). The remainder of the growth process for the $\varepsilon = 0.4$ case is characterized by the addition of distinct, vertical solid sections that grow from the bottom of the domain to the top, as shown in Figs. 3g and 3h. These solid sections, located near the vertical centerline, effectively propagate high temperatures upward (Figs. 4g and 4h).

4.2.3 Topology Optimization Model, $k_s^* = 1$

The branching tree-like structures obtained by TO (Figs. 3i - 3l) exhibit more complexity than the corresponding solid shapes obtained by SGM (Figs. 3a - 3h). As A_s increases, the TO structures are characterized by thicker solid sections with more branching and additional complexity. The complexity serves to reduce conduction resistance values, but can increase the resistance to radiation transfer across the domain because of the radiation shielding effect. At $A_s \times 10^3 = 0.05$ m^2, (Fig. 3i) the conduction resistance associated with TO (R'_{cond} = 21.12 m·K/W) is bracketed by the conduction resistances associated with either SGM approach (R'_{cond} = 1.468 m·K/W and 27.72 m·K/W). The unexpectedly large R'_{cond} associated with the TO prediction is attributed to the small amount of solid in the domain, and the corresponding thin solid branches of Fig. 3i. This complex TO-derived structure, obtained from the mapping

process of Section 3, is therefore associated with multiple staggered solid-fluid control volumes that serve to artificially increase the computed conduction resistances across the domain. A comparison of the overall resistances at this A_s value shows that the TO structure's overall resistance (R'_{tot} = 0.9816 m·K/W) is similar to the overall resistance of SGM (R'_{tot} = 0.6307 m·K/W).

At $A_s \times 10^3 = 0.1$ m^2, (Fig. 3j) more solid is present relative to the solid of Fig. 3i, the staggering effect that numerically increases conduction resistances is diminished, and the conduction resistance of the TO solid (R'_{cond} = 1.015 m·K/W) is smaller than those of either of the SGM predictions (R'_{cond} = 1.071 and 1.080 m·K/W). The overall resistance of the TO solid (R'_{tot} = 0.5341 m·K/W) is also smaller than that of the SGM predictions (R'_{tot} = 0.6144 m·K/W). As A_s increases ($A_s \times 10^3 = 0.15$ m^2 and 0.2 m^2), the conduction resistances reported in Table 1 for the SGM and TO predictions are similar in value, while the overall resistances associated with the TO approach (R'_{tot} = 0.4946 and 0.4506 m·K/W at $A_s \times 10^3 = 0.15$ m^2 and 0.2 m^2) are incrementally smaller than for either overall resistance associated with the SGM approach (R'_{tot} = 0.5286 m·K/W and 0.4777 m·K/W at $A_s \times 10^3 = 0.15$ m^2 and 0.2 m^2). Based on these limited results, it may be concluded that the TO approach produces more desirable structures to reduce R'_{tot} values and increase the corresponding figures of merit, for situations where sufficient solid is present to minimize numerical effects that artificially increase conduction resistance values.

4.3 SGM and TO Predictions, k_s^* = 0.1

Solid configurations and temperature distributions of the k_s^* = 0.1 cases are reported in Figs. 5 and 6, respectively, at several A_s values. The thermal resistances and figures of merit associated with the solid configurations of Fig. 5 are reported in Table 2.

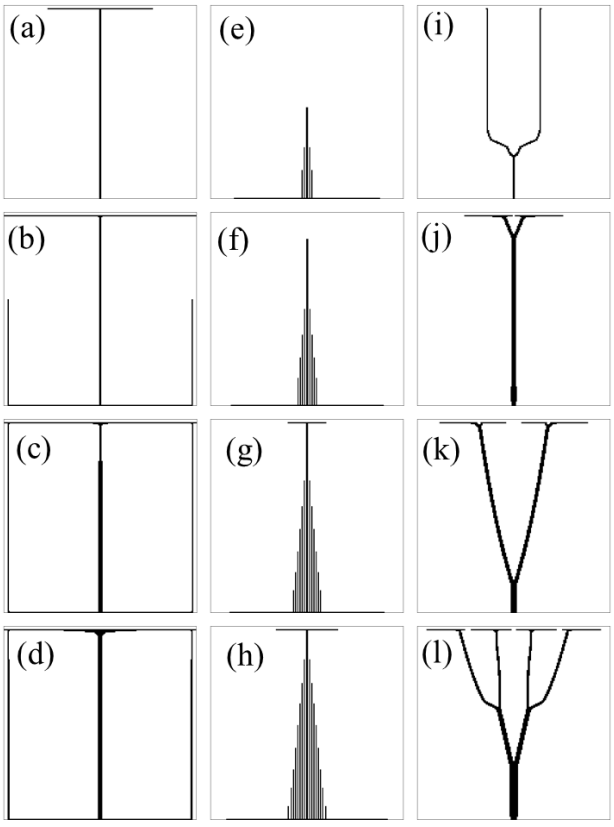

FIGURE 5: Solid configurations for k_s^* = 0.1 and the SGM with ε = 0 (left), the SGM with ε = 0.4 (middle), and TO (right) for $A_s \times 10^3$ = 0.05 m^2 (a, e, i), 0.1 m^2 (b, f, j), 0.15 m^2 (c, g, k), and 0.2 m^2 (d, h, l).

4.3.1 Solid Growth Method, k_s^* = 0.1, ε = 0

The ε = 0 case (Figs. 5a - 5d and 6a - 6d) initially has the same growth path as the k_s^* = 1, ε = 0 case (Figs. 3a - 3d and 4a - 4d) and exhibits a similar evolution of R'_{tot} and F (Fig. 2). The solid configurations of Figs. 5a and 5b are identical to those of Figs. 3a and 3b. The temperature distributions of the k_s^* = 0.1 case (Figs. 6a and 6b) exhibit a

higher concentration of isotherms in the region containing solid relative to the k_s^* = 1 case (Figs. 4a - 4d). The solid evolution for the k_s^* = 0.1, ε = 0 case is slightly different than the k_s^* = 1 case after $A_s \times 10^3 = 0.1165$ m^2 in that more solid is added to the center vertical column relative to the outer columns (Figs. 5c and 5d).

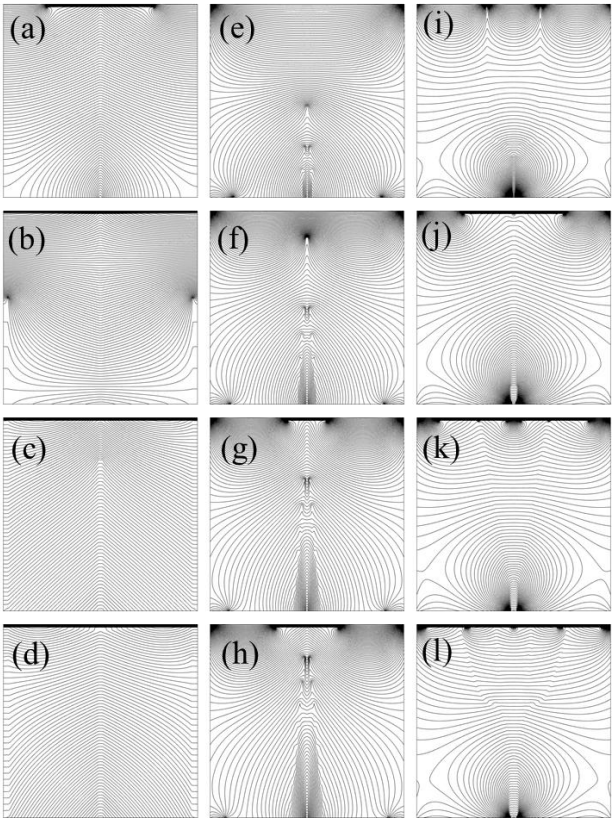

FIGURE 6: Temperature distributions for k_s^* = 0.1 and the SGM with ε = 0 (left), the SGM with ε = 0.4 (middle), and TO (right) for $A_s \times 10^3$ = 0.05 m^2 (a, e, i), 0.1 m^2 (b, f, j), 0.15 m^2 (c, g, k), and 0.2 m^2 (d, h, l).

4.3.2 Solid Growth Method, k_s^* = 0.1, ε = 0.4

The solid evolution of the k_s^* = 0.1, ε = 0.4 case (Figs. 5e - 5h) is remarkably different than that of the other growth method cases. The solid initially grows outward horizontally, but before it reaches the side boundaries, at $A_s \times 10^3 = 0.015$ m^2 the location of maximum heat flux shifts to the bottom center of the domain. Subsequently, the solid grows upward at $x = H/2$ until it reaches $y \approx H/2$. After that, the solid growth is characterized by the nucleation and growth of new solid columns and the extension of existing columns as shown in Figs. 5e and 5f. For $A_s \times 10^3 =$ 0.05 m^2 and 0.1 m^2 (Figs. 5e and 5f) most of the solid is in the lower half of the domain, and there is a large surface area of solid that exchanges thermal radiation with the top isothermal boundary. Both of these characteristics cause the thermal resistance to be dominated by radiation. This is shown by the fact that R'_{cond} (28.78 and 14.44 m·K/W) is significantly larger than R'_{tot} (0.8540 and 0.8134 m·K/W) at $A_s \times 10^3 = 0.05$ m^2 and 0.1 m^2 (Table 2).

Table 2: Thermal resistances and figures of merit associated for $k_s^* = 0.1$.

$A_s \times 10^3$ (m^2)	Method	R'_{tot} ($\frac{m \cdot K}{W}$)	R'_{cond} ($\frac{m \cdot K}{W}$)	F
0.05	SGM, $\varepsilon = 0$	4.742	4.742	590.9
	SGM, $\varepsilon = 0.4$	0.8540	28.78	3281
	TO, $\varepsilon = 0.4$	1.274	6.966	2199
0.1	SGM, $\varepsilon = 0$	4.261	4.261	328.7
	SGM, $\varepsilon = 0.4$	0.8134	14.44	1730
	TO, $\varepsilon = 0.4$	1.029	2.926	1362
0.15	SGM, $\varepsilon = 0$	2.317	2.317	403.1
	SGM, $\varepsilon = 0.4$	0.8063	4.385	1158
	TO, $\varepsilon = 0.4$	0.9504	2.135	982.6
0.2	SGM, $\varepsilon = 0$	1.946	1.946	360
	SGM, $\varepsilon = 0.4$	0.8101	3.448	864.6
	TO, $\varepsilon = 0.4$	0.9226	1.696	759.2

The central solid column eventually reaches the top of the growth domain at $A_s \times 10^3 = 0.115$ m^2 then bifurcates outward horizontally as shown in Fig. 5g. Unlike the $k_s^* = 1$, $\varepsilon = 0.4$ case (Figs. 3e - 3h) the horizontal section of solid at the top of the domain does not immediately extend entirely to the side boundaries. Instead, the solid growth alternates between extending the vertical columns, creating new vertical columns, and gradually extending the horizontal sections at the top and bottom of the domain. This complex solid evolution is reflected in Fig. 5h. Because the top horizontal section of solid in Fig. 5h does not span to width of the domain, such as for the solid configurations of Figs. 3f - 3h, there is less shielding of radiation between the high temperature regions at the bottom of the domain and the colder top boundary. However, there is still some shielding which occurs that increases the thermal resistance due to radiation, which is evidenced by the fact that between $A_s \times 10^3 = 0.15$ m^2 and 0.2 m^2 R'_{cond} decreases from 4.385 to 3.448 m·K/W, but R'_{tot} increases from 0.8063 to 0.8101 m·K/W (Table 2). Even though the solid thermal conductivity is relatively low, the high number of columns allows for high temperatures to propagate upwards as shown by Figs. 6e - 6h.

4.3.3 Topology Optimization Model, $k_s^* = 0.1$

In comparison to the higher thermal conductivity TO case (Figs. 3i - 3l), the TO solid configurations of the $k_s^* = 0.1$ case (Figs. 5i - 5l) are of simpler geometry with less branching and a higher concentration of solid near the vertical centerline. At $A_s \times 10^3 = 0.05$ m^2, (Fig. 5i) the conduction resistance associated with TO (R'_{cond} = 6.966 m·K/W) is bracketed by the conduction resistances associated with either SGM approach (R'_{cond} = 4.742 m·K/W and 28.78 m·K/W). However, for $A_s \times 10^3 = 0.1$ m^2, 0.15 m^2, and 0.2 m^2 (Figs. 5j - 5l) the TO solid structures exhibit a lower R'_{cond} (2.926, 2.135, and 1.696 m·K/W) than the SGM, ε = 0 (4.261, 2.317, and 1.946 m·K/W) and ε = 0.4 (14.44, 4.385, and 3.448 m·K/W) cases. While the conduction thermal resistances of the TO solid structures (Figs. 5i - 5l) are lower than that of the SGM, ε = 0.4 case (Figs. 5e - 5h) for all four A_s values, the total thermal resistances associated with TO (R'_{tot} = 1.274, 1.029, 0.9504, and 0.9226 m·K/W) are higher than that of the growth method (R'_{tot} = 0.8540, 0.8134, 0.8063, and 0.8101 m·K/W) (Table 2). This result shows that the SGM, which incorporates the effects of radiation into the solid evolution, achieves a lower thermal resistance due to radiation and therefore results in a preferred solid configuration when the radiation heat transfer is dominant, such as when a low solid thermal conductivity or low amount of solid is considered.

5. CONCLUSIONS

A solid growth methodology has been developed and used to predict the evolution of thermally-conducting solid configurations that are simultaneously cooled by conduction to a stationary fluid as well as by surface radiation. The methodology was applied to four cases involving solids that have one of two surface emissivities and one of two thermal conductivities. Thermal performance was quantified by evaluating both (*i*) the overall thermal resistance and (*ii*) a figure of merit. It is shown that radiation has a significant influence on the solid shapes and corresponding overall thermal resistances. In general, inclusion of radiation produces solid configurations having vertical columns and thus more surface area of solid that can participate in radiative transfer.

Predictions of the SGM were compared to those of a formal topology optimization method based on the assumption of negligible radiation transfer. In general, for the higher solid thermal conductivity cases the TO method produced solid configurations with lower overall thermal resistances. However, for the lower solid thermal conductivity cases, the SGM that incorporates radiation transfer into the solid evolution predicted solid configurations with lower overall thermal resistances, even though the TO solid structures had lower conduction thermal resistances.

The results of this study suggest that thermal radiation can have a significant influence on solid configurations that will offer desired thermal performance, especially when low thermal conductivity solids are considered. While the heuristic SGM proposed in this study is relatively simple and straightforward, it was able to produce solid shapes having lower overall thermal resistances than those associated with a formal TO method. It is recommended that future research address ways to incorporate the effects of thermal radiation into formal TO approaches.

ACKNOWLEDGEMENTS

The first author acknowledges support from the University of Kansas by way of the School of Engineering Wilburn & Mina Wyatt Memorial Scholarship. The authors also acknowledge Dr. Krister Svanberg for providing the source code for the Method of Moving Asymptotes

REFERENCES

[1] Bergman, T.L., and Lavine, A.S. *Fundamentals of Heat and Mass Transfer, eighth ed*., John Wiley and Sons, Hoboken, (2017).
[2] Kraus, A.D., and Bar-Cohen, A. *Design and Analysis of Heat Sinks, first ed*., John Wiley and Sons, New York, (1995).
[3] Bar-Cohen, A. "Fin thickness for an optimized natural convection array of rectangular fins." *ASME Journal of Heat Transfer* 101 (3) (1979) 564-566. https://doi.org/10.1115/1.3451032
[4] Ahmed, H.E., Salman, B.H., Kherbeet, A.S., and Ahmed, M.I. "Optimization of thermal design of heat sinks: a review." *International Journal of Heat and Mass Transfer* 118 (2018) 129-153. https://doi.org/10.1016 /j.ijheatmasstransfer.2017.10.099
[5] Bejan, A. "Constructal-theory network of conducting paths for cooling a heat generating volume." *International Journal of Heat and Mass Transfer* 40 (4) (1997) 799-816. https://doi.org/10.1016/0017-9310(96)00175-5
[6] Muzychka, Y.S. "Constructal multi-scale design of compact micro-tube heat sinks and heat exchangers." *International Journal of Thermal Sciences* 46 (3) (2007) 245-252. https://doi.org/10.1016/j.ijthermalsci.2006.05.002
[7] Bendsøe, M.P., and Sigmund, O. *Topology Optimization: Theory, Methods, and Applications, second ed*., Springer, Berlin, (2003). https://doi.org/10.1007/978-3-662-05086-6
[8] Yoon, G.H. "Topological design of heat dissipating structure with forced convective heat transfer." *Journal of Mechanical Science and Technology* 24 (6) (2010) 1225-1233. https://doi.org/10.1007/s12206-010-0328-1
[9] Koga, A.A., Lopes, E.C.C., Nova, H.F.V., de Lima, C.R., and Silva, E.C.N. "Development of heat sink device by using topology optimization." *International Journal of Heat and Mass Transfer* 64 **(**2013) 759-772. https://doi.org/10.1016/j.ijheatmasstransfer.2013.05.007
[10] Li, Q., Steven, G.P., Xie, Y.M., and Querin, O.M. "Evolutionary topology optimization for temperature reduction of heat conducting fields." *International Journal of Heat and Mass Transfer* 47 (23) (2004) 5071-5083. https://doi.org/10.1016/j.ijheatmasstransfer.2004.06.010
[11] Gao, T., Zhang, W.H., Zhu, J.H., Xu, Y.J., and Bassir, D.H. "Topology optimization of heat conduction problem involving design-dependent heat load effect." *Finite Elements in Analysis and Design* 44 (14) (2008) 805-813. https://doi.org/10.1016/j.finel.2008.06.001
[12] Marck, G., Nemer, M., Harion, J.L., Russeil, S., and Bougeard, D. "Topology optimization using the SIMP method for multiobjective problems." *Numerical Heat Transfer, Part B: Fundamentals* 61 (6) (2012) 439-470. https://doi.org/10.1080/10407790.2012.687979
[13] Lee, G., Lee, I., and Kim, S.J. "Topology optimization of a heat sink with an axially uniform cross-section cooled by forced convection." *International Journal of Heat and Mass Transfer* 168 (2021) 120732. https://doi.org/10.1016/j.ijheatmasstransfer.2020.120732
[14] Yan, S.N., Wang, F.W., Hong, J., and Sigmund O., "Topology optimization of microchannel heat sinks using a two-layer model." *International Journal of Heat and Mass Transfer* 143 (2019) 118462. https://doi.org/10.1016/j.ijheatmasstransfer.2019.118462

[15] Dede, E.M., Joshi, S.N., and Zhou, F. “Topology optimization, additive layer manufacturing, and experimental testing of an air-cooled heat sink.” *ASME Journal of Mechanical Design* 137 (11) (2015) 11403-1-111403-9. https://doi.org/10.1115/1.4030989
[16] Zhang, B., Zhu, J., Xiang, G., and Gao, L. “Design of nanofluid-cooled heat sink using topology optimization.” *Chinese Journal of Aeronautics* 34 (2) (2021) 301-317. https://doi.org/10.1016/j.cja.2020.05.023
[17] Li, H.L., Lan, D.Y., Zhang, X.M., and Cao, B.Y. “Investigation of the parameter-dependence of topology-optimized heat sinks in natural convection.” *Heat Transfer Engineering* (2021) 1-15. https://doi.org/10.1080/01457632.2021.1919972
[18] Alexandersen, J., Aage, N., Andreasen, C.S., and Sigmund, O. “Topology optimisation for natural convection problems.” *International Journal for Numerical Methods in Fluids* 76 (10) (2014) 699-721. https://doi.org/10.1002/fld.3954
[19] Alexandersen, J., Sigmund, O., and Aage, N. “Large scale three-dimensional topology optimisation of heat sinks cooled by natural convection.” *International Journal of Heat and Mass Transfer* 100 (2016) 876-891. https://doi.org/10.1016/j.ijheatmasstransfer.2016.05.013
[20] Alexandersen, J., Sigmund, O., Meyer, K.E., and Lazarov, B.S. “Design of passive coolers for light-emitting diode lamps using topology optimization.” *International Journal of Heat and Mass Transfer* 122 (2018) 138-149. https://doi.org/10.1016/j.ijheatmasstransfer.2018.01.103
[21] Lei, T., Alexandersen, J., Lazarov, B., Wang, F., Haertel, J., De Angelis, S., Sanna, S., Sigmund, O., and Engelbrecht, K. “Investment casting and experimental testing of heat sinks designed by topology optimization.” *International Journal of Heat and Mass Transfer* 127 (2018) 396-412. https://doi.org/10.1016/j.ijheatmasstransfer.2018.07.060
[22] Audunson, T., and Gebhart, B. “An experimental and analytical study of natural convection with appreciable thermal radiation effects.” *Journal of Fluid Mechanics* 52 (1) (1972) 57-95. https://doi.org/10.1017/S0022112072002976
[23] Carpenter, J.R., Briggs, D.G., and Sernas, V. “Combined radiation and developing laminar free convection between vertical flat plates with asymmetric heating.” *ASME Journal of Heat Transfer* 98 (1) (1976) 95-100. https://doi.org/10.1115/1.3450476
[24] Chu, W.X., Lin, Y.C., Chen, C.Y., and Wang, C.C. “Experimental and numerical study on the performance of passive heat sink having alternating layout.” *International Journal of Heat and Mass Transfer* 135 (2019) 822-836. https://doi.org/10.1016/j.ijheatmasstransfer.2019.02.034
[25] Hall, D.A., Vliet, G.C., and Bergman, T.L. “Natural convection cooling of vertical rectangular channels in air considering radiation and wall conduction” *ASME Journal of Electronic Packaging* 121 (2) (1999) 75-84. https://doi.org/10.1115/1.2792671
[26] Huang, C.H., and Wu, Y.T. “An optimum design for a natural convection pin fin array with orientation consideration.” *Applied Thermal Engineering* 188 (2021) 116633. https://doi.org/10.1016/j.applthermaleng.2021.116633
[27] Jang, D., Yu, S.H., and Lee, K.S. “Multidisciplinary optimization of a pin-fin radial heat sink for LED lighting applications.” *International Journal of Heat and Mass Transfer* 55 (4) (2012) 515-521. https://doi.org/10.1016/j.ijheatmasstransfer.2011.11.016
[28] Bahadormanesh, N., and Salimpour, M.R. “Constructal design of high-emissivity radiation inserts embedded in a disk-shaped heat generation body.” *Applied Thermal Engineering* 112 (2017) 638-648. https://doi.org/10.1016/j.applthermaleng.2016.09.138
[29] Tan, J.Y., Zhao, J.M., and Liu, L.H. “Geometric optimization of a radiation-conduction heating device using meshless method.” *International Journal of Thermal Sciences* 50 (10) (2011) 1820-1831. https://doi.org/10.1016/j.ijthermalsci.2011.05.009
[30] Castro, D.A., Kiyono, C.Y., and Silva, E.C.N. “Design of radiative enclosures by using topology optimization.” *International Journal of Heat and Mass Transfer* 88 (2015) 880-890. https://doi.org/10.1016/j.ijheatmasstransfer.2015.04.077
[31] Zhao, X., Yin, Y., He, Z., and Liu, X. “Inverse design of indoor radiant terminal using the particle swarm optimization method with topology concept.” *Building and Environment* 204 (2021) 108117. https://doi.org/10.1016/j.buildenv.2021.108117
[32] Sevart, C.D., and Bergman, T.L. “Evolutionary design method for a conducting solid cooled by combined free convection and radiation.” *ASME Journal of Heat Transfer* 143 (4) (2021) 042103. https://doi.org/10.1115/1.4049841

[33] Wang, C., Yu, Z., Zhou, M., and Qian, X. “Topology optimization of thermophotonic problem for daytime passive radiative cooling.” *International Journal of Heat and Mass Transfer* 183 (2022) 122097. https://doi.org/10.1016/j.ijheatmasstransfer.2021.122097
[34] Patankar, S.V. *Numerical Heat Transfer and Fluid Flow, first ed*., Hemisphere, New York, (1980).
[35] Hottel, H. C. *Radiant Heat Transmission, in: W. H. McAdams, (Ed.), Heat Transmission*, McGraw-Hill, New York, (1954).
[36] Svanberg, K. “The method of moving asymptotes – a new method for structural optimization,” *International Journal for Numerical Methods in Engineering*, 24 (2) (1987) 359-373. https://doi.org/10.1002/nme.1620240207

Paper P4

Title:

A Dual Solid Method for Topological Optimization of a Conducting Solid Cooled by Gas Conduction and Surface Radiation

Authors:

Chadwick D. Sevart

Theodore L. Bergman

Journal:

ASME Journal of Heat Transfer

A Dual Solid Method for Topological Optimization of a Conducting Solid Cooled by Gas Conduction and Surface Radiation

Chadwick D. Sevart
University of Kansas
Lawrence, KS, 66044
e-mail: cdsevart@ku.edu

Theodore L. Bergman
University of Kansas
Lawrence, KS, 66044
e-mail: tlbergman@ku.edu

Abstract – The topological optimization of a conducting solid simultaneously cooled by (*i*) conduction to a stationary, radiatively non-participating fluid and (*ii*) surface-to-surface radiation exchange is performed. A novel Dual Solid Method (DSM) that utilizes concurrent discrete and continuous descriptions of the solid phase distribution is introduced. Corresponding discrete and continuous solid models are used to (*i*) quantify the conduction and radiation heat transfer, and (*ii*) power a density-based topology optimization, respectively. The discrete and continuous models of the DSM are linked by sharing information pertaining to the radiation exchange process. The influence of the relative strengths of conduction and radiation is illustrated by performing parametric simulations involving various domain boundary temperatures and solid phase thermal conductivities. In general, use of the DSM to account for radiation heat transfer leads to solid shapes of reduced complexity, relative to shapes predicted when radiation is neglected.

Keywords – *Topology Optimization, Conjugate Heat Transfer, Radiation*

1 Introduction

Identification of optimal solid configurations is of interest in many heat transfer applications. The optimization often involves minimization of an overall thermal resistance, subject to constraints on the

volume or weight of solid material. Early attempts involved size and shape optimization, where general geometric features are specified *a priori* and their dimensions are considered as the optimization parameters. For example, Bar-Cohen *et al.* [1] considered plate-fin heat sinks cooled by natural convection, and maximized the heat transfer rate per volume by varying the fin thickness and fin pitch.

A limitation of size and shape optimization is that the actual optimal geometries may be complex, and not reduceable to simple geometrical features. As is well known, a method that allows for geometrical complexity is constructal theory [2], which involves the hierarchical construction and optimization of conducting or flow paths. The overall geometry is obtained by assembling multiple smaller sections. Although the smallest geometric features are specified *a priori*, the overall geometry is allowed to evolve into more intricate shapes that can be unanticipated. For example, Bejan [2] predicted a branching tree-like structure for cooling a heat generating volume so that the local maximum temperature is minimized. Almogbel and Bejan [3] considered a similar problem and found that allowing nonuniformly spaced branches increased the allowable number of constructs (branches) resulting in more complex geometries with lower thermal resistances.

The method that allows the most geometrical flexibility is topology optimization (TO) [4]. The advantages of TO are rooted in its initial description of a material distribution throughout the entirety (or large portion) of a computational domain. From this unbiased starting point, the evolution of complex solid shapes proceeds without any specification of geometric features or sub-features. In general, the TO process applied to a heat transfer problem involves (*i*) specification of an initial material distribution, (*ii*) solution of the appropriate governing equations (*e.g.*, the heat equation), followed by (*iii*) adjustment of the material distribution according to an optimization algorithm that is informed by the spatial distribution of the state variables (*e.g.*, the temperature distribution). Steps (*ii*) and (*iii*) are repeated until the solid shape converges to an optimal form. There are various types of TO methods, categorized by the material distribution methodology and optimization algorithm used [5]. One type involves a density based method, in which the solid shape is defined by a discretized distribution of local solid volume fractions. This distribution can be

discrete, for which each location in a domain is computationally solid or fluid, or continuous, where some locations have intermediate values of a solid volume fraction and are treated as a mixture of solid and fluid.

An early example of TO applied to heat conduction is that of Li *et al.* [6] in which a discrete evolutionary method was used to minimize the temperature at a specified location. The domain was initially filled with solid material from which solid elements were selectively removed based on the sensitivity of the objective temperature to a given solid element. Gersborg-Hansen *et al*. [7] developed a continuous TO method utilizing the finite volume method for a heat conduction problem. The optimized solids were complex branching structures. Topology optimization for heat conduction problems has been investigated extensively [8-10] and is relatively well-developed.

It is necessary to consider multiple modes of heat transfer in most applications. For example, a simple way to incorporate the effects of convection using TO is to impose a boundary condition based on Newton's law of cooling [11]. The effects of convection can also be modeled by introducing a temperature-dependent source term in the heat diffusion equation, such as done by Iga *et al*. [12] in which a continuous density based TO method was utilized. The source term was dependent on the local solid fraction through a Hat function which was non-zero only at locations of intermediate solid fraction values, therefore incorporating the effects of convection only at solid-fluid interfaces. It was found that the optimal geometry became less complex when the strength of convection was increased.

A more accurate way of incorporating convection into TO is through solution of the Navier-Stokes equations [13-19]. Yoon [13] considered a forced convection problem and applied a continuous density based TO method. It was found that the optimal geometries led to high fluid velocities at the locations of the applied heat rate. Alexandersen *et al*. [17] considered a natural convection problem. As with the results of [12], it was reported that the geometries become simpler as the strength of convection is increased. The methods of Alexandersen *et al.* [17] were later adapted to three-dimensional geometries [18] and then used for the design of heat sinks [19] which were subsequently fabricated using additive manufacturing [20].

The branching tree-like structures were shown to exhibit a lower maximum temperature and a reduced mass compared to traditional heat sink geometries.

Optimal geometric configurations for heat transfer processes are also affected by thermal radiation [21,22]. While the effects of radiation have been considered extensively in size and shape optimization studies [23-31], the development of TO methods which incorporate the effects of thermal radiation has been slow. Only a few examples exist in the literature, with most concerned with the optimal material distribution on a surface of simple geometry. For example, Castro *et al*. [32] considered a three-dimensional radiative enclosure with negligible conduction and convection effects. Three objective function cases were considered with the goal being (*i*) minimization of the temperature at a specified location and (*ii*) either minimization or maximization of the net radiative heat flux at a specified location. A continuous density based TO method was used to determine the optimal distribution of high emissivity material on multiple surfaces inside the enclosure.

A more complex problem is the optimization of a conducting solid cooled or heated by radiation. For example, Shen *et al*. [33] used a continuous TO method to determine the optimal distribution of material on the exterior casing of an electronics device. Three-dimensional conduction was considered within the casing material and the effects of radiation were treated as a boundary condition. Wang *et al*. [34] considered the optimization of the microscale features of a thin structure in order to maximize the heat rate at a surface. A convection boundary condition was enforced on the top surface. The effects of radiation were incorporated by introducing a uniformly distributed source term into the heat diffusion equation. The source term was considered to be independent of the temperature distribution, therefore the heat transfer processes were only weakly coupled. The source term did depend on the emissivity which was influenced by the material distribution. Therefore, the optimal material distribution was influenced by radiation, conduction, and convection.

To the authors' knowledge, Shen *et al*. [33] and Wang *et al*. [34] are the only investigators to consider a formal TO method for the design of a conducting solid cooled by radiation. However, a situation that has

not been treated with a formal TO approach is one where conduction is coupled with surface-to-surface radiation transfer that is, in turn, dependent on both the temperature distribution and the solid shape. Such a situation was considered by Sevart and Bergman [35] in which desirable shapes of a conducting solid cooled by conjugate radiation and natural convection processes were determined. While the solid geometry had no features specified *a priori*, a heuristic evolutionary design method was employed rather than a formal TO method. It was found that, even for low surface emissivities, the effects of radiation had a significant influence on the predicted optimal shape and the overall thermal resistance.

This study is concerned with the optimization of a solid configuration that is cooled by conjugate gas conduction and surface-to-surface radiation using a formal TO method that requires the assumption of a continuous, non-discrete solid. As is perhaps obvious, the main challenge is associated with incorporating the effects of radiation to or from distinct solid surfaces into a model that assumes a non-discrete, continuous material that is, in general, devoid of distinct solid surfaces. To address this challenge, a novel Dual Solid Method (DSM), which utilizes both discrete and continuous descriptions of the solid distribution, is introduced and developed.

2 Physical and Numerical Model

The physical situation is shown in Fig. 1, in which a two-dimensional, square enclosure of dimension H consists of (i) a specified amount of solid of thermal conductivity k_s, and (ii) a stationary, radiatively transparent fluid of thermal conductivity k_f. The exposed surfaces of the solid and the interior walls are of emissivity ε. A heat rate per unit length, q', is applied at the bottom center of the domain over width b, while the top boundary is isothermal at T_o. All remaining enclosure boundaries are adiabatic. The solid is restricted to the portion of the domain below $y_{\max}$.

The solid shape that provides the smallest total thermal resistance ($R'_{\text{tot}} \equiv [T(H/2,0) - T_o]/q'$) will be determined by utilizing both a discrete and a continuous description of the solid material distribution. The

continuous description is used in conjunction with a topological optimization method to redistribute the material, while the discrete description is necessary to evaluate the radiation exchange between surfaces. As will become evident, the two models are linked by the spatial distribution of thermal energy source terms associated with the radiation heat transfer. Hence, the topologically redistributed solid shape is dependent on (*i*) conduction in both the solid and fluid as well as (*ii*) radiation exchange at the exposed solid surfaces.

2.1 Governing Equations: Discrete Solid Distribution. The temperature distribution throughout the domain can be determined by solving distinct conservation of thermal energy equations in both the solid and the fluid. Steady state conditions are assumed, and the thermophysical properties are considered to be constant. It is assumed that the fluid is stationary and does not participate in the radiation exchange process, while all surfaces are assumed to be opaque, diffuse, and gray. With these assumptions, both the solid and fluid temperature distributions are governed by the heat diffusion equation:

$$\frac{\partial}{\partial x}\left(k\frac{\partial T}{\partial x}\right)+\frac{\partial}{\partial y}\left(k\frac{\partial T}{\partial y}\right)=0 \tag{1}$$

with $k=k_s$ for the solid and $k=k_f$ for the fluid. Along all solid-fluid interfaces, the heat flux from the solid is equal to the sum of the conduction and radiation heat fluxes from the interface,

$$-k_s\frac{\partial T}{\partial n_s}=-k_f\frac{\partial T}{\partial n_s}+q''_{\mathrm{rad}} \tag{2}$$

where n_s is the direction normal to the solid surface as shown in Fig. 1. Similarly, the sum of the conduction and radiation heat fluxes is zero along the exposed adiabatic boundaries,

$$-k_f\frac{\partial T}{\partial n_b}+q''_{\mathrm{rad}}=0 \tag{3}$$

If the solid is in contact with an adiabatic boundary, blocking radiation, the boundary condition is:

$$-k_s\frac{\partial T}{\partial n_b}=0 \tag{4}$$

Isothermal conditions are specified along the top of the domain, $T(x, y = H) = T_o$, and a uniform heat rate per unit length is applied over a width b at the bottom center of the domain:

$$-k_s \frac{\partial T}{\partial y}\Big|_{y=0} = q'/b \tag{5}$$

The radiation heat fluxes appearing in Eqs. (2) and (3) are evaluated as described in Appendix A.

2.2 Governing Equations: Continuous Solid Distribution. The continuous solid approach involves the spatial distribution of the local solid fraction, $\gamma(x, y)$, where $0 \leq \gamma \leq 1$. Because distinct solid surfaces are in general absent in the continuous solid formulation, surface-to-surface radiation heat transfer is accommodated by use of a spatially distributed source term, $S_{\mathrm{rad},cm}(x, y)$, that is related to the radiation heat transfer of the discrete solid model and is independent of $\gamma(x, y)$. Equation (1) is re-cast as:

$$\frac{\partial}{\partial x}\left(k \frac{\partial T}{\partial x}\right) + \frac{\partial}{\partial y}\left(k \frac{\partial T}{\partial y}\right) + S_{\mathrm{rad},cm}(x, y) = 0 \tag{6}$$

where local thermal conductivities are determined from $\gamma(x, y)$ so that $k_f \leq k \leq k_s$. Unlike in the discrete model formulation, the adiabatic boundary of the continuous model cannot be separated into sections which are exposed or covered by solid. Therefore, the condition along the entire adiabatic boundary can be stated as:

$$-k \frac{\partial T}{\partial n_b} + q_b'' = 0 \tag{7}$$

where $q_b'' = 0$ or q_{rad}'' depending on information provided from the discrete model. The boundary conditions at the location of the applied heat rate and along the top, isothermal boundary are the same as in the discrete solid formulation.

2.3 Discretization of the Governing Equations and Boundary Conditions: Discrete Solid Distribution. The finite volume method is used to solve the discretized form of Eq. (1) with harmonic-mean thermal conductivities specified at all control surfaces [36]. Equal-sized computational control volumes of dimension $\Delta x = \Delta y = \Delta w$ are distributed throughout the domain, with each control volume

being either solid (k_s) or fluid (k_f). Equation (2) is treated computationally by incorporating a radiation source term, $S_{\mathrm{rad},dm}(x,y)$, into the discretized form of Eq. (1). The source term is determined based on the local radiation heat fluxes that are calculated as described in Appendix A:

$$S_{\mathrm{rad},dm}(x,y) = -\sum_{i=1}^{4} q''_{\mathrm{rad},i}/\Delta w \tag{8}$$

where $q''_{\mathrm{rad},i}$ is the radiation heat flux from control surface *i* of the control volume located at (*x*, *y*), and Δw is the control volume dimension. The condition at the exposed adiabatic boundary is handled by setting a constant boundary temperature that satisfies the discretized form of Eq. (3). The coupled radiation-conduction problem for a fixed solid distribution is therefore solved using the following iterative procedure: (*i*) $T(x,y)$ is obtained neglecting radiation ($S_{\mathrm{rad},dm}(x,y) = 0$), (*ii*) the local radiation heat fluxes that appear in Eqs. (2) and (3) are calculated or updated, (*iii*) the radiation source terms, $S_{\mathrm{rad},dm}(x,y)$, and boundary temperatures at the exposed adiabatic boundary are calculated, and (*iv*) the discretized form of Eq. (1) is solved again with the updated source terms and boundary temperatures. Steps (*ii*) – (*iv*) are repeated until the maximum change in any local temperature is less than 10^{-8} K.

2.4 Discretization of the Governing Equations and Boundary Conditions: Continuous Solid Distribution. The finite volume method, with control volumes co-located with those of the discrete solid model, is also used to solve the discretized form of Eq. (6). The local solid fraction, $\gamma(x,y)$ determines the local thermal conductivity based on an interpolation scheme. When using the continuous solid approach, it is desirable to obtain a crisp or binary material distribution that has most control volume values nearly equal to 0 or 1. To achieve this, an interpolation scheme is used to define the local thermal conductivity in Eqs. (6) and (7) which penalizes intermediate solid fractions. The Solid Isotropic Material with Penalization (SIMP) method [4] used here is:

$$k(\gamma) = k_f + \gamma^P (k_s - k_f) \tag{9}$$

where *P* is the penalization parameter. Here, *P* = 3 was selected based on preliminary sensitivity studies, consistent with the recommendations of other researchers [5, 37].

A spatial distribution of source terms, determined from the discrete model, is utilized to accommodate the effects of surface radiation heat transfer:

$$S_{\mathrm{rad},cm}(x,y) = S_{\mathrm{rad},dm}(x,y) \tag{10}$$

The boundary condition of Eq. (7) is enforced by specifying the source term at the boundary as:

$$S_{\mathrm{rad},cm}(x,y) = -q_b''/\Delta w \tag{11}$$

As will become evident, Eq. (10) links the discrete and continuous solid models, and is utilized throughout the topological optimization process.

3 Topology Optimization (TO) Applied to the Continuous Solid Model

The continuous solid distribution is adjusted using a sensitivity-based, TO method for which the objective function

$$f_o(\gamma,T) = T(H/2,0) \tag{12}$$

is minimized. This is equivalent to minimizing the total thermal resistance subject to

$$\sum_{i=1}^{N}\gamma_i \le V_o \times N \tag{13}$$

and

$$0 \le \gamma_i \le 1 \tag{14}$$

while satisfying Eqs. (5) – (7). Here, γ_i is the solid fraction of an arbitrary control volume i, V_o is the total solid fraction of the entire domain, and N is the total number of computational control volumes in the domain.

The Method of Moving Asymptotes (MMA) is used to optimize $\gamma(x,y)$ [38]. This technique makes use of the sensitivities of the objective function to the solid fraction values, $\partial f_o/\partial\gamma$, to generate a convex approximation of f_o, the details of which are described by Svanberg [38]. The solution of the convex

problem provides the updated solid fraction distribution of the continuous solid model. Therefore, at each iteration of the TO process a new convex approximation is formulated and solved in order to adjust the solid distribution, $\gamma(x, y)$.

The main components of the TO process as applied to the continuous model are depicted in Fig. 2. Initially, the solid fraction is spatially uniform, $\gamma(x, y) = V_o$, and the radiation source term is either $S_{\mathrm{rad},cm}(x, y) = 0$ to begin the simulation, or $S_{\mathrm{rad},cm}(x, y) = S_{\mathrm{rad},dm}(x, y)$. The optimization proceeds as follows. First, $k(\gamma)$ is determined based on the SIMP method. Then the discretized equations are solved to determine $T(x, y)$ and f_o. Using the temperature and solid fraction distributions, the sensitivities are then calculated and filtered as described in Appendix B. Lastly, $\gamma(x, y)$ is adjusted based on the filtered sensitivities using the MMA. The process shown by the dark arrow in Fig. 2 is repeated until the maximum change in local solid fraction, $\Delta\gamma_{\max}$, is less than a convergence criterion, CC = 0.001 (Appendix C). The counter used in the continuous model, I_{cm} = 0, 1, 2, …, tracks the number of times $\gamma(x, y)$ is adjusted for each unique $S_{\mathrm{rad},cm}(x, y)$. The iterative process of Fig. 2 must be revisited and completed for each unique $S_{\mathrm{rad},dm}(x, y)$ distribution that is transferred from the discrete model formulation by way of Eq. (10).

4 The Dual Solid Method

The DSM, introduced here, utilizes both the discrete and continuous solid models, and is outlined in Fig. 3. The counter I_{DSM} = 0, 1, 2, … is used to track the number of times a discrete solid distribution is created using the methodology described below, with each unique value of I_{DSM} referred to as a *design iteration* [17-19]. First, the optimal continuous solid distribution for the pure conduction problem (I_{DSM} = 0, $S_{\mathrm{rad},cm}(x, y) = 0$) is obtained using the process of Fig. 2. An equivalent discrete solid shape corresponding to a domain solid fraction V_o is then generated with the number of solid control volumes, N_s, determined from $N_s = V_o \times N$. The resulting N_s solid control volumes are distributed throughout the

domain as follows. First, the solid fraction values of individual control volumes $\gamma(x, y)$ of the continuous model are sorted, then the N_s control volumes with the largest values of γ are specified to be solid in the discrete solid model. With the discrete solid (and fluid) distribution now determined from the predictions of the continuous model, distinct solid surfaces that experience radiation transfer are now present, and the coupled radiation-conduction problem is solved as described in Section 2.3.

After the solution of the radiation-conduction model, the radiation source terms that are calculated with the converged radiation-conduction solution using Eq. (8) are sent back to the continuous solid model by way of Eq. (10), and the TO process of Fig. 2 is repeated ($I_{\mathrm{DSM}} = 1$, $S_{\mathrm{rad},cm}(x, y) \geq 0$) to determine a new continuous solid distribution. The corresponding new discrete solid is then generated, and the process of sharing source terms and gradually re-sculpting the discrete solid shape is repeated ($I_{\mathrm{DSM}} = 2, 3, 4, \ldots$) until (*i*) the discrete solid distribution does not change as I_{DSM} is increased, or (*ii*) the discrete solid oscillates between two distinct distributions as I_{DSM} is increased, or (*iii*) a large number of design iterations have been performed.

As might be expected, the total thermal resistance changes from design iteration-to-design iteration as the individual control volumes with the largest N_s solid fraction values shift their positions in the computational domain. Moreover, even minor adjustments to the solid shape can produce or eliminate surface-to-surface radiation obstructions that can significantly impact the total radiation resistance. Mainly because of the sensitivity of local radiation heat fluxes to the redistribution of the discrete solid, it will be observed that the discrete solid shape may not monotonically converge to an optimal form as I_{DSM} increases. To accommodate this behavior, the simulations will typically be allowed to proceed through a large number of design iterations, and the solid shape associated with the lowest total thermal resistance will be deemed to be optimal, while acknowledging that more desirable solid shapes could possibly emerge if an extremely large number of design iterations were to be performed.

5 Results

In this section, the topological optimization of the continuous solid will first be demonstrated. Mapping the optimized continuous solid distribution to the discrete solid distribution will be discussed, and the radiation transfer equations will be incorporated into the predictions to demonstrate their effect. After the initial phase of the DSM is presented, the entire design process will be allowed to proceed, and optimal shapes along with their associated thermal performance will be reported.

The DSM is applied to the physical system of Fig. 1, using a range of top boundary temperatures and solid thermal conductivities, in order to ultimately determine the influence of radiation and conduction on the solid shape that is associated with the lowest total (radiation + conduction) thermal resistance. For all cases, the thermal conductivity of the fluid is that of air (k_f = 0.0257 W/m·K) and all surfaces have an emissivity of either ε = 0 (pure conduction) or ε = 1. The total solid fraction is specified to be V_o = 0.05. The characteristic length of the domain is H = 0.06 m and b/H = 1/90. A base case of T_o = 750 K and k_s = 237 W/m·K is considered. The applied heat rate at the bottom center of the domain is q' = 10 W/m for all cases. All of the results are generated using a 180 × 180 computational control volume mesh based on a grid sensitivity study (Appendix C). One hundred isotherms are shown in each plot of temperature distributions.

5.1 Demonstration of TO Applied to the Continuous Solid Model. As described in Section 4, the initial step in the DSM approach is to obtain the optimal continuous solid distribution for the pure conduction problem. The evolution history of the conduction resistance, as well as the continuous solid distribution for various I_{cm} are reported in Fig. 4. As evident, the conduction resistance decreases rapidly as the solid evolves from its initial uniform, low density distribution to the branching structure shown. As the TO proceeds, the solid becomes more distinct as intermediate solid fraction values are replaced with values that are nearly 0 or 1, as driven by the penalization scheme of Section 2.4.

The optimal continuous solid distribution (I_{cm} = 1350) and corresponding temperature distribution for the ε = 0 case are shown in Fig. 5(a). The temperature distribution is dominated by the presence of the thin, high thermal conductivity solid that propagates high temperatures from the location of the applied heat rate toward the cold upper surface. There is a high concentration of isotherms within $y \geq y_{\max}$ because of the exclusion of the solid from this region. The conduction heat flux at all adiabatic boundaries is zero, as evident by the temperature distributions adjacent to these boundaries.

5.2 Generation of a Discrete Solid Shape and the Influence of Radiation. The discrete solid distribution of Fig. 5(b) is created from the continuous solid distribution of Fig. 5(a) using the sorting methodology described in Section 4. Applying the discrete solid model with ε = 1 to the solid distribution of Fig. 5(b) leads to the corresponding temperature distribution shown. As in Fig. 5(a), the temperature distribution is influenced by the high thermal conductivity solid. In contrast to the pure conduction temperature distribution of Fig. 5(a), however, there is a larger concentration of isotherms in the $y < y_{\max}$ section of the domain for the ε = 1 case. This is because, for ε = 1, the thermal resistance in the $y \geq y_{\max}$ region of the domain is reduced by the combined effects of conduction in the fluid and radiation exchange between the top of the solid structure and the isothermal top boundary. When radiation is included in the analysis, the isotherms of Fig. 5(b) are no longer normal to the adiabatic boundaries, as required by Eq. (3).

The conduction resistance corresponding to the discrete solid of Fig. 5(b) may be obtained by specifying ε = 0 in the discrete model. A comparison of the conduction resistances corresponding to the continuous and discrete solid distributions of Fig. 5 (see inserts) reveals a slightly larger value for the discrete solid case. The difference in conduction resistances is attributed to (i) the approximations inherent in mapping a continuous shape to a discrete shape and (ii) the presence of γ values in the continuous model that are not equal to 0 or 1. In contrast, a comparison of the total resistances of Fig. 5 reveals the significance of radiation, with $R'_{\text{tot}}/R'_{\text{cond}} = 1$ and ≈ 0.3 reported in Figs. 5(a) and 5(b), respectively.

5.3 TO Applied to the Continuous Solid Model with Radiation. The effects of radiation that are embedded in the predictions of Fig. 5(*b*) are passed back to the TO process of Fig. 2 through the use of Eq. (10) to create a set of non-zero source terms for use in the continuous model, $S_{\mathrm{rad},cm}(x,y) \geq 0$. The continuous model TO, with its non-zero source terms located throughout the domain, is then solved for the first time, $I_{\mathrm{DSM}} = 1$.

The evolution history of the first TO process to include the effects of radiation ($I_{\mathrm{DSM}} = 1$) is shown in Fig. 6. Similar to the pure conduction evolution of Fig. 4, the total (radiation + conduction) thermal resistance decreases as the solid evolves from its initial uniform distribution to a more distinct branching structure. The discrete solid generated from the optimum continuous solid distribution (I_{cm} = 1911, Fig. 6) and the associated temperature distribution are shown in Fig. 7. Modest differences in the solid shapes and temperature distributions of Figs. 5(*b*) ($I_{\mathrm{DSM}} = 0$) and 7 ($I_{\mathrm{DSM}} = 1$) can be observed upon close inspection, with the first bifurcation of the solid moved to a lower position in the domain. Also, the total thermal resistance has decreased from R'_{tot} = 0.253 m·K/W ($I_{\mathrm{DSM}} = 0$) to 0.250 m·K/W ($I_{\mathrm{DSM}} = 1$) but the corresponding resistance due to pure conduction has increased from R'_{cond} = 0.852 m·K/W to 0.905 m·K/W. As will become evident, the solid shapes and associated heat transfer phenomena continue to evolve as the dual solid method is allowed to run its course ($I_{\mathrm{DSM}} = 2, 3, 4, \ldots$).

5.4 Base Case Results. The evolution histories of the total and pure conduction thermal resistances associated with the discrete solid model are shown in Fig. 8. As evident, there is an initial sharp decrease in the total thermal resistance, coinciding with a sharp increase in the pure conduction resistance, suggesting the evolution of solid shapes that continually perform worse (better) from the conduction (radiation + conduction) perspective as the design iterations proceed. Both resistances approach constant values at $I_{\mathrm{DSM}} \approx 15$, with the total thermal resistance achieving a minimum value at $I_{\mathrm{DSM}} = 54$, as identified by the filled data symbol. The discrete solid and associated temperature distributions for $I_{\mathrm{DSM}} = 54$ are shown in Fig. 9. A comparison of the solid distributions of Figs. 5(*b*) and 9 reveals significant differences. For example, the locations at which any solid branch bifurcates is shifted to a lower position in the domain.

Also, the gap in the horizontal solid section near $y_{\max}$ has widened, allowing radiation to more freely penetrate the domain in the vertical direction. Quantitatively, the central gap has doubled in width from $8\Delta x$ at I_{DSM} = 0 to $16\Delta x$ at I_{DSM} = 54. The effectiveness with which the DSM method can determine solid shapes that enhance the combined radiation-conduction transfer across the domain is especially noteworthy, considering that the solid shape of Fig. 9 poses a substantially larger pure conduction resistance relative to the conduction-optimized shape of Fig. 5(*b*).

5.5 Parametric Simulations. The influence of radiation relative to that of conduction will be investigated by way of several parametric studies conducted with the DSM.

5.5.1 Influence of the top boundary temperature. Top boundary temperatures of T_o = 1000 K and 500 K are now considered in addition to the base case of T_o = 750 K. The evolution histories of the total and conduction thermal resistances associated with the discrete solid distribution for the T_o = 1000 K and 500 K cases are shown in Fig. 10, and can be compared to the histories of the base case reported in Fig. 8. As evident in Fig. 10(*a*), the total resistances are significantly smaller for the T_o = 1000 K case compared to the base case, but the conduction resistances are of similar value for T_o = 750 K and 1000 K, as expected. In contrast to the evolution behavior noted in Fig. 8, the resistances more monotonically approach optimal values as radiation is strengthened by increasing T_o. The T_o = 1000 K simulations are stopped at I_{DSM} = 31, the point at which the discrete solid begins to oscillate between two distinct shapes as I_{DSM} is increased.

The resistance histories for the T_o = 500 K case, reported in Fig. 10(*b*), exhibit complexity as the DSM seeks an optimal solid configuration. The inability of the DSM to more readily identify an optimal configuration for this weak-radiation case is attributed to the good radiation-conduction performance that is already offered by a solid configuration that has been optimized under pure conduction conditions. In fact, the minimum total thermal resistance for T_o = 500 K is associated with I_{DSM} = 0 as evident in Fig. 10(*b*). The T_o = 500 K simulations are curtailed at I_{DSM} = 61, at which point the solid distribution no longer changes with increasing I_{DSM}.

The solid shapes associated with I_{DSM} = 0 are identical for the three cases and correspond to Fig 5(*b*). The discrete solid shapes and temperature distributions associated with $R'_{\mathrm{tot,min}}$ for the three T_o cases are shown in Fig. 11. As T_o is increased, the point at which the thick solid first bifurcates moves lower in the domain, eventually coming into close proximity to the location of the applied heating. Correspondingly, more space is provided between the two main branches of the solid as T_o is increased. Importantly, there is an increase in the width of the central gap in the horizontal solid section near $y_{\max}$, with widths of 8Δ*x*, 16Δ*x*, and 22Δ*x* for the solid distributions of Figs. 11(*a*), 11(*b*), and 11(*c*) respectively. The inner branches associated with the second bifurcation of the solid become shorter as T_o increases, again reducing the resistance to upward propagation of thermal radiation. In general, increasing T_o produces solid shapes that reduce the total (radiation + conduction) thermal resistance across the domain, even as the isolated conduction component of the total resistance increases in value.

5.5.2 Influence of the solid thermal conductivity. A dimensionless solid thermal conductivity is introduced, $k_s^* \equiv k_s/237$ W/m·K, and the DSM is used to predict the evolution histories of the thermal resistances for k_s^* = 0.01 and 0.1 with T_o = 750 K reported in Figs. 12(*a*) and 12(*b*), respectively. For the weakest solid conduction (strongest radiation) case, Fig. 12(*a*), the total thermal resistance decreases and the conduction resistance increases monotonically until the DSM stops at I_{DSM} = 9, after which the solid distribution does not change with increasing I_{DSM}. The evolution histories of the k_s^* = 0.1 case, shown in Fig. 12(*b*), exhibit a large initial decrease (increase) in the total (pure conduction) thermal resistance between I_{DSM} = 0 and 1, followed by small changes for $I_{\mathrm{DSM}} > 1$. The minimum value of the total thermal resistance occurs at I_{DSM} = 16 and, interestingly, coincides with the maximum conduction resistance. The predictions were curtailed after a large number of iterations, I_{DSM} = 100.

Both the initial (I_{DSM} = 0) and the optimal (I_{DSM} > 0) discrete solid shapes and temperature distributions associated with the conduction-radiation (ε = 1) cases are reported in Fig. 13. Also included are the

corresponding conduction and total thermal resistances. Again, the discrete solid shapes associated with I_{DSM} = 0 (left column of Fig. 13) are obtained from the pure conduction TO.

As evident in the second and third rows of the first column of Fig. 13, the optimal discrete solid shapes that were generated from the continuous model with ε = 0 are similar for k_s^* = 0.1 and 1. In both cases $k_s \gg k_f$ and conduction within the solid dominates conduction in the fluid. For k_s^* = 0.01, however, conduction in the fluid becomes more important, and the solid takes the form of a relatively thick, single branch that extends upward to within proximity of the cold upper surface before bifurcating. Hence, the complexity of the solid shape increases with increasing k_s, in a manner consistent with predictions reported in previous pure-conduction shape optimization studies [8, 12]. Also, as k_s increases, slightly more of the solid migrates to the upper half of the domain.

The optimal solid shapes for the ε = 1 cases (third column of Fig. 13) differ substantially from the optimal shapes associated with ε = 0. This is especially evident for the weak conduction (strong radiation) case, $k_s^* = 0.01$, where parts of the solid propagate laterally outward, forming two horizontal, petal-like structures that do little to reduce the conduction resistance, but serve as radiatively active surfaces that improve radiative exchange with the cold upper surface. In contrast to all of the results discussed so far, the optimal solid configuration for the $k_s^* = 0.01$, ε = 1 case includes almost no material in the upper half of the domain which declutters the domain of solid obstructions to radiation heat transfer. As for the ε = 0 cases, the discrete solid shapes associated with $R'_{\mathrm{tot,min}}$ exhibit greater complexity as k_s increases. The total thermal resistances decrease with increasing k_s^* and ε , as expected.

6 Conclusions and Recommendations

A novel Dual Solid Method (DSM) that utilizes concurrent discrete and continuous descriptions of the shape of a solid has been developed to include surface radiation in a topology optimization process. The

solid geometries that minimize the overall (conduction + radiation) thermal resistance across a computational domain bear some resemblance to the branching tree-like structures reported for situations where radiation heat transfer was neglected [7,8,17]. The specific influence of coupled radiation and conduction heat transfer processes on the optimal solid shape, as well as on the corresponding overall thermal resistance, has been demonstrated and quantified through a series of parametric simulations. Increasing the average temperatures throughout the domain, achieved by increasing the temperature of the cold boundary, increases the influence of radiation. This leads to more open solid shapes that can more freely exchange radiation with the cold boundary. Reducing the thermal conductivity of the solid also increases the influence of radiation, and leads to optimal geometries that can be significantly different than the geometries determined when radiation is neglected.

Acknowledging that radiation heat transfer is important, if not dominant in a broad range of practical applications, future investigations might address the following.

- The influence of free or forced convection within the fluid phase was neglected in this study. It is expected that coupled conduction-radiation-convection phenomena may lead to distinctly different optimal solid shapes than have been reported in the literature.
- The present study involves opaque solid surfaces that are assumed to be both diffuse and gray. Many solids are characterized by directional, as well as spectral radiative properties. Inclusion of these effects would require more advanced radiation modeling, and could influence the optimal solid shapes.
- The present study involves radiatively opaque solids and a radiatively non-participating gas. For situations involving semi-transparent media, the radiation model used here would need to be replaced with more advanced descriptions of the radiation processes.
- Due to their complexity, the optimized solid geometries might require additive manufacturing methods to be fabricated. It is well known that the properties of additively manufactured solids are influenced by the manufacturing process itself [39-42]. Hence, the influence of, for example,

anisotropic solid phase thermal conductivities and directional radiative properties attributable to the manufacturing process might need to be accounted for in the optimization process.

Acknowledgment

The authors acknowledge Dr. Krister Svanberg for providing the source code for the Method of Moving Asymptotes. The first author acknowledges support from the University of Kansas by way of the School of Engineering Wilburn & Mina Wyatt Memorial Scholarship.

Nomenclature

b	width of applied heat rate surface
$\{B\}$	temperature vector multiplier
CC	topology optimization convergence criterion
E_b	blackbody emissive power
F_{ij}	view factor between surfaces i and j
f_o	objective function
H	domain dimension
H_j	filter weight factor
I	counter variable
J	radiosity
k	thermal conductivity
$[K]$	coefficient matrix
k_s^*	dimensionless solid thermal conductivity
L	Lagrangian
n	normal direction
N	total number of control volumes

N_s	number of discrete solid control volumes
NS	number of exposed control surfaces
P	penalization parameter
q'	heat rate per unit length
q''	heat flux
$\{Q\}$	source term vector
$r_{\min}$	filter radius
R'	thermal resistance
S	thermal energy source term
T	temperature
$\{T\}$	temperature vector
T_o	boundary temperature
V_o	total solid fraction
Δw	control volume width
x, y	coordinate directions

Greek Symbols

γ	local solid fraction
$\Delta(i,j)$	center-to-center distance between control volumes
ε	emissivity
$\{\lambda\}$	set of adjoint variables

Subscripts

b	boundary
cond	conduction
cm	continuous model

dm discrete model

DSM Dual Solid Method

f fluid

i,j surfaces *i* and *j*

max maximum

min minimum

rad radiation

s solid

tot total

Appendix A: Calculation of Radiation Heat Fluxes.

The exposed control surfaces of the computational control volumes are assumed to be isothermal and at the temperature of the corresponding solid control volume. As such, the net radiation heat flux from diffuse and gray control surface *i* can be calculated as [43]:

$$q''_{\mathrm{rad},i} = \frac{E_{bi} - J_i}{(1-\varepsilon_i)/\varepsilon_i} \tag{15}$$

where $E_{bi} = \sigma T_i^4$ is the blackbody emissive power and J_i is the radiosity. The net radiation heat flux can also be expressed as [43]:

$$\frac{E_{bi} - J_i}{(1-\varepsilon_i)/\varepsilon_i} = \sum_{j=1}^{NS} F_{ij}(J_i - J_j) \tag{16}$$

where F_{ij} is the view factor between arbitrary control surface *i* and arbitrary control surface *j*, and *NS* is the number of exposed control surfaces. A view factor calculation methodology that accounts for the obstruction of radiation between control surfaces *i* and *j*, a situation common for complex geometries, is employed [35]. In short, the view factors are first calculated by using Hottel's crossed string method [44] without accounting for obstructions between surfaces *i* and *j*. The view factors associated with either

completely or partially obstructed control surfaces i and j are then adjusted in order to satisfy the conservation of radiation energy requirement [43]. Equations (15) and (16) are solved using Gaussian elimination. The methodology for evaluating F_{ij} is described in detail elsewhere [35].

Appendix B: Sensitivity Analysis and Sensitivity Filter.

An adjoint method is employed to determine the sensitivities of the objective function to the solid fraction values $\partial f_o/\partial \gamma$. The discretized heat equation for the continuous model can be expressed in matrix form:

$$[K]\{T\} = \{Q\} \tag{17}$$

while the objective function can then be expressed as:

$$f_o = T(H/2,0) = \{B\}^T\{T\} \tag{18}$$

where,

$$\{B\}^T = \{0,\ 0, \ldots \tfrac{1}{2},\ \tfrac{1}{2},\ \ldots 0,0\} \tag{19}$$

If Eq. (17) is satisfied, then the objective function is equivalent to the Lagrangian:

$$L = \{B\}^T\{T\} + \{\lambda\}^T([K]\{T\} - \{Q\}) \tag{20}$$

where $\{\lambda\}$ is a set of adjoint variables. Differentiating with respect to γ yields:

$$\frac{\partial L}{\partial \gamma} = \{B\}^T\left\{\frac{\partial T}{\partial \gamma}\right\} + \{\lambda\}^T\left[\frac{\partial K}{\partial \gamma}\right]\{T\} + \{\lambda\}^T[K]\left\{\frac{\partial T}{\partial \gamma}\right\} - \{\lambda\}^T\left\{\frac{\partial Q}{\partial \gamma}\right\} \tag{21}$$

Because the source term distribution handed from the discrete model is independent of the continuous solid distribution, the last term of Eq. (21) can be neglected. The remaining expression can then be rearranged to yield:

$$\frac{\partial L}{\partial \gamma} = (\{B\}^T + \{\lambda\}^T[K])\left\{\frac{\partial T}{\partial \gamma}\right\} + \{\lambda\}^T\left[\frac{\partial K}{\partial \gamma}\right]\{T\} \tag{22}$$

Therefore, calculation of $\{\partial T/\partial \gamma\}$ is not necessary if the following system of equations is satisfied:

$$[K]\{\lambda\} = -\{B\} \tag{23}$$

and the sensitivities can be evaluated as:

$$\frac{\partial f_o}{\partial \gamma} = \frac{\partial L}{\partial \gamma} = \{\lambda\}^T \left[\frac{\partial K}{\partial \gamma}\right]\{T\} \tag{24}$$

Calculation of $[\partial K/\partial \gamma]$ is straightforward using Eq. (9).

During a TO process, the solid can be prone to exhibit unrealistic checkerboard patterns in which there are alternating solid and fluid control volumes. To prevent this from occurring, a sensitivity filter is used. The sensitivities are adjusted based on the values of neighboring control volumes in order to smooth the distribution, that is

$$\frac{\widehat{\partial f_o}}{\partial \gamma_i} = \frac{1}{\gamma_i \sum_{j=1}^{N} H_j} \sum_{j=1}^{N} H_j \gamma_j \frac{\partial f_o}{\partial \gamma_i} \tag{25}$$

where

$$H_j = \max\left(0, r_{\min} - \Delta(i,j)\right) \tag{26}$$

Here, $r_{\min}$ is the filter radius and $\Delta(i,j)$ is the center-to-center distance between any pair of control volumes i and j. For all cases considered, $r_{\min} = 1.5\Delta w$, which is a value large enough to prevent checkerboard patterns, but small enough that it does not restrict the minimum feature size of the solid distribution.

Appendix C: Grid Dependence and Convergence Criterion Study.

The numerical techniques used to calculate view factors, determine local radiation heat fluxes, and solve the discretized forms of the heat equations have been validated previously [35]. Here, attention is given to the dependence of the predictions on (*i*) the convergence criterion used in the TO analysis and (*ii*) the grid size.

The DSM was conducted using *CC* = 0.01, 0.001, and 0.0005 for T_o = 750 K, k_s^* = 1, and ε = 1 using a uniform mesh of 180 × 180 control volumes. The discrete solid shapes and temperature distributions associated with I_{DSM} = 0 and with $R'_{\mathrm{tot,min}}$ for the three *CC* values are provided in Fig. 14. As is evident, the solid shapes and total thermal resistances undergo minor changes as *CC* is reduced from 0.001 to 0.0005. Considering the additional computational time required as *CC* is reduced, *CC* = 0.001 is used.

The DSM was exercised using grids of 60 × 60, 120 × 120, 180 × 180, and 240 × 240 uniform control volumes. The discrete solid shapes and temperature distributions associated with I_{DSM} = 0 and with $R'_{\mathrm{tot,min}}$ for the three largest grid sizes are reported in Fig. 15. As evident, the dependence of the solid shapes and R'_{tot} values on the grid size is significant for the larger control volume sizes, but is modest as the grid is refined from 180 × 180 to 240 × 240. Considering the tradeoff between the grid size and the total computational time required to perform the simulations (the heat equation is solved more than 10^6 times to generate the results reported here), a grid size of 180 × 180 is used for the simulations of this study.

References

[1] Bar-Cohen, A., Iyengar, M., and Kraus, A.D., 2003, "Design of Optimum Plate-Fin Natural Convective Heat Sinks," *ASME J. Electron Packag*, **125**(2), pp. 208-216. https://doi.org/10.1115/1.1568361

[2] Bejan, A., 1997, "Constructal-Theory Network of Conducting Paths for Cooling a Heat Generating Volume," *Int. J. Heat Mass Transfer*, **40**(4), pp. 799-816. https://doi.org/10.1016/0017-9310(96)00175-5

[3] Almogbel, M., and Bejan, A., 2001, "Constructal Optimization of Nonuniformly Distributed Tree-Shaped Flow Structures for Conduction," *Int. J. Heat Mass Transfer*, **44**(22), pp. 4185-4194. https://doi.org/10.1016/S0017-9310(01)00080-1

[4] Bendsøe, M.P., and Sigmund, O., 2003, *Topology Optimization: Theory, Methods, and Applications.* Springer, Berlin. https://doi.org/10.1007/978-3-662-05086-6

[5] Sigmund, O., and Maute, K., 2013, "Topology Optimization Approaches," *Struct. Multidiscip. Optim.*, **48**, pp. 1031-1055. https://doi.org/10.1007/s00158-013-0978-6

[6] Li, Q., Steven, G.P., Xie, Y.M., and Querin, O.M., 2004, "Evolutionary Topology Optimization for Temperature Reduction of Heat Conducting Fields," *Int. J. Heat Mass Transfer*, **47**(23), pp. 5071-5083. https://doi.org/10.1016/j.ijheatmasstransfer.2004.06.010

[7] Gersborg-Hansen, A., Bendsøe, M.P., and Sigmund, O., 2006, "Topology Optimization of Heat Conduction Problems Using the Finite Volume Method," *Struct. Multidiscip. Optim.*, **31**(4), pp. 251-259. https://doi.org/10.1007/s00158-005-0584-3

[8] Zhang, Y., and Liu, S., 2008, "Design of Conducting Paths Based on Topology Optimization," *Heat Mass Transfer*, **44**, pp. 1217-1227. https://doi.org/10.1007/s00231-007-0365-1

[9] Gao, T., Zhang, W.H., Zhu, J.H., Xu, Y.J., and Bassir, D.H., 2008, "Topology Optimization of Heat Conduction Problem Involving Design-Dependent Heat Load Effect," *Finite Elem. Anal. Des.*, **44**(14), pp. 805-813. https://doi.org/10.1016/j.finel.2008.06.001

[10] Marck, G., Nemer, M., Harion, J.L., Russeil, S., and Bougeard, D., 2012, "Topology Optimization Using the SIMP Method for Multiobjective Problems," *Numer. Heat Transfer B*, **61**(6), pp. 439-470. https://doi.org/10.1080/10407790.2012.687979

[11] Bruns, T.E., 2007, "Topology Optimization of Convection-Dominated, Steady-State Heat Transfer Problems," *Int. J. Heat Mass Transfer*, **50**(15-16), pp. 2859-2873. https://doi.org/10.1016/j.ijheatmasstransfer.2007.01.039

[12] Iga, A., Nishiwaki, S., Izui, K., and Yoshimura, M., 2009, "Topology Optimization for Thermal Conductors Considering Design-Dependent Effects, Including Heat Conduction and Convection," *Int. J. Heat Mass Transfer*, **52**(11), pp. 2721-2732. https://doi.org/10.1016/j.ijheatmasstransfer.2008.12.013

[13] Yoon, G.H., 2010, "Topological Design of Heat Dissipating Structure with Forced Convective Heat Transfer," *J. Mech. Sci. Technol.*, **24**(6), pp. 1225-1233. https://doi.org/10.1007/s12206-010-0328-1

[14] Marck, G., Nemer, M., and Harion, J.L., 2013, "Topology Optimization of Heat and Mass Transfer Problems: Laminar Flow," *Numer. Heat Transfer B*, **63**(6), pp. 508-539. https://doi.org/10.1080/10407790.2013.772001

[15] Yan, S.N., Wang, F.W., Hong, J., and Sigmund, O., 2019, "Topology Optimization of Microchannel Heat Sinks Using a Two-Layer Model," *Int. J. Heat Mass Transfer*, **143**, p. 118462. https://doi.org/10.1016/j.ijheatmasstransfer.2019.118462

[16] Zhang, B., Zhu, J., Xiang, G., and Gao, L., 2021, "Design of Nanofluid-Cooled Heat Sink Using Topology Optimization," *Chinese Journal of Aeronautics*, **34**(2), pp. 301-317. https://doi.org/10.1016/j.cja.2020.05.023

[17] Alexandersen, J., Aage, N., Andreasen, C.S., and Sigmund, O., 2014, "Topology Optimisation for Natural Convection Problems," *Int. J. Numer. Methods Fluids*, **76**(10), pp. 699-721. https://doi.org/10.1002/fld.3954

[18] Alexandersen, J., Sigmund, O., and Aage, N., 2016, "Large Scale Three-Dimensional Topology Optimisation of Heat Sinks Cooled by Natural Convection," *Int. J. Heat Mass Transfer*, **100**, pp. 876-891. https://doi.org/10.1016/j.ijheatmasstransfer.2016.05.013

[19] Alexandersen, J., Sigmund, O., Meyer, K.E., and Lazarov, B.S., 2018, "Design of Passive Coolers for Light-Emitting Diode Lamps Using Topology Optimisation," *Int. J. Heat Mass Transfer*, **122**, pp. 138-149. https://doi.org/10.1016/j.ijheatmasstransfer.2018.01.103

[20] Lazarov, B.S., Sigmund, O., Meyer, K.E., and Alexandersen, J., 2018, "Experimental Validation of Additively Manufactured Optimized Shapes for Passive Cooling," *Applied Energy*, **226**, pp. 330-339. https://doi.org/10.1016/j.apenergy.2018.05.106

[21] Audunson, T., and Gebhart, B., 1972, "An Experimental and Analytical Study of Natural Convection with Appreciable Thermal Radiation Effects," *J. Fluid Mechanics*, **52**(1), pp. 57-95. https://doi.org/10.1017/S0022112072002976

[22] Carpenter, J.R., Briggs, D.G., and Sernas, V., 1976, "Combined Radiation and Developing Laminar Free Convection Between Vertical Flat Plates with Asymmetric Heating," *ASME J. Heat Transfer*, **98**(1), pp. 95-100. https://doi.org/10.1115/1.3450476

[23] Hall, D.A., Vliet, G.C., and Bergman, T.L., 1999, "Natural Convection Cooling of Vertical Rectangular Channels in Air Considering Radiation and Wall Conduction," *ASME J. Electron Packag.*, **121**(2), pp. 75-84. https://doi.org/10.1115/1.2792671

[24] Howell, J.R., Daun, K.J., Erturk, H., Gamba, M., and Sarvari, M.H., 2003, "The Use of Inverse Methods for the Design and Control of Radiant Sources," *JSME International Journal Series B – Fluids and Thermal Engineering*, **46**(4), pp. 470-478. https://doi.org/10.1299/jsmeb.46.470

[25] Daun, K.J., Morton, D.P., and Howel, J.R., 2003, "Geometric Optimization of Radiant Enclosures Containing Specular Surfaces," *ASME J. Heat Transfer*, **125**(5), pp. 845-851. https://doi.org/10.1115/1.1599369

[26] Tan, J.Y., Zhao, J.M., and Liu, L.H., 2011, "Geometric Optimization of a Radiation-Conduction Heating Device Using Meshless Method," *Int. J. Thermal Sciences*, **50**(10), pp. 1820-1831. https://doi.org/10.1016/j.ijthermalsci.2011.05.009

[27] Jang, D., Yu, S.H., and Lee, K.S., 2012, "Multidisciplinary Optimization of a Pin-Fin Radial Heat Sink for LED Lighting Applications," *Int. J. Heat Mass Transfer*, **55**(4), pp. 515-521. https://doi.org/10.1016/j.ijheatmasstransfer.2011.11.016

[28] Farahmand, A., Payan, S., and Hosseini Sarvari, S.M., 2012, "Geometric Optimization of Radiative Enclosures Using PSO Algorithm," *Int. J. Thermal Sciences*, **60**, pp. 61-69. https://doi.org/10.1016/j.ijthermalsci.2012.04.024

[29] Kwak, D.B., Kwak, H.P., Noh, J.H., and Yook, S.J., 2018, "Optimization of the Radial Heat Sink with a Concentric Cylinder and Triangular Fins Installed on a Circular Base," *J. Mech. Sci. Technol.*, **32**(1), pp. 505-512. https://doi.org/10.1007/s12206-017-1252-4

[30] Huang, C.H., and Wu, Y.T., 2021, "An Optimum Design for a Natural Convection Pin Fin Array with Orientation Consideration," *Applied Thermal Engineering*, **188**, p. 116633. https://doi.org/10.1016/j.applthermaleng.2021.116633

[31] Czerwiński, G., and Woloszyn, J., 2021, "Optimization of Air Cooling System Using Adjoint Solver Technique," *Energies*, **14**(13), p. 3753. https://doi.org/10.3390/en14133753

[32] Castro, D.A., Kiyono, C.Y., and Silva, E.C.N., 2015, "Design of Radiative Enclosures by Using Topology Optimization," *Int. J. Heat Mass Transfer*, **88**, pp. 880-890. https://doi.org/10.1016/j.ijheatmasstransfer.2015.04.077

[33] Shen, X., Han, H., Li, Y., Yan, C., and Mu, D., 2021, "A Topology Optimization Based Design of Space Radiator for Focal Plane Assemblies," *Energies*, **14**(19), p. 6252. https://doi.org/10.3390/en14196252

[34] Wang, C., Yu, Z., Zhou, M., and Qian, X., 2022, "Topology Optimization of Thermophotonic Problem for Daytime Passive Radiative Cooling," *Int. J. Heat Mass Transfer*, **183**, pp. 122097. https://doi.org/10.1016/j.ijheatmasstransfer.2021.122097

[35] Sevart, C.D., and Bergman, T.L., 2021, "Evolutionary Design Method for a Conducting Solid Cooled by Combined Free Convection and Radiation," *ASME J. Heat Transfer*, **143**(4), p. 042103. https://doi.org/10.1115/1.4049841

[36] Patankar, S.V., 1980, *Numerical Heat Transfer and Fluid Flow*, McGraw-Hill, New York.

[37] Bendsøe, M.P., and Sigmund, O., 1999, "Material Interpolation Schemes in Topology Optimization," *Archive of Applied Mechanics*, **69**, pp. 635-654. https://doi.org/10.1007/s004190050248

[38] Svanberg, K., 1987, "The Method of Moving Asymptotes – a New Method for Structural Optimization," *Int. J. Numerical Methods in Engineering*, **24**(2), pp. 359-373. https://doi.org/10.1002/nme.1620240207

[39] Kandis, M., and Bergman, T.L., 2000, "A Simulation-Based Correlation of the Density and Thermal Conductivity of Objects Produced by Laser Sintering of Polymer Powders," *ASME J. Manuf. Sci. Eng.*, **122**(3), pp. 439-444. https://doi.org/10.1115/1.1286558

[40] Yang, P., Deibler, L.A., Bradley, D.R., Stefan, D.K., and Carrol, J.D., 2018, "Microstructure Evolution and Thermal Properties of an Additively Manufactured, Solution Treatable AlSi10Mg Part," *Journal of Materials Research*, **33**, pp. 4040-4052. https://doi.org/10.1557/jmr.2018.405

[41] Wen, C.D., and Mudawar, I., 2004, "Emissivity Characteristics of Roughened Aluminum Alloy Surfaces and Assessment of Multispectral Radiation Thermometry (MRT) Emissivity Models," *Int. J. Heat Mass Transfer*, **46**(17-18), pp. 3591-3605. https://doi.org/10.1016/j.ijheatmasstransfer.2004.04.025

[42] Wen, C.D., and Mudawar, I., 2006, "Modeling the Effects of Surface Roughness on the Emissivity of Aluminum," *Int. J. Heat Mass Transfer*, **49**(23-24), pp. 4279-4289. https://doi.org/10.1016/j.ijheatmasstransfer.2006.04.037

[43] Bergman, T.L., and Lavine, A.S., 2017, *Fundamentals of Heat and Mass Transfer*, 8th edition, John Wiley and Sons, New Jersey.

[44] Hottel, H. C., 1954, "Radiant Heat Transmission" *Heat Transmission*, W.H. McAdams, ed., McGraw-Hill, New York.

Figure Captions

Fig. 1 Physical domain and boundary conditions

Fig. 2 Topology optimization process for adjusting the continuous solid distribution, $\gamma(x, y)$. I_{cm} = 0 at the start of the first iteration.

Fig. 3 The dual solid method (DSM) process. Dashed box represents the topology optimization process of Fig. 2. I_{DSM} = 0 for the $S_{\mathrm{rad},cm}(x, y) = 0$ case.

Fig. 4 Pure conduction base case evolution history of the conduction resistance and solid shapes associated with the continuous solid model using the TO process of Fig. 2. Solid distributions are shown at I_{cm} = 5, 20, 400, and 1350.

Fig. 5 The base case solid distribution (left) and temperature distribution (right) associated with (a) the optimized continuous solid of the pure conduction solution (I_{cm} = 1350 of Fig. 4), and (b) the equivalent discrete solid with radiation and conduction included (I_{DSM} = 0).

Fig. 6 Evolution history of the overall thermal resistance associated with the continuous solid and the radiation conditions of the base case using the TO process of Fig. 2. Solid distributions are shown for I_{cm} = 5, 20, 400, and 1911.

Fig. 7 The base case discrete solid and temperature distributions (I_{DSM} = 1)

Fig. 8 Base case evolution history of the total pure conduction thermal resistances associated with the discrete solid for the first 100 iterations of the DSM. The minimum total thermal resistance occurs at I_{DSM} = 54.

Fig. 9 Base case discrete solid and temperature distributions associated with $R'_{\mathrm{tot,min}}$ the of Fig. 8 at I_{DSM} = 54

Fig. 10 Evolution history of the total and pure conduction thermal resistances associated with the discrete solid for (a) T_o = 1000 K and (b) T_o = 500 K

Fig. 11 Discrete solid shapes and temperature distributions associated with $R'_{\text{tot,min}}$ for (a) $T_o = 500$ K (I_{DSM} = 0), (b) $T_o = 750$ K (I_{DSM} = 54), and (c) $T_o = 1000$ K (I_{DSM} = 31).

Fig. 12 Evolution history of the total and pure conduction thermal resistances associated with the discrete solid for (a) k_s^* = 0.01 and (b) k_s^* = 0.1 with T_o = 750 K

Fig. 13 Discrete solid shapes and temperature distributions associated with T_o = 750 K and k_s^* = 0.01 (top), k_s^* = 0.1 (middle), and k_s^* = 1 (bottom). I_{DSM} = 0 for the first and second columns. The third and fourth columns are associated with $R'_{\text{tot,min}}$ and (a) I_{DSM} = 9, (b) I_{DSM} = 16, and (c) I_{DSM} = 54.

Fig. 14 Discrete solid shapes and temperature distributions associated with grid sizes of *CC* = 0.01 (top), *CC* = 0.001 (middle), and *CC* = 0.0005 (bottom). I_{DSM} = 0 for the first and second columns. Third and fourth columns are associated with $R'_{\text{tot,min}}$ and (a) I_{DSM} = 8, (b) I_{DSM} = 15, and (c) I_{DSM} = 7.

Fig. 15 Discrete solid shapes and temperature distributions associated with grid sizes of 120 × 120 (top), 180 × 180 (middle), and 240 × 240 (bottom). I_{DSM} = 0 for the first and second columns. Third and fourth columns are associated with $R'_{\text{tot,min}}$ and (a) I_{DSM} = 7, (b) I_{DSM} = 15, and (c) I_{DSM} = 11.

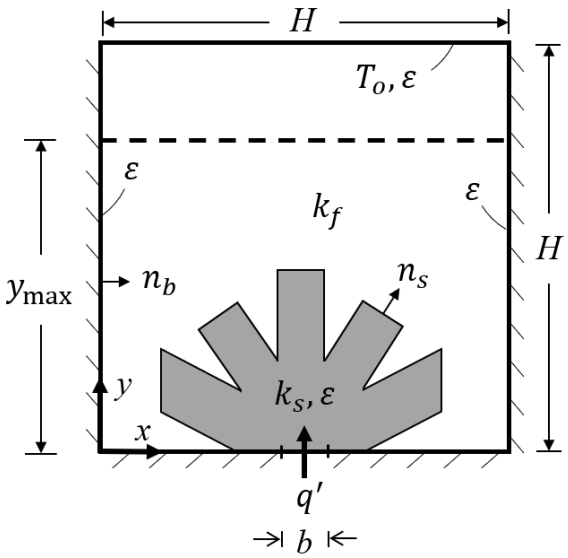

Fig. 1 Physical domain and boundary conditions

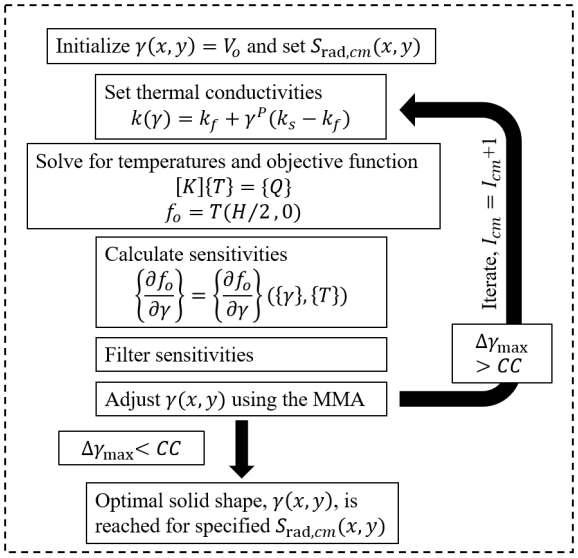

Fig. 2 Topology optimization process for adjusting the continuous solid distribution, $\gamma(x,y)$. I_{cm} = 0 at the start of the first iteration.

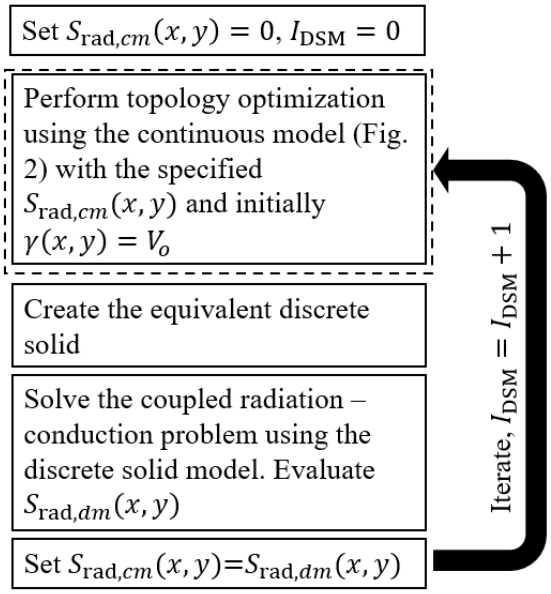

Fig. 3 The dual solid method (DSM) process. Dashed box represents the topology optimization process of Fig. 2. I_{DSM} = 0 for the $S_{\mathrm{rad},cm}(x,y) = 0$ case.

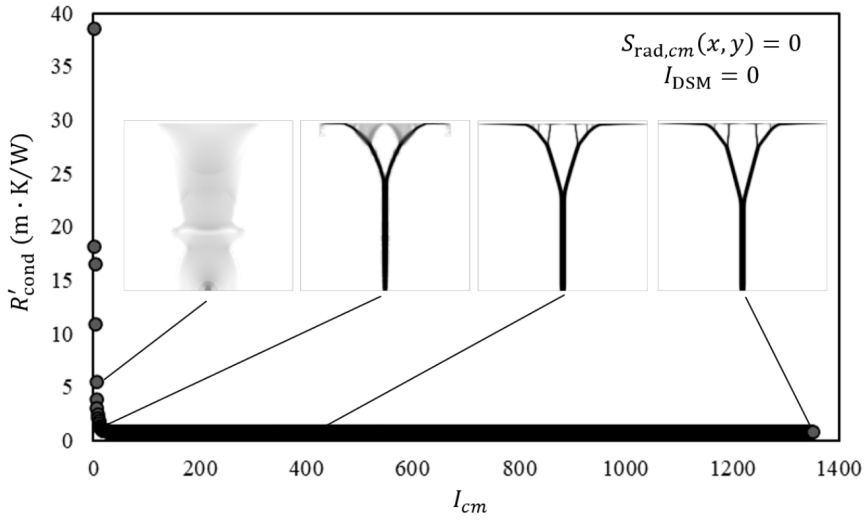

Fig. 4 Pure conduction base case evolution history of the conduction resistance and solid shapes associated with the continuous solid model using the TO process of Fig. 2. Solid distributions are shown at I_{cm} = 5, 20, 400, and 1350.

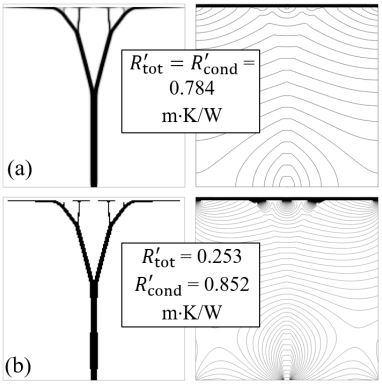

Fig. 5 The base case solid distribution (left) and temperature distribution (right) associated with (a) the optimized continuous solid of the pure conduction solution (I_{cm} = 1350 of Fig. 4), and (b) the equivalent discrete solid with radiation and conduction included (I_{DSM} = 0).

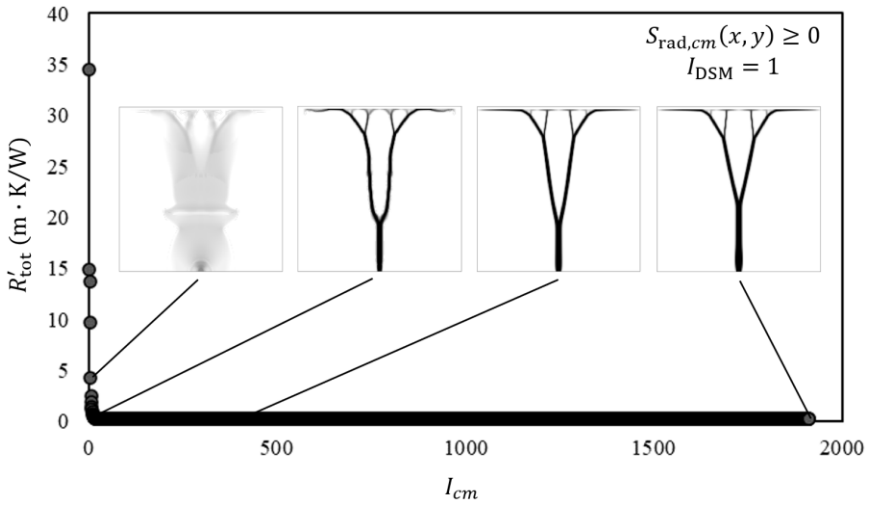

Fig. 6 Evolution history of the overall thermal resistance associated with the continuous solid and the radiation conditions of the base case using the TO process of Fig. 2. Solid distributions are shown for I_{cm} = 5, 20, 400, and 1911.

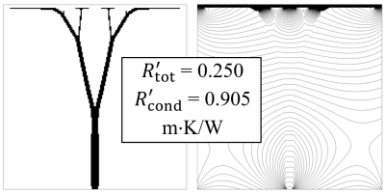

Fig. 7 The base case discrete solid and temperature distributions (I_{DSM} = 1)

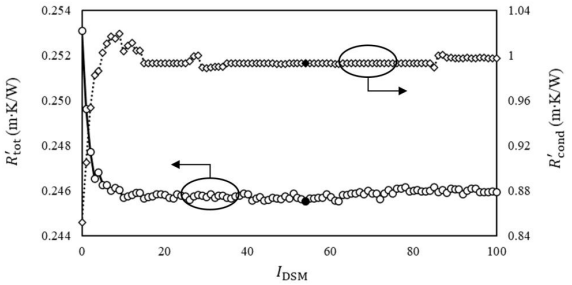

Fig. 8 Base case evolution history of the total pure conduction thermal resistances associated with the discrete solid for the first 100 iterations of the DSM. The minimum total thermal resistance occurs at $I_{\mathrm{DSM}} = 54$.

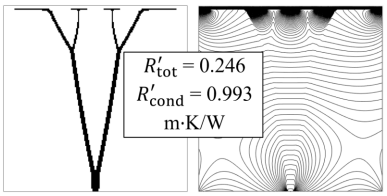

Fig. 9 Base case discrete solid and temperature distributions associated with $R'_{\mathrm{tot,min}}$ the of Fig. 8 at I_{DSM} = 54

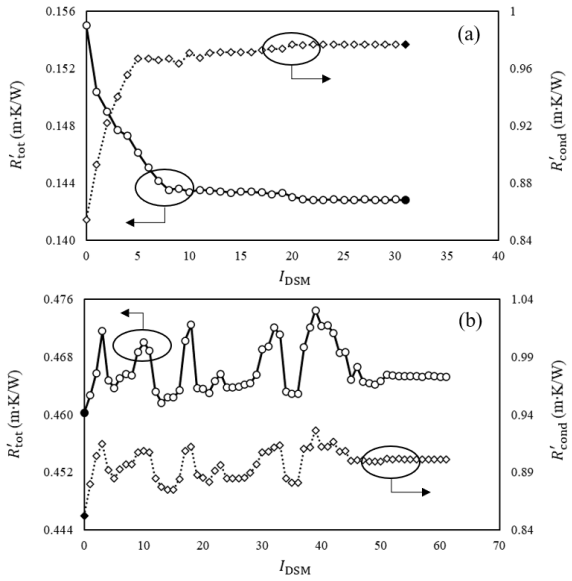

Fig. 10 Evolution history of the total and pure conduction thermal resistances associated with the discrete solid for (a) T_o = 1000 K and (b) T_o = 500 K

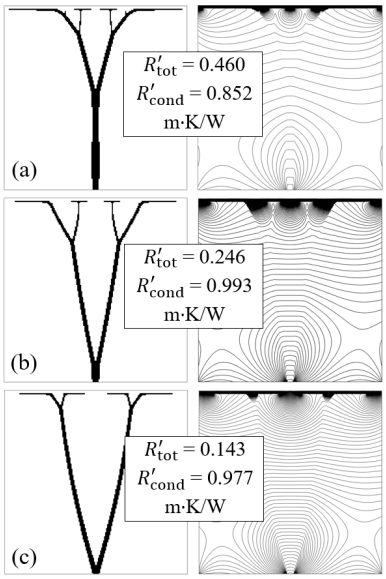

Fig. 11 Discrete solid shapes and temperature distributions associated with $R'_{\mathrm{tot,min}}$ for (a) $T_o = 500$ K (I_{DSM} = 0), (b) $T_o = 750$ K (I_{DSM} = 54), and (c) $T_o = 1000$ K (I_{DSM} = 31)

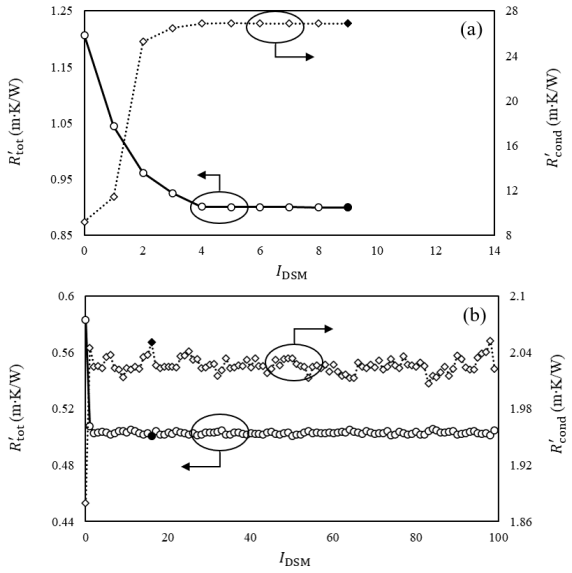

Fig. 12 Evolution history of the total and pure conduction thermal resistances associated with the discrete solid for (a) k_s^* = 0.01 and (b) k_s^* = 0.1 with T_o = 750 K

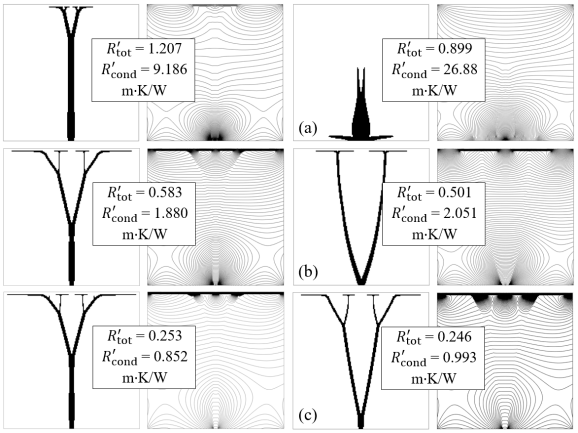

Fig. 13 Discrete solid shapes and temperature distributions associated with T_o = 750 K and k_s^* = 0.01 (top), k_s^* = 0.1 (middle), and k_s^* = 1 (bottom). I_{DSM} = 0 for the first and second columns. The third and fourth columns are associated with $R'_{\mathrm{tot,min}}$ and (a) I_{DSM} = 9, (b) I_{DSM} = 16, and (c) I_{DSM} = 54.

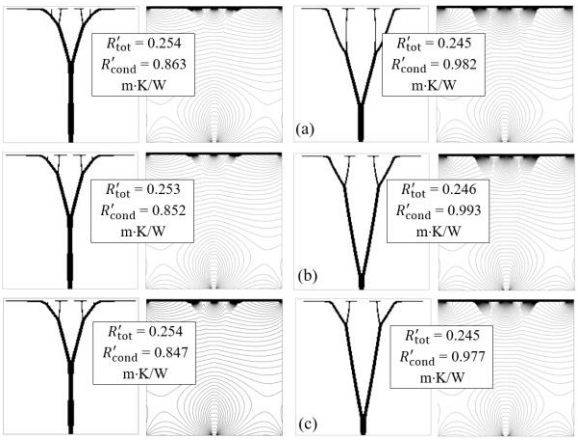

Fig. 14 Discrete solid shapes and temperature distributions associated with grid sizes of *CC* = 0.01 (top), *CC* = 0.001 (middle), and *CC* = 0.0005 (bottom). I_{DSM} = 0 for the first and second columns. Third and fourth columns are associated with $R'_{\mathrm{tot,min}}$ and (a) I_{DSM} = 8, (b) I_{DSM} = 15, and (c) I_{DSM} = 7.

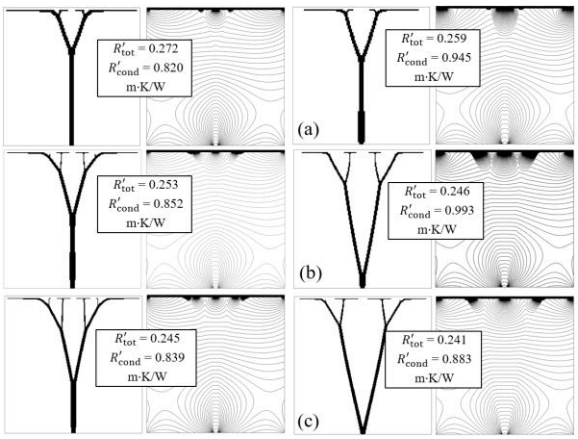

Fig. 15 Discrete solid shapes and temperature distributions associated with grid sizes of 120 × 120 (top), 180 × 180 (middle), and 240 × 240 (bottom). I_{DSM} = 0 for the first and second columns. Third and fourth columns are associated with $R'_{\mathrm{tot,min}}$ and (a) I_{DSM} = 7, (b) I_{DSM} = 15, and (c) I_{DSM} = 11.